Determining the physical and metallurgical properties of lump ore subgroups on the Kapstevel South iron ore deposit, Kolomela Mine

Tricia Robyn Scott

Supervisor: Professor Emeritus Richard Minnitt

A research report submitted to the Faculty of Engineering and the Built Environment, University of the Witwatersrand, in partial fulfilment of the requirements for the degree of Master of Science in Engineering.

Johannesburg 2020

Declaration

I declare that this research report is my own unaided work. It is being submitted to the Degree of Master of Science to the University of the Witwatersrand, Johannesburg. It has not been submitted before for any degree or examination to any other University.

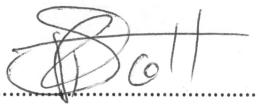

.....

7th day of December year 2020

Abstract

Geometallurgy involves understanding the spatial variability of a deposit's metallurgical properties to promote optimal resource utilisation. This geometallurgical study investigates the physical and metallurgical iron ore properties that affect blast furnace operation and that are used to market lump iron ore. Different ore types are commonly blended to meet specific blast furnace requirements; thus, knowledge of these properties is crucial. Physical and metallurgical test results were compared with the geological features recorded for core samples. Results were then grouped based on the geological features that affect these properties, including ore texture, competency and chert content. The subgroups enable physical and metallurgical properties to be assigned to all ore exhibiting similar geological features. This provides an understanding of the spatial variation of these ore properties and can subsequently assist in creating the mine's first geometallurgical block model. Planning the mining sequence with full spatial knowledge of the chemical, physical and metallurgical characteristics across the deposit will enable optimal resource utilisation. Additionally, the block model would allow prediction of the physical and metallurgical properties of product beds and promote optimal marketing.

Acknowledgements

I would like to express my appreciation to Kumba Iron Ore Ltd for allowing the use of the company's geometallurgical data and for financial assistance during this study. Thank you to the Principal Mining Geologist, Marushnee Govender, for her guidance during this project, and to Professor Richard Minnitt for his encouragement and supervision. Logging all core samples would have been a mammoth task on my own – thanks to the geologists who helped with the meticulous logging of geometallurgical core: Louis le Grange, Joshua van Schalkwyk, Anton Viljoen, Peter Cloete, Dishebo Letanta and Lorena Tafur.

Contents

List of Figures

List of Tables

List of Abbreviations

AI: abrasion index

BIF: banded ironstone formation

BKN: broken

BMOZ: black mineralised ore zone

CID: channel iron deposit

CoV: coefficient of variation

CPT: competent

CRM: certified reference material

CWi: crusher work index

DI: decrepitation index

DMS: dense media separation

DMT: diamictite

DSO: direct shipping ore

EAF: electric arc furnace

GAB: gabbro

GOE: great oxidation event

GPS: global positioning system

GRG: gravity recoverable gold

GSI: geological strength index

HEM: hematite

ID: identification

ISO: International Organisation for Standardisation

KIO: Kumba Iron Ore Limited

KSS: Kapstevel South

LAV: lava

LOI: loss on ignition

MAE: mean absolute error

ME: mean error

MEAB: meso- to macrobanded

MEB: mesobanded

MIB: microbanded

MLR: multiple linear regression

NPV: net present value

PCA: principal component analysis

PP: projection pursuit

PPR: projection pursuit regression

QA/QC: quality assurance/quality control

SMC: sag mill comminution

RC: reverse circulation

RD: relative density

RDI: reduction-disintegration index

RI: reducibility index

RMSE: root mean squared error

ROM: run-of-mine

Std. dev: standard deviation

TDI: totally disintegrated

TI: tumble index

UCS: uniaxial compressive strength

UHDMS: ultra-high dense media separator

1 Introduction

A rapid increase in iron ore production, exceeding the rate at which steel was produced (Figure 1.1) has resulted in an iron ore surplus within the global market. The divergence between the world iron ore and world steel production trends can be seen from the year 2004, increasing to what is seen today. An increase in iron ore price initially followed the spike in iron ore demand and plummeted as surplus iron ore entered the market. This has resulted in increased pressure for mining companies to lower costs and remain competitive. Where iron ore furnaces historically accepted the iron ore that was available, these are now able to be more selective of their suppliers, preferring those that provide the most suitable and consistent ore for the furnaces. It is thus vital for mining companies to provide customers with ore exhibiting consistent and predictable metallurgical properties (Fernández-González *et al*, 2016; Mitterlehner *et al*., 2004). This practice would result in smooth, interruption-free furnace operation, satisfied customers, and a sound, reliable reputation for the mining company.

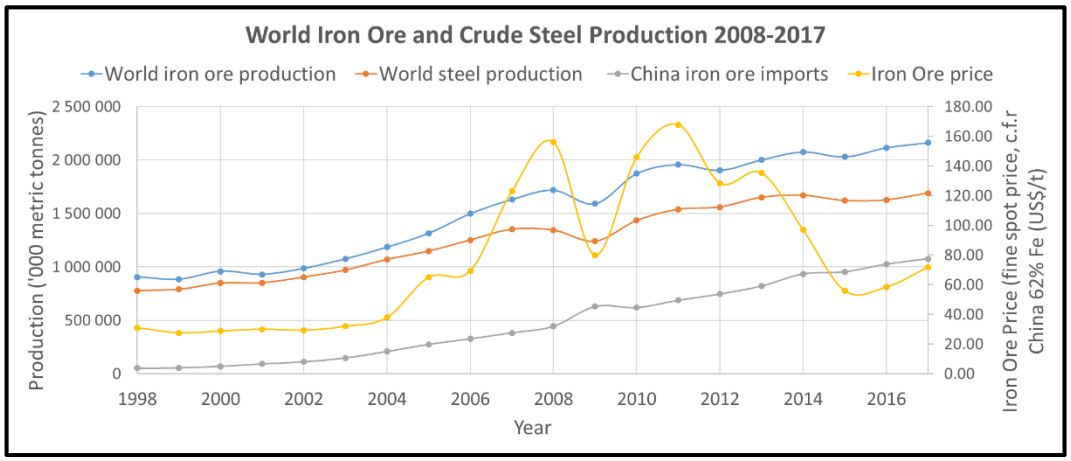

Figure 1.1 World Iron Ore and Crude Steel Production from 2008 to 2017. Data derived from Index Mundi (2019) and World Steel Association (2018)

Additionally, the drive to reduce carbon-dioxide (CO_2) emissions and move towards more environmentally sustainable practices encourages the use of lump and pellet iron ore feed. In 2017, the iron and steel sector accounted for 23.5% of industry's direct CO_2 emissions (International Energy Agency, 2019), making it one of the biggest contributors to air pollution worldwide. Ore that optimises blast furnace energy consumption, such as lump and pellet, fetches premium prices over lower-quality, finer feed and is more environmentally conscious

Kolomela Mine is primarily a direct shipping ore (DSO) iron ore operation southwest of Postmasburg, Northern Cape, and forms one of two Kumba Iron Ore Limited (KIO) operational mines. A geometallurgical program was implemented in 2017 to better characterise and understand the various metallurgical and physical properties of the ore body, which would aid the company in ensuring clients receive optimum-quality iron ore.

The main physical and metallurgical variables affecting blast furnace operation include the tumble index (TI), abrasion index (AI), disintegration index (DI), reduction-disintegration index (RDI) and reducibility index (RI). These variables are routinely tested on DSO samples derived from geometallurgical drilling at Kolomela Mine and are believed to be related to primary geological variables such as ore texture, grade and mineralogical content.

Data on the above-mentioned primary variables are routinely collected during the geological logging and the assaying of samples. Understanding the relationship between the primary and physical/metallurgical variables will enable proxies to be developed, reducing the need for costly and time-consuming geometallurgical testing in the future. An additional benefit is that it will also allow the vast amount of current spatially distributed geological data (exploration core drilling as well as closely spaced reverse-circulation (RC) drilling) to be correlated with specific physical and metallurgical properties.

Developing proxies between the primary and response variables will aid in the creation of the geometallurgical model. Metallurgical and physical response variables are typically influenced by a number of factors, such as geology and mining, making them non-additive (Coward, Vann, Dunham and Stewart, 2009). Additive variables, on the other hand, can be modelled and subsequently used to estimate the response variables, such as performed by Ashley and Callow (2000); Mwanga, Rosenkranz and Lamberg, (2015) and Shi, Kojovic, Larbi-Bram, and Manlapig, 2009; Vos, Stange and Bradshaw, (2014). As a result, the mine would be able to predict the metallurgical and physical properties of product beds based on the textures, grades and mineralogy of the ore used to create that blend.

The objective of this study is thus to identify proxies between the physical/metallurgical properties (TI, AI, DI, RI and RDI) and primary variables such as ore texture, grade and

mineralogical content. Identifying these proxies would enable the mine to predict the physical and metallurgical properties of product beds and ensure blast furnace customers receive ore that meets their quality needs.

2 Iron Ore and Blast Furnace Operation

2.1 Iron Ore

Iron, the second-most common metal in the earth, became popular around 800 B.C.E at the beginning of the iron-age (Jensen and Bateman, 1981). Today, it is the most widely used metal due to its favourable mechanical properties and relatively cheap production (Muwanguzi, Karasev, Byaruhanga and Jönsson, 2012). It is most used as steel and is found everywhere from houses, machinery, cities to various forms of transport.

Three types of iron oxides are found naturally: hematite (Fe_2O_3), magnetite (Fe_3O_4) and goethite (FeOOH) (Clout and Manuel, 2015; Cornell and Schwertmann, 2003). The term "martite" is used to indicate the hematite pseudomorph of primary magnetite (Morris, 1985). Hydrohematite ($Fe_{(2-x)/3}(OH)_xO_{3-x}$) occurs where hydroxide (OH^-) ions replace oxygen atoms in hematite (Wolska and Szajda, 1985).

Wustite (FeO) is naturally unstable, as it absorbs oxygen from the air to form hematite (Johnson, 1918). All three of the naturally occurring iron oxides can be processed and used commercially.

2.2 Commercial Iron

Commercial iron can be grouped into three classes: wrought iron, steel and cast iron. Wrought iron generally contains the least foreign elements (for example carbon, silicon, manganese, phosphorus and sulphur) which may only comprise up to half a percent of the material in total (Forsythe, Meissner and Mohr, 1922). Wrought iron is unique in that it is softer than cast iron and steel, is fibrous, malleable, ductile, and has a higher melting point. Before wrought iron melts, it exhibits plastic behaviour that allows two pieces to be welded firmly together (Forsythe *et al.,* 1922). As more contaminants are added to wrought iron, these properties change. The melting point decreases, hardness increases, it obtains a crystalline structure, and its malleable properties are hindered (Forsythe *et al.,* 1922).

Steel is like wrought iron, except that it may contain higher concentrations of carbon. Its properties vary depending on the amount of carbon it contains, which ranges from a few hundredths of a percent to above 2% (Forsythe *et al.,* 1922). Low-carbon steel behaves

much like wrought iron, but as carbon content increases, the melting point decreases, steel becomes harder, and it loses its welding properties (Forsythe *et al.,* 1922). Steel also gains the characteristic of becoming extremely hard when quenched. The result is a hard and brittle material, contrasting the tough and fibrous wrought iron (Forsythe *et al.,* 1922).

Contaminants comprise 5 to 10% of cast iron. In general, silicon constitutes less than 3%, carbon constitutes 3.25 to 4.5%, manganese less than 2%, phosphorus less than 1% and sulphur less than 0.1% (Forsythe *et al.,* 1922). Steel and cast iron thus both exist at a wide composition range, with properties varying as contaminants are added or removed.

Cast iron, in contrast to the contaminant-poor wrought iron, melts relatively easily and rapidly changes to the fluid state, which prevents its welding ability (Forsythe *et al.,* 1922). It is also coarsely crystalline, brittle and physically appears different to wrought iron and steel. Cast iron is favourable as it can be formed into various shapes at a low cost. Its wide range of physical properties can also be changed by monitoring chemical content and cooling rate, without major changes to production methods (Elliott, 1988).

The specific physical properties of cast iron vary according to the way carbon precipitates in the matrix. The carbon precipitate can form either cementite (iron carbide) or graphite and is dependent on several factors including cooling rate and the specific nature or treatment of the liquid iron (Elliott, 1988). The carbon precipitate will affect the machinability, thermal conductivity, damping, hardness and resistance to wear of the cast iron (Elliott, 1988). Pig iron is the rawer form of cast iron, and is the only product directly produced from iron ore (Forsythe *et al.,* 1922). This material is then further processed and refined to produce wrought iron and steel.

2.3 From the Mine to the Blast Furnace

Iron ore is first calcined before being used in the blast furnace, where it is packed into firebrick-lined stoves (Simons and Gregory, 1940). The heat-resistant bricks are made from fireclay, which is a mixture of silica and alumina in various proportions. The ore is heated to a yellow heat, after which it undergoes a change in texture, becoming less dense and more porous (Simons and Gregory, 1940). Sulphur existing as iron sulphide is burnt and released as sulphur dioxide gas, lowering the sulphur content of the iron ore. Additionally, the increased porosity of the ore is necessary to allow for better penetration

of carbon monoxide (CO) gas, which is used as a reducing agent to produce metallic iron (Simons and Gregory, 1940). In this way, reduction progresses at a faster pace.

2.4 Blast Furnace Operation

The objective of smelting ore in the blast furnace is to reduce it to metallic iron (Fe). The furnace (Figure 2.1) consists of a cylindrical structure lined with refractory firebricks, and can be as high as 30 metres. Iron ore and limestone (the burden), and coke are fed into the top of the blast furnace in alternating layers (Geerdes, Chaigneau, Kurunov, Lingiardi and Ricketts, 2015). Coke is more permeable than the burden, and aids gas flow in the furnace. Hot air is blasted through tuyères near the bottom of the furnace. The tuyères consist of 12 to 42 (depending on the size of the furnace) conical copper nozzles which transport heated air (1000°C-1300°C) into the blast furnace (Geerdes *et al.,* 2015). The heated air gasifies the coke, or alternative fuel, that has been injected in front of the tuyères, and creates an intense flame exhibiting temperatures of 1900°C-2300°C (Geerdes *et al.,* 2015).

The fast-moving gas flowing out of the tuyères creates an area called the raceway (indicated in Figure 2.2). This flame generated from the tuyères creates the heat needed to melt the burden (Geerdes *et al.,* 2015).

The zones of a blast furnace are shown in Figure 2.2, consisting of the hearth, bosh, belly, stack and throat. Burden and coke enter through the top of the furnace and is found in the throat, after which the ore is heated, and reduction reactions start in the stack. By the time the ore reaches the bosh, it is completely melted, and reduction is complete. The liquid metal and slag are then collected in the hearth via tapholes (Geerdes *et al.,* 2015).

The hot gases facilitate the conversion of the limestone flux to lime (CaO), which melts at a lower temperature (around 870°C) than the surrounding charge and forms the fusible slag (American Iron and Steel Institute, 2005). Iron ore, in contrast, starts melting at 1000-1300°C (Geerdes *et al.,* 2015). Lime aids in the removal of contaminants from the iron ore, combining with these elements to form slag (American Iron and Steel Institute, 2005). The slag, exhibiting a density of around 2.3 t/m^3, descends towards the bottom of the furnace, but floats on the surface of the liquid metallic iron, which exhibits densities around 7.2 t/m^3 (Geerdes *et al.,* 2015).

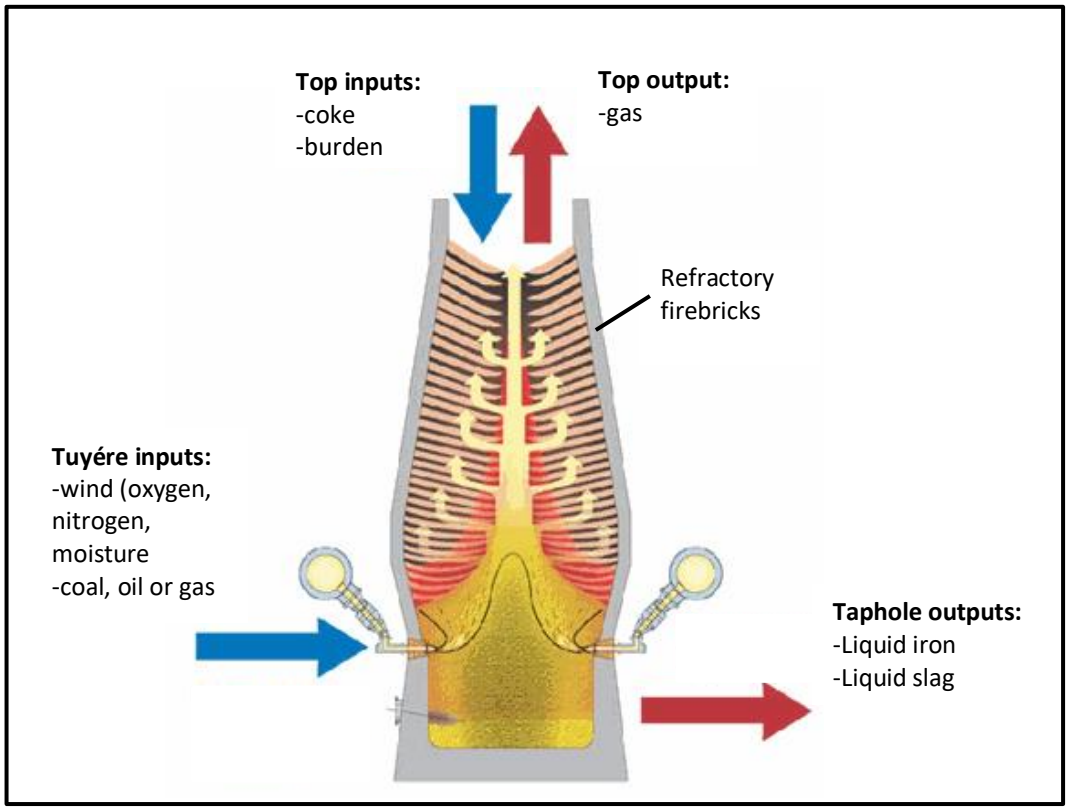

Figure 2.1 Cross-section diagram of a blast furnace, after Geerdes *et al.* (2015)

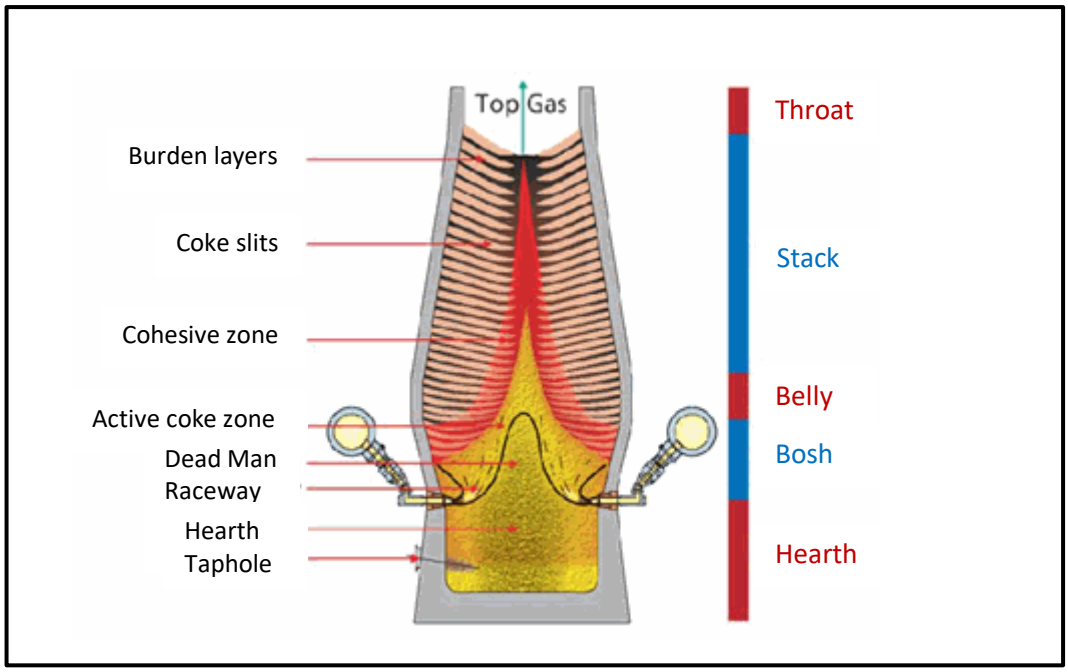

Figure 2.2 Illustration of the different zones in a blast furnace, after Geerdes *et al.* (2015)

The liquid iron is removed through a metal tap-hole at the bottom of the furnace, at a level below the slag-hole (Geerdes *et al.,* 2015). This taphole is 4-6 cm in diameter and 2.5-3.5 m in length (Geerdes *et al.,* 2015). Thereafter, the iron flows along a main sand

channel (sow) that branches off into smaller lateral channels (pigs), thus the term “pig iron” (Simons and Gregory, 1940). The hot, solid metal is then broken up and transferred to be used as required. Alternatively, the molten iron is run into ladles which transfer the pig iron into iron moulds that are quickly chilled in cool water (Simons and Gregory, 1940). Slag can then be converted to granulated slag by dousing with water, after which it may be used during cement manufacture (Geerdes *et al.,* 2015).

Up to this point, iron ore has been converted to pig iron which contains roughly 93.5-95% iron, 0.3-0.9% silicon, 0.025-0.05% sulphur, 0.55-0.75% manganese, 0.03-0.09% phosphorus, 0.02-0.06% titanium, and 4.1-4.4% carbon (American Iron and Steel Institute, 2005). It will need to go through further processes to reach an impurity level of approximately 0.2-0.3% before it can be used for commercial purposes.

2.5 Reduction Reactions in the Blast Furnace

Several raw materials are added to the blast furnace, after which a series of steps produces the liquid iron metal. These raw materials include:

- Iron ore (Fe_2O_3 or Fe_3O_4), silica (SiO_2) and alumina (Al_2O_3)
- Limestone, which converts to lime (CaO)
- Carbon dioxide (CO_2)
- Coke (essentially carbon and some ash)
- Air (mostly N_2 and O_2)

The oxygen combines with carbon, from coke, to create carbon monoxide (CO), carbon dioxide (CO_2) and heat. This reacts with iron ore to create metallic iron and carbon dioxide (American Iron and Steel Institute, 2005; Johnson, 1918):

Initially hematite (Fe_2O_3) is reduced to magnetite (Fe_3O_4) – an exothermic reaction which adds further heat to the furnace (Geerdes *et al.,* 2015; Simons and Gregory, 1940). This reaction also weakens the crystal structure and may cause it to break down into smaller particles (Geerdes *et al.,* 2015).

$3Fe_2O_3 + CO \rightarrow 2Fe_3O_4 + CO_2$ and

$3Fe_2O_3 + C \rightarrow 2Fe_3O_4 + CO$

Magnetite is then converted to wüstite (FeO) via an endothermic reaction (Geerdes *et al.,* 2015; Simons and Gregory, 1940).

$Fe_3O_4 + CO \rightarrow 3FeO + CO_2$ and

$Fe_3O_4 + C \rightarrow 3FeO + CO$

With increasing temperature, wüstite reduces to iron metal, which drips into the hearth of the furnace (Geerdes *et al.,* 2015; Simons and Gregory, 1940).

$FeO + CO \rightarrow Fe + CO_2$

$FeO + C \rightarrow Fe + CO$

In this way, the oxygen content of the gas in the blast furnace constantly increases, while that in the ore decreases. The various reduction reactions, at different stages in the blast furnace, are shown in Figure 2.3 (Geerdes *et al.,* 2015).

Silicon, sulphur and titanium from the original iron ore combine with lime to form slag. Most potassium and sodium are concentrated in the slag, but some are released as vapour with the gas. Manganese, and nearly all phosphorus, passes through to the hot metal (Geerdes *et al.,* 2015).

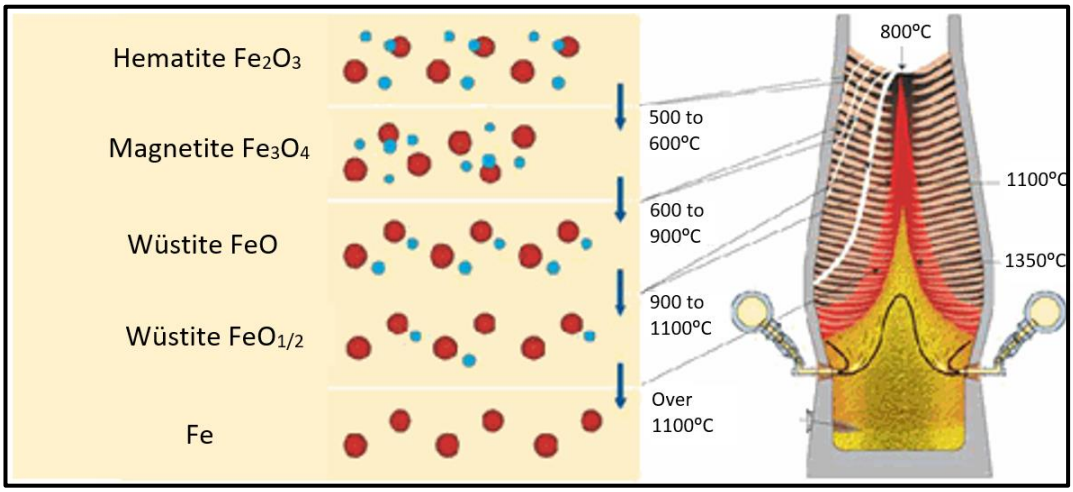

Figure 2.3 The iron ore reduction reactions occurring at different stages in the blast furnace (Geerdes *et al.,* 2015)

The gases produced during the process (for example CO_2, N_2, CO) move to the top of the furnace and through gas cleaning equipment. It then passes through a down take where

they are used to pre-heat the ore calciners and air blasts (American Iron and Steel Institute, 2005).

2.6 Other Types of Furnaces

Pig iron produced from blast furnaces is supplied to basic oxygen furnaces, which produced 71.5% of the worldwide steel in 2017 (World Steel Association 2018). Electric arc furnaces (EAFs) came in second with regards to worldwide steel production, supplying 28% of the global steel.

The EAF produces heat-generating electric arcs between two or more electrodes. The arc-generated heat is then used to smelt the iron ore, either directly by striking the ore, or indirectly by radiation (Simons and Gregory, 1940).

Electric arc furnaces offer several advantages, including the high temperatures that can be obtained, leading to the improved removal of impurities, the efficient separation of air and gases from the molten iron, and the consistent carbon content of the molten fluid (Simons and Gregory, 1940). Although offering these advantages to the conventional blast furnace, the high operating cost of producing electricity is often a deterrent. To offset the high electricity costs, EAFs are commonly used to smelt low-cost raw materials such as scrap steel (Geerdes *et al.,* 2015). As EAFs are not typically used to smelt iron ore, they will be excluded from the study.

2.7 Variations in the Form of Iron Ore Feed

Iron ore is added to the blast furnace in the form of lump, sinter or pellets (American Iron and Steel Institute, 2005; Geerdes *et al.,* 2015; Simons and Gregory, 1940). Examples of these materials are shown in Figure 2.4. Lump ore is approximately 6-25mm in size but may vary slightly depending on market requirements. Lump comprises raw ore containing 58-70 %Fe (Geerdes *et al.,* 2015) and any lower-grade ore needs to be beneficiated to increase its iron content before entering the blast furnace (American Iron and Steel Institute, 2005). Lump is produced by mining the ore and then subjecting it to crushing and screening processes. The generation of lump ore is highly dependent on the geological properties of the ore deposit, and is generally becoming scarcer worldwide (Geerdes *et al.,* 2015).

Figure 2.4 Forms of iron ore used in the blast furnace (Geerdes *et al.,* 2015)

Lump ore does not reduce as easily as fine (150µm to 6mm in size), but is preferred due to the larger air gaps found between particles during packing (Johnson, 1918). These air gaps facilitate the flow of blast furnace gases better than the fine ore. “Soft” ore can generally be excavated by shovel or hand, without the need for blasting (Clout and Manuel, 2015). Soft lump ore is easily reducible and their plastic nature upon melting prevents them from being blown out of the top of the blast furnace (Johnson, 1918). This soft ore also exposes less surface area on which gases can react, when compared to fine ore. As a result, physical and chemical changes occur at a slower rate, aiding smooth blast furnace operation (Johnson, 1918). Generally, blast furnaces prefer lump ore that is not too dense and can be easily penetrated by gases (Forsythe *et al.,* 1922).

Pellets are made from the lower-grade iron ore that is crushed to a powder (less than 150 µm), after which contaminants are removed and rolled into marble-sized balls containing 60-65 %Fe (American Iron and Steel Institute, 2005; Geerdes *et al.,* 2015). To produce sinter, fine iron ore is mixed with coke, limestone and iron-bearing steel plant waste materials. This material is placed on a sintering strand where it is heated and particles fuse together to form larger-sized pieces of iron (American Iron and Steel Institute, 2005). The sinter is then passed through a screen size of 12-35 mm, to achieve an end-product that is more suitable to withstand blast furnace conditions than the original fine ore (Cores, Babich, Muñiz, Ferreira and Mochon, 2010).

The forms of iron ore that can be used in a blast furnace include magnetite, hematite and goethite. Magnetite ore is denser than hematite and reduces at higher temperatures, resulting in a lower production rate and higher fuel costs (Johnson, 1918).

Goethite is highly reducible in blast furnaces. This is believed to be due to the expulsion of water at temperatures of 400-500°C, creating porous gaps within the ore, and leading to a greater surface area on which reduction can occur (Johnson, 1918). However, a high-

water content, and corresponding loss on ignition, occupies volume in the iron ore which is sold per tonne. The blast furnace would thus produce less liquid metal per tonne of processed iron ore, as a large portion is lost as water.

Iron silicates such as ferrosilite ($FeSiO_3$), and iron carbonates such as siderite ($FeCO_3$), contain 42.4% and 48.3 %Fe respectively. This makes these ores less favourable than the above-mentioned iron oxides which may contain up to 72.4 %Fe and thus yield more metal per tonne of ore (Forsythe *et al.,* 1922). Additionally, iron oxides produce metallic iron by the straight-forward removal of oxygen, where iron silicates and carbonates require further processes to remove carbon and silicon (Forsythe *et al.,* 1922).

Minerals such as pyrite (FeS_2) and siderite are generally avoided for iron extraction due to the adverse environmental effects of SO_x and CO_2 emissions (Clout and Manuel, 2015).

3 Iron Ore Feed Quality

The quality of iron ore determines how efficiently the blast furnace operates, the costs associated therewith as well as the environmental effects of producing iron metal. It is thus vital to characterise and quantify the properties affecting blast furnace operation, enabling operators to plan the optimal iron ore blend for each furnace. The three dominant features determining the quality of iron ore are physical, metallurgical and chemical properties (Clout, 1998; Geerdes *et al.*, 2015; Muwanguzi *et al*., 2012).

3.1 Physical, Metallurgical and Chemical Properties of Iron Ore

Many physical and metallurgical properties of iron ore ultimately affect the gas flow in a furnace. Gas flow in the blast furnace is important as the more oxygen is removed from the ore, the more productive the furnace. According to Geerdes *et al.* (2015), a significant portion of blast furnace problems are caused by ore layers exhibiting poor permeability. This low permeability is largely caused by fines in the ore layers, which are either directly charged into the furnace, or created during the break-down of ore (Geerdes *et al.,* 2015). The impermeable layers are difficult to melt and can result in chilling of the blast furnace as well as tuyére failures (Geerdes *et al*., 2015).

The way in which iron ore behaves during handling, transport and descent in the blast furnace are a result of its physical properties, while metallurgical properties indicate how the ore reacts during reduction in the blast furnace (Muwanguzi *et al.,* 2012). The physical and metallurgical factors of ore can be measured using several indices, including the TI, AI, DI, RDI and RI. TI and AI indicate the way ore will react upon transport and handling, while DI, RDI and RI measure performance in various zones of the blast furnace, as indicated in Figure 3.1. As temperature increases down the blast furnace; the DI predicts ore behaviour in the thermal shock zone, RDI correlates with the low-temperature solid state reduction zone, and RI relates to the medium-temperature solid state reduction zone. Table 3.1 shows the preferable physical and metallurgical property ranges for sinter, pellet and lump feed globally as well as the typical values produced by Kumba Iron Ore Ltd. These properties, affecting the lump zone of the blast furnace, will be investigated during this study.

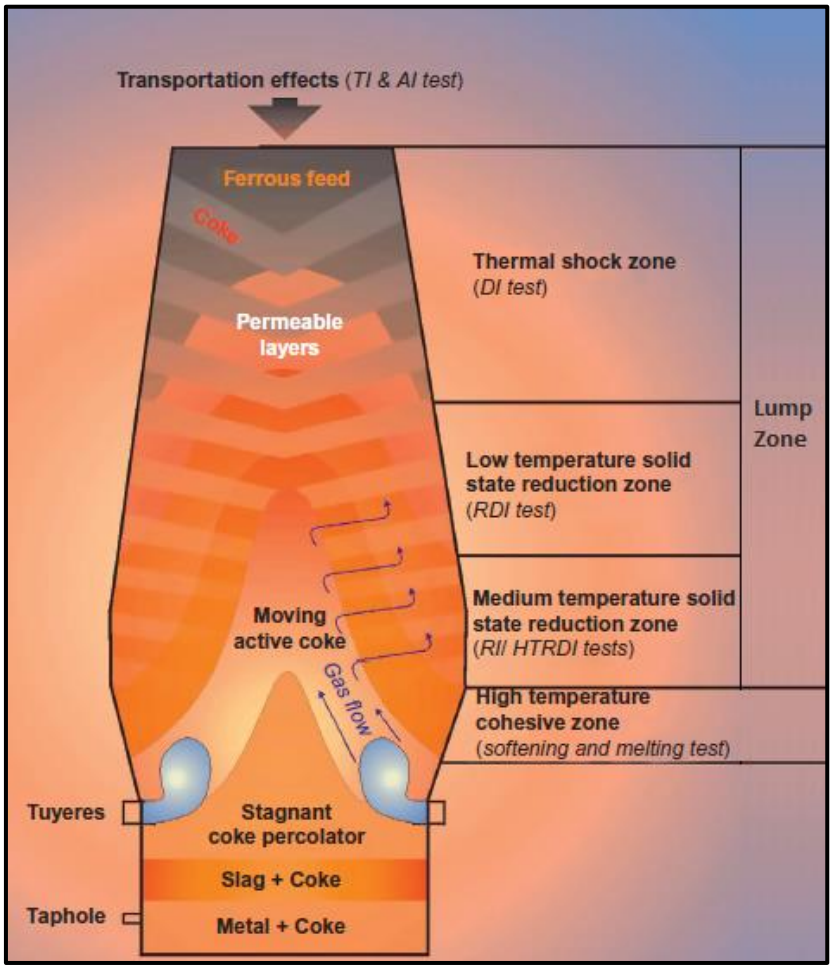

Figure 3.1 Cross-section of the blast furnace, showing the zones simulated by various tests, after (Clout and Manuel, 2015)

Table 3.1 Metallurgical and physical properties for sinter, pellet and lump feed. KIO: Kumba Iron Ore Ltd

	Description	Values	Preferred range				Source
			Sinter	Pellet	Lump	Typical KIO lump values	
TI/AI	Size distribution after tumbling	%>6.3 mm %<0.5 mm	>65 <7	>90 <3	>80-85 <10	92 4	(Barlow, 2018; Lu *et al.*, 2015)
RDI	Size distribution after reduction and tumbling	%>6.3 mm %<3.15 mm %<0.5 mm %>2.8 mm	<20 <35	>80 <10 N/A	<10* <25	6-8	(Barlow, 2020, 2018; ISO4696 as cited in Geerdes *et al.*, 2015; Lu *et al.*, 2015)
RI	Loss in weight with reduction	% oxygen lost after 180min	>65	>70	>60	36-41	(Barlow, 2018; Lu *et al.*, 2015)
DI	Mass proportion of material of testing	% <6.3 mm	N/A	N/A	<15	<2	(Barlow, 2018; Lu *et al.*, 2015)

*RDI values of <10% are the preferred Kumba Iron Ore lump standard, as tested in 2019. Typical global values range between 15-20% (Barlow, 2020)

The free swelling index is often measured in pellet ore. This is because pellets may significantly increase in size (or swell) as reduction takes place. This leads to greater volume, lower pellet strength and a subsequent increase in fine generation (Lu, Pan and Zhu, 2015). As KIO does not produce a pellet product, this property will not be further discussed in this research study.

In Figure 3.1, the high-temperature cohesive zone exists from the point where material softens and deforms to the point where liquid drips into the lower part of the blast furnace (Clout and Manuel, 2015). Lu *et al.* (2015) points out that this is where FeO is reduced to Fe, which may in turn become carburized by carbon monoxide (CO). It is preferred that this zone be narrow, with the base of the zone as low as possible. The metallurgical properties of ore in this zone are measured using the softening temperature (which should preferably be high), as well as the dripping temperature (which should be low).

Metallurgical ore properties do not play a major role below the high-temperature cohesive zone as the softening and melting process reduces the metallurgical variability of ferrous materials (Lu *et al.,* 2015). In the lower section of the blast furnace, the chemical composition is the main factor affecting operation. It influences the amount of metal and slag that are produced in the furnace and may also affect blast furnace operation and the quality of steel produced. Table 3.2 lists the effects of various elements in the blast furnace, which range from altering steel properties and inhibiting blast furnace production to creating adverse environmental conditions.

Table 3.2 The Effects of Contaminants on Blast Furnace Operation and Steel Production, after (Clout, 1998), as cited in (Clout and Manuel, 2015)

Contaminant	Acceptable Upper Limit in Iron Ore Feed	Geological Source	Effects
Carbonates		Banded ironstone formation (BIF), hydrothermal alteration, leaching	CO_2 is released during calcination of the ore, resulting in higher porosity in sinter and pellets. This leads to lower overall strength.
Clay	5%	Aluminosilicates in BIF and weathered shale	Alumina increases the melt viscosity, leading to the reduced strength of sinter and pellets
Alkalis, including potassium oxide (K_2O) and sodium (Na)	0.09 %K_2O	K_2O is derived from micas and stilpnomelane in BIF. Na can be introduced by groundwater.	Forms concretions which corrode the blast furnace refractory bricks. It also lowers the ore melting temperature.
Phosphorus (P)	0.08%	Commonly occurs as apatite	Causes brittleness in steel (Fordyce, 1860). It is not removed in slag and thus its removal adds to the cost of producing the cast iron.
Alumina (Al_2O_3)	2.8%	Aluminosilicates in BIF, and shale	Results in higher melt viscosity, which may block slag tapholes. Additionally, higher fuel costs are incurred.
Silica (SiO_2)	5%	BIF and shale	Higher amounts of slag are produced. Additional limestone flux must be added to the blast furnace
Manganese (Mn)	0.9%	Carbonates in BIF, precipitation from adjacent dolomite	Ore containing excessive amounts of Mn must be blended with lower-Mn ore
Copper (Cu)	100 ppm	BIF, hydrothermal alteration	Results in excessive, environmentally-damaging, dioxin formation. Ores with excessive amounts must be blended with low-Cu ore.
Chlorine (Cl)	500 ppm	Groundwater	Increases dioxin and nitrous emissions, which are environmentally hazardous. Causes damage to the blast furnace refractory brick lining.
Sulphur (S)	0.08%	BIF, organic sulphur in near-surface deposits	Increased amounts of harmful sulphur emissions. Additional magnesium oxide (MgO) must be added to the furnace to bond with S in the slag.
Titanium (Ti)	1.0%	Shale, intrusives containing ilmenite	Decreases the strength of pellets and sinter

3.1.1 Tumble and abrasion index

Abrasion index and tumble index are both used to quantify the extent to which the ore breaks down with impact and abrasion, which takes place during handling and transport. Particles can either be broken down by volume breakage or surface breakage processes, as illustrated in Figure 3.2. During volume breakage, the particle breaks along internal fractures, resulting in angular particles of varying sizes (Menacho, 1986). Surface breakage results from the slow wearing away, and chipping, of the surface of the particle (Menacho, 1986). This results in the rounding of the original particle, and predominantly fine degradation particles.

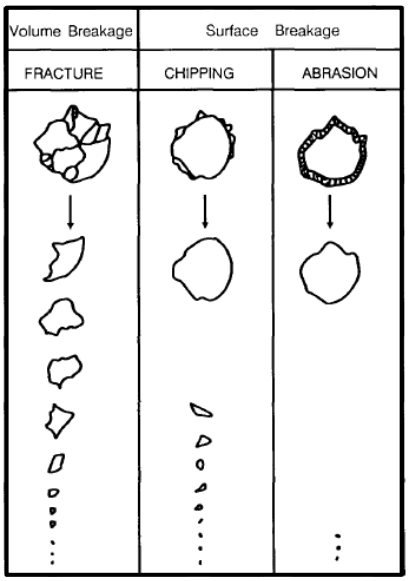

Figure 3.2 Different methods of particle breakage (Menacho, 1986)

As stated by Teo, Walters and Nicol (1990), the most common form of breakage during handling and transport is volume breakage. This is due to material being repeatedly dropped from heights above several meters during loading, stockpiling, stacking, reclaiming, and similar activities.

The abrasion and tumble index test involves rotating the iron ore sample in a drum for a specified amount of time, after which the sample is passed through sieves containing square openings of 6.3 and 0.5 mm (International Organisation for Standardisation 3271, 2015). The abrasion index provides a measure for the mass proportion of material that is <0.5 mm after handling, whereas the tumble index indicates the mass proportion of material >6.3 mm after handling.

3.1.2 Decrepitation index

The decrepitation index quantifies the degree to which ore particles crack or shatter within the blast furnace, due to the sudden heat increase (Anderson, 2014). The shattered particles result in fines which reduce permeability and heat flow in the blast furnace. Additionally, iron may be lost from the blast furnace in the form of dust (Lu *et al.*, 2015).

As stated in the International Organisation for Standardisation 8371 (2015), the DI test involves heating a sample of iron ore to 700°C for 30 minutes, after which it is cooled down to room temperature. The sample is then screened using a sieve with square openings of 6.3 mm, and the DI reported as the mass proportion of material <6.3 mm in size.

3.1.3 Reduction-disintegration index

The crystal structure volume increases by about 10% when six iron atoms bonded to nine oxygen atoms are forced to change to six iron atoms bonded to eight oxygen atoms ($3Fe_2O_3 \rightarrow 2Fe_3O_4$) (Geerdes *et al.,* 2015). This reaction occurs at 400-700°C (Wu, S., Lio, X. and Wu, J., 2015) and weakens the crystal structure, after which particles break down and fines are generated. Once again, these fines inhibit heat flow, permeability and destabilise blast furnace operation. The degree to which ore breaks down is measured using the RDI.

The RDI test involves monitoring the fines generated through reduction, under similar conditions to those in a blast furnace. The sample is first heated to 500°C and then reduced with a gas containing CO, CO_2, H_2 and N_2 for 60 minutes (International Organisation for Standardisation 4696-1, 2015). The sample is then allowed to cool, tumbled in a rotating drum, and the size distribution is measured. RDI is then reported as the percentage of particles <3.15 mm in size.

3.1.4 Reducibility index

The RI measures how easily the iron ore particles are reduced. The ease at which oxygen is transferred has an impact on the amount of fuel needed in the blast furnace (Mochón, *et al*. 2013). Hematite and magnetite both reduce to wüstite easily, however the reduction from wüstite to iron differs greatly depending on the source mineral (Maeda and Ono, 1985). The reduction of wüstite to iron from hematite progresses

homogeneously and is relatively fast. Only a portion of the wüstite is surrounded by dense iron and remains unreduced at the end of the process (Maeda and Ono, 1985).

When material reduces from magnetite to wüstite and then iron, the majority of the wüstite grains are bound by dense iron from the initial stages of reduction, hampering the smooth progression of the reactions (Maeda and Ono, 1985).

The RI test involves reducing the sample at temperatures of 900°C, in the presence of gas containing CO and N_2, for 180 minutes (International Organisation for Standardisation 7215, 2015). The degree of reduction is then calculated using the proportion of oxygen mass lost after the test.

4 Geometallurgy

4.1 What is Geometallurgy?

"Modern geometallurgy" is a relatively new area of interest within the mining industry, arising in the early 2000's (Williams, 2013), and offers a plethora of benefits throughout the mining value chain, and ultimately to the net present value (NPV) of a deposit. Modern geometallurgy incorporates several disciplines, including geology, mining, geotechnical engineering and metallurgy, to create a spatially representative 3D block model which optimises the NPV of a project, reduces risk and builds resilience (Dominy, O'Connor, Parbhakar-Fox, Glass, and Purevgerel, 2018 a). It minimises the difference between planned and actual mine performance with regards to production, recovery and revenue (Hunt and Berry, 2017). The aim of modern geometallurgy is to build a 3D model that not only predicts ore grade and lithologies being mined and sent to the plant, but also metallurgical and physical variables that could affect downstream processing.

Pure "metallurgy" derives the metallurgical and physical characteristics of ore via several tests of composited samples, considered to be representative of the entire ore body (Dominy *et al*., 2018 a). "Classical geometallurgy" improves on this practice by adding mineralogical knowledge to plant operations, but still uses a set of average characteristics to represent the ore body. In reality, the spatial variability of the ore body results in sub-optimal and unpredictable plant performance, (Ashley and Callow, 2000; Hunt and Berry, 2017; Lund and Lamberg, 2014). Modern geometallurgy characterises the spatial variability of the ore body, as well as waste lithologies, while consulting other disciplines in the mine value chain. The result is a geometallurgical model that accounts for geological variations that affect geological, geotechnical, physical, metallurgical and mining objectives.

Modern geometallurgy will become critical to ensure the success of mining companies in the future. Dominy *et al.* (2018a) outlines several challenges that will benefit from a geometallurgical input, including:

- More complex ore bodies will be mined, as higher-grade and easily accessible deposits are depleted. Challenges herewith include lower ore grades,

geometrically intricate ore bodies, processing problems and deep ore bodies with higher geotechnical complexity.

- Higher stripping ratios results in the generation of more waste, which needs to be managed with minimal impact to the environment.
- Increased electricity and water costs
- More stringent requirements on the “social license to mine”
- Commodity price fluctuation

Geometallurgical programs have recently proven successful on several mines and exploration projects, as summarised in Table 4.1. These examples show how geometallurgy can mitigate project risk, increase NPV and reduce operating costs.

Worldwide mining industry circumstances are changing at a rapid rate. It is no longer enough to assume that following the same mining method as the previous few decades will keep companies in business over the following decades. Geometallurgy will play a critical role in adapting mindsets and mine processes to optimise the way resources are utilised.

4.2 Modern Geometallurgy

The modern geometallurgy discipline can be subdivided into two main fields: strategic and tactical geometallurgy. Strategic geometallurgy has a longer-term focus and plays a role during the entire life of mine, from exploration, development, planning to mine closure and rehabilitation (McKay, Vann, Ware, Morley and Hodkiewicz, 2016). It uses information derived from drilling, test work and modelling and is updated by adding information acquired during the tactical geometallurgy program (Dominy *et al.*, 2018 a). The strategic geometallurgical block model can then be used to create an optimal mine plan, generate production forecasts, identify efficient metal extraction methods, and predict cash flows over the life of mine.

Table 4.1 Summary of the successful implementation of geometallurgy programs at existing operations

Mine	Type of Deposit	Geometallurgical Input	Outcome	Reference
La Colosa, Columbia	Copper-poor, porphyry gold	GeM comminution index tests were used to derive A x b (impact breakage) and BMWi (grindability) values. Differing comminution response values were correlated with albite, chlorite, magnetite and density.	The first 3D model of comminution variability within La Colosa was developed. The information can be used to optimise mill designs during the feasibility stage of the deposit.	(Montoya, Keeney, Jahoda, Hunt, Berry, Drews, Chamberlain and Leichliter, 2011)
Collahuasi, Chile	Copper	Specific power consumption values for grinding circuits varied according to lithology and alteration type.	Geometallurgical data was incorporated into the production model. This allowed planning engineers to optimise ore treatment capacities based on the ore types blended into the grinding circuit.	(Alruiz, Morrell, Suazo and Naranjo, 2009)
Not specified	Diamond – kimberlite pipes	Historical relationships between different kimberlite ores and processing response were analysed for trends. Hardness was correlated with the proportion of material expected to report to oversize, grits and slimes in the mills.	The historical relationships were used to predict future plant performance and alter blends to ensure production targets are met. Hardness was used to predict the average size and mass of particles sent to the dense media separation (DMS) plant.	(Lechuti-Tlhalerwa, Coward and Field, 2019)

Mine	Type of Deposit	Geometallurgical Input	Outcome	Reference
Noligwa Mine, South Africa	Gold	Gold recoveries from the Vaal and C-Reefs were correlated to the gold grain size, and the proportion of exposed surface area, after milling.	It was decided that the existing plant, designed to process ore from the Vaal Reef, is suitable for the processing of ore from the new C-Reef. Certain situations may warrant a finer milling size, or longer cyanide retention phase, to ensure optimal gold extraction. The study suggested altering blast practices to prevent finer-grained gold from being lost during mining, resulting in low mine call factors.	(Pienaar, D. Guy, Pienaar, C. and Viljoen, 2017)
San Antonio Project, South America	Gold	Two zones exhibiting different gold recovery potentials were identified: quartz and sulphide-hosted gold. Uniaxial compressive strength (UCS) and bond ball mill work index was correlated with EQUOtip values. This was then used to predict comminution performance. GRG (gravity recoverable gold) is calculated by multiplying head grade with the GRG recovery fraction. Flotation recovery was correlated with pyrite content of the ore. Sulphide distribution is determined by sulphur, lead and zinc assays. Density was found to be controlled by sulphur content.	A 3D geometallurgical model predicting ore variability was created. The ore control model contained information regarding grade, GRG, sulphide content, ore density and ore hardness. The model, created during the prefeasibility study, helped inform an early start-up mining scenario consisting of a low-capital expenditure selective narrow-vein operation, with a more sustainable footprint compared to other mining scenarios.	(Dominy, O'Connor, Glass and Xie, 2018b)

Mine	Type of Deposit	Geometallurgical Input	Outcome	Reference
Nkout (Cameroon) and Putu (Liberia) deposits	Iron	Recovery of iron minerals was found to be dependent on modal mineralogy, grain size, mineral associations.	Optimum beneficiation methods were suggested for lower-grade BIF samples, based on its mineralogy. Goethite and andradite were identified as minerals that could potentially cause discrepancies in iron recovery. The optimal grind size for beneficiation was identified.	(Anderson, 2014)
Malmberget Mine, Sweden	Iron	Ore was classified according to modal mineral composition as well as various mineral textures	Ore textures and modal mineral composition were used to create a geometallurgical model that predicts metallurgical responses, including the way that ore will break and the resulting particle types.	(Lund, Lamberg and Lindberg, 2015)
Ruashi Mine, Democratic Republic of Congo	Copper and cobalt	Ore was characterised according to several factors that affect ore processing and recovery, including • The amount of talcose material in the feed, which lowers feed density, plant throughput and recovery • The amount of ore from the black mineralised ore zone (BMOZ) which increases the manganese content in the electrowinning circuit, causing a decrease in recovery	A stockpiling strategy was derived whereby ores exhibiting different geometallurgical characteristics were stockpiled separately. This allowed for the blending of different ore types to ensure a consistent feed to the plant. The initial life of mine (LOM) plan did not produce the cash flow required to keep the mine profitable each year, which was worsened by declining cobalt prices. The new LOM plan, incorporating the	(Macfarlane and Williams, 2014)

Mine	Type of Deposit	Geometallurgical Input	Outcome	Reference
		• The amount of dolomitic ore in the feed. Higher amounts of this ore require more acid in the leach circuit, increasing processing costs	geometallurgical ore variability and stockpiling, allowed for a blending strategy that kept the mine profitable each year, and ultimately added US$127 million to the project's NPV.	
Mikheevskoye Mine, Russia	Copper-gold	Process performance was correlated to ore hardness, oxidation and presence of magnetite. Thirteen geometallurgical domains were identified, based on these characteristics.	A potential mining scenario was calculated, taking geometallurgical domains into consideration. This scenario accounted for variability in ore processing costs and decreased the project's payback period by 1.5 years. The NPV was also significantly increased.	(Lishchuk, Koch, Lund and Lamberg, 2015)

During the tactical geometallurgy program, the strategic and short-term ore control models are applied in order to optimise mine processes (Dominy *et al.*, 2018 a). These include optimised drill and blast patterns, optimised crusher and plant settings, as well as predicting the market value of each mining block. The tactical model uses information from the strategic geometallurgical model and from ore control drilling. This model is updated several times throughout the year, depending on how often ore control information is received, and is focused on the shorter-term mine processes (Dominy *et al.*, 2018 a).

Characterising ore according to TI, AI, RDI, DI and RI will affect both the strategic and tactical geometallurgical models. It will allow for long-term forecasts of ore quality and revenue prediction across the life of mine. Additionally, the data can be used to quantify the value of each mining block in the short-term and enable ore to be blended according to customer requirements.

4.3 Primary-Response Variable Relationships

Geometallurgical modelling is complex for several reasons. Firstly, the lack of geometallurgical practices in the past, and expense associated with collecting data, results in a sparse amount of data available for modelling. Once data is collected, the next hurdle becomes the non-additivity of metallurgical and physical response variables.

One method of overcoming the non-additivity problem, outlined by Coward *et al.* (2009) is to define a relationship between primary and response variables. This will allow additive primary variables to be modelled and used to predict non-additive response variables. Coward *et al.* (2009) defines primary variables as inherent rock characteristics that are not affected by downstream processes; while response variables are rock characteristics that define how the rock will react to downstream processes, such as beneficiation and smelting.

The primary-response modelling approach contains two main criteria (Sepulveda, Dowd, Xu and Addo, 2017):

- A relationship with a good prediction performance must be selected.

- Identify the top key variables that will most accurately predict response variables. This is in efforts to reduce dimensionality of geometallurgical data and create simpler, more accurate models.

One of the more popular models that uses relationships to predict a variable from one or more input variables is regression (Friedman, 1994). Linear regression can be subdivided into three main techniques (Rencher and Christensen, 2012):

- Simple linear regression. Here there is only one *y* and one *x* variable. For example, predicting the hardness of a sample based on the %Fe content.
- Univariate multiple linear regression. This technique is applied to cases where there is one *y* variable and several *x* variables. For example, predicting the hardness of a sample based on the %Fe content and ore texture.
- Multivariate multiple linear regression (MLR). Here there are multiple *y* variables and multiple *x* variables. For example, predicting ore hardness in terms of crusher work index and uniaxial compressive strength, using independent variables such as %Fe content and ore texture.

MLR is commonly used in fields including financial engineering, psychometrics and chemometrics (Yuan, Ekici, Lu and Monteiro, 2007). However, it is limited to variables displaying strongly linear relationships.

In MLR, there are generally *n* observations. Of these, there are *q* responses (dependant variables plotted on the y-axis) and *p* explanatory variables (plotted on the x-axis) (Yuan *et al.*, 2007). The equation used during MLR is:

$$Y = XB + E \quad (1)$$

where Y is based on an *n x q* matrix and X is based on an *n x p* matrix. *B* is a coefficient of *p x q* and *E* is the regression noise, which is an unobserved random variable (Yuan *et al*., 2007).

Principal component analysis (PCA) often provides a starting point for multivariate analysis (Wold, Esbensen and Geladi, 1987). It predicts *X* based on the matrices of *T* and *P'*. PCA was first described by Pearson (1901) as "lines and planes of closest fit to systems of points in space".

An example of the primary-response framework technique can be seen in a study by (Keeney and Walters, 2011). PCA was used to transform multidimensional data and plot it onto a two-dimensional scatter plot. This allowed the definition of nine geometallurgical domains, each fitted with regression models exhibiting high coefficients of determination (R^2). As a result, mineralogy and assay data could be used to predict specific comminution characteristics.

Hunt, Berry, Bradshaw, Triffett and Walters (2014) performed batch flotation testing on 24 archetype samples to determine copper recovery. They divided the sample assay data for the archetypes into two groups: high-Fe low-Al and low-Fe high-Al, which also gives an indication of the mineralogy of the samples. Modelling these two groups separately to predict copper performance resulted in R^2 values of 0.69 for the low-Al high-Fe group and an R^2 value of 0.79 for the high-Al low-Fe group. These strong linear relationships allowed for copper recovery predictions to be made across all on-site assay samples.

Choosing a modelling technique depends on the unique characteristics of each project, and there is no set method in finding the most appropriate technique (Sepulveda *et al.*, 2017). Primary and geometallurgical response variables are typically non-linear and would necessitate a non-linear regression method (Sepulveda *et al.*, 2017). These include polynomial regression, projection pursuit methods and machine learning (Friedman, 1994).

Projection pursuit regression (PPR) was developed by Friedman and Tukey (1974) to aid exploratory data analysis, and Sepulveda *et al.* (2017) used this technique to model geometallurgical response variables. Sepulveda *et al*. (2017) demonstrated that the PPR method more accurately predicts response variables than MLR, and estimates the uncertainty associated with these variables.

Projection pursuit (PP) is a form of linear transformation that centres on projections. PCA, on the other hand, is a linear transformation method that focuses on orthogonal global transformation (Sepulveda *et al.,* 2017). PP is used to identify optimal directions on which multidimensional data can be plotted. This reveals useful information on data trends, without the need to reduce data to a low-dimensional space to facilitate human interpretation (Sepulveda *et al.,* 2017). The equation used during PP is:

$$p = \alpha^T * X \tag{2}$$

where α^T is the direction of the normalised vector, *p* is the projection and *X* is the observation.

PPR accommodates non-linear relationships by combining multiple linear combinations of smoothed projections (Sepulveda *et al.,* 2017). It uses a projection of the data, instead of raw input, after which the projection is smoothed to identify the main data trend.

As outlined by Sepulveda *et al.* (2017), there are five ways to measure how well a regression model fits the data. These include the correlation coefficient (R), coefficient of determination (R^2), root-mean-squared error (RMSE), mean absolute error (MAE), and the mean error (ME). An R value of close to -1 or +1 shows that the model predicts the response variables well and R^2 values of close to +1 shows that the model fully explains the variance of the true value and indicates a reliable model. RMSE and MAE give indications of the prediction error, while ME states the amount of bias in the prediction, with a "0" value indicating no biases.

4.4 Identifying Primary-Response Variable Relationships

In this study, several response variables affecting blast furnace operation are investigated, including the TI, AI, DI, RDI and RI. The response variables are compared to primary geological variables (including ore texture, mineralogical content and grade) to identify correlations between the two. It focuses on the acquisition of geometallurgical data and subsequent class-based analysis. Metallurgical and physical characteristics are then assigned to all exploration drill holes (300+) on the Kapstevel South farm based on their primary geological variables. In this way, the need for costly and timeous metallurgical and physical testing on exploration drill holes is reduced without compromising the density of geometallurgical data. Thereafter, the geological model containing primary variables is used to infer metallurgical and physical response variables across the Kapstevel South farm and inform the mine's first geometallurgical model.

Several factors are thought to affect physical and metallurgical properties of iron ore at KIO. Mineralogy and texture have been found to play a vital role in the way ore responds to processing (Lund *et al*., 2015; Schouwstra and Smit, 2011; Yildirim, Bradshaw, Powell, Evans and Clark, 2014), making it an important variable to investigate during this study. It is also possible that iron ore grade influences the response variables as it is an indicator of mineralogy, for example increased phosphorus contents signalling the abundance of

apatite or other phosphorus-containing minerals. A geometallurgical study at Anglo American's Mogalakwena Mine has indicated correlations between calcium and the metallurgical responses of the ore (Schouwstra, Vaux, Muzondo and Prins, 2013). In addition, (Gordon, Miller and Becker, 2018) found relationships between three early-stage geometallurgical domains and the following response variables: liberation, mill throughput, flotation grade, recovery and selectivity. Higher iron concentrations are correlated with increased relative density at Kolomela Mine, which may also affect the response variables.

4.4.1 Factors affecting metallurgical and physical ore characteristics – a review

Although much is known about the way iron ore chemistry affects blast furnace operation, the reasons for metallurgical and physical variations of iron ore has not been investigated until fairly recently (Clout, 2003; Clout, Maré, Ilich, Brandli and Bradley, 2007; Cores *et al.*, 2010; Geerdes *et al.*, 2015; Hsieh, 2005; Muwanguzi *et al.*, 2012; van der Vyver, Pistorius, Brand, and Reid, 2009; Wu, Xu, Tian, 2009). This gap in knowledge indicates room for further optimisation and efficiency improvements in blast furnace operation and reinforces the need for modern geometallurgy. The following section summarises some of the geometallurgical iron ore characterisation performed to date.

Tumble and abrasion index

Clout, Maré, Ilich, Brandli and Bradley (2007), as cited in (Clout and Manuel, 2015), found a correlation between ore hardness and degree of breakage to fines. This correlation was investigated by conducting drop tests on run-of-mine (ROM) lump samples and the outcomes are displayed in Figure 4.1. The greatest amount of disintegration occurs during the first drop, after which the break-down rate slows down in all three hardness types. Overall, hard iron ores are expected break down the least during transport, exhibit higher TI with lower AI, and yield the highest lump to fine ratios.

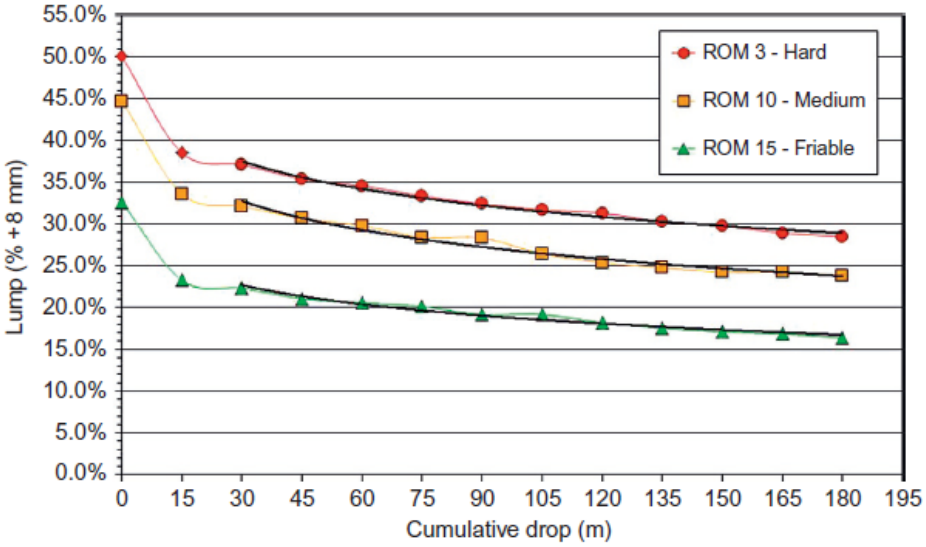

Figure 4.1 Lump yield after drop tests, simulating material disintegration during transport and handling. Lump yields calculated from the crushing and screening of ROM feed (Clout et al., 2007), cited in (Clout and Manuel, 2015)

Clout and Manuel (2015) indicate a correlation between hardness and the predominant iron minerals in the ore (displayed in Figure 4.2). Here, hematite occurs across a range of hardness values, whereas goethite typically exists as softer ore with higher porosity. This hardness is then further affected by the texture, degree of secondary leaching and porosity of the ore. Low porosity leads to increased ore hardness, resulting from the strong interlocking textures of iron minerals (Clout and Manuel, 2015). Similarly, the strength of the ore matrix bonding components of sinter feed has been found to play a major role in the TI of the sinter (Mochón *et al*., 2013).

Larger grain structure is thought to negatively affect tumble index, as they generally contain larger impurities that break upon impact (Muwanguzi *et al.,* 2012).

	Main ore minerals			
Hardness	Hematite	Hematite-goethite	Goethite-hematite	Goethite
Hard	✓	✓	✓	
Medium	✓	✓	✓	✓
Friable	✓	✓	✓	✓
Powder/dust	✓		✓	✓

Increasing hardness ↑

Increasing porosity ↓

Increasing hematite content ←

Figure 4.2 Hardness variation across the main iron ore minerals (Clout and Manuel, 2015)

Decrepitation index

DI is most significant where water is present within the structure of iron minerals, such as goethite (Clout, 2003). Moisture and carbonate minerals have also been correlated with increased DI (de Azevedo and Cardoso, 1983). Upon heating in the blast furnace, the phase transformation of oxides around 700 °C results in volume changes in the ore particles, creates stress and results in the formation of cracks (Faria, Vianna, Jannotti and Vieira, 2010).

Porosity is also known to have an effect on DI. Lu *et al*. (2015) shows that ores exhibiting higher porosity levels do not decrepitate as much as lower-porosity ores. This is true even when porous ores contain greater loss on ignition (LOI).

Ores created by thermal processing, such as pellets and sinter, do not yield problematic decrepitation indices (Lu *et al*., 2015). Therefore, the property is only monitored in lump ores.

Reduction-disintegration index

This phenomenon is particularly common in sinter and lump ores and is dependent on the bond strength between particles (Geerdes *et al.,* 2015). Reduction-disintegration is not problematic in pellets as about 30% of their structure is made up of voids which accommodate expansion of the crystal structure (Geerdes *et al.,* 2015).

Geerdes *et al.* (2015) suggests several factors that affect lump ore and sinter RDI, including the chemical and mineralogical composition of the ore. For example, alumina and magnesia lower the bond strength within the ore. However, studies such as those conducted by Hsieh (2005) indicate that high alumina ore may result in a wide range of RDI values. Additional factors, such as texture, may contribute to the varying RDI values with alumina in Hsieh's study.

The proportion of FeO in the ore, which is related to magnetite content (Fe_3O_4, corresponding to $FeO{\cdot}Fe_2O_3$) is also known to affect RDI (Geerdes *et al*., 2015). The initial hematite-magnetite reduction reaction has less of an impact on crystal structure with increasing FeO content. Although a slight increase in FeO content of sinter improves the material's RDI, it has a negative effect on reducibility (Cores *et al.,* 2010). The reduction

of secondary hematite is more destructive to crystal structure than that of primary hematite (Mochón *et al*., 2013), making this mineral less-favourable.

Increased grain size, lower porosity, orientation of grain structure, interconnected large pores, and hydrous minerals result in an increased RDI (van der Vyver *et al*., 2009).

Additionally, van der Vyver *et al.* (2009) confirmed that cracking in the blast furnace can be caused by reduction, and that gangue minerals affect fracture density and orientation. However, gangue contents do not correlate with RDI and cannot be used as a proxy.

Reducibility index

The RI is largely dependent on the porosity and mineralogy of particles (Anderson, 2014; Clout, 2003; Fernández-González, Ruiz-Bustinza, Mochón, González-Gasca, and Verdeja, 2017; Muwanguzi *et al.,* 2012). Porous goethite, for example, would exhibit a higher RI than the dense hematite ore. Porosity increases the available surface area on which reduction can occur. Although a high proportion of FeO is favourable for RDI, it has adverse effects on the RI (Cores *et al.,* 2010).

More hematite than magnetite is also preferred for improved sinter reducibility, and general quality (Fernández-González *et al.,* 2017; Maeda and Ono, 1985). Calcium ferrite is known to reduce easier than wüstite and results in porous iron that does not hamper further reduction (Maeda and Ono, 1985).

Physical and metallurgical properties of lump ore

Clout (2003) subdivides lump ore quality based on the iron minerals and textures that make up the ore (Table 4.2). These TI, AI, DI, RDI and RI values are all relative. Microplaty hematite comprises a network of 10-200 µm hematite plates that form via the replacement of silicate and carbonate bands in the original BIF (Morris, 1985).

Table 4.2 Metallurgical and physical properties per ore group (Clout, 2003)

Ore group	Tumble Index	Abrasion Index	Decrepitation Index	Reduction-Disintegration Index	Reducibility Index
Dense martite/hematite (P)	High	Low	Low	Low	Medium
Microplaty hematite (P)	Low to medium	High to medium	Very low	Medium to high	High
Martite-goethite (P)	Medium	Medium	Medium	Medium	Medium
Goethite-martite (P)	Low to medium	High to medium	Medium	Medium	High
Dense hematite/martite/hydrohematite (D)	Very high	Low	Very high	Low	Medium
Dense martite-geothite (H)	High	Low	High	Medium	Medium
Dense goethite-martite (H)	Medium	Medium	High	Medium	Medium
Microplaty hematite-goethite	Medium	Medium	Medium	High	High
Ochreous goethite (H-P)	Low	High	Low	High	Very high
Vitreous goethite (H)	Medium	Medium	Medium	Medium	High

Origin type: P-primary, H-hydrothermal, D-deydration

Lump ore is a low-cost alternative to pellets and is generally thought to exhibit poorer and more variable physical and metallurgical properties. As stated by Geerdes *et al.* (2015), lump ore differs to pellets in that it:

- Shatters or breaks at the top of the blast furnace as crystalline water evaporates.
- Exhibits poorer AI, TI, RDI and RI properties. A study conducted by Wu *et al.* (2009) contrasts this statement by showing that lump ores generally exhibit higher RI properties than pellets.
- Exhibits a lower melting temperature
- The physical and metallurgical properties are more variable, and thus unpredictable

According to Geerdes *et al.* (2015), higher melting temperatures are preferred because material that melts too early forms impermeable layers within the blast furnace.

However, a study conducted by Wu *et al.* (2010) contrasts with Geerdes *et al.* (2015). It rates the metallurgical and physical properties of lump ore as very similar to that of pellets

and concludes that there are few disadvantages to substituting pellets for lump in the blast furnace. Furthermore, lump advantageously consumes less energy during its creation, making it more environmentally sustainable. The difference in opinion may be due to the vast range of metallurgical and physical properties of lump iron ore, which depend on its in-situ geological properties.

As sinter, lump and pellets offer specific advantages and disadvantages in the blast furnace, the materials are often blended to minimise the disadvantages of each ore type (Geerdes *et al.,* 2015). For example, the effects of higher sulphur and phosphorus levels in lump ore are negligible due to the lower proportion of lump used in the blast furnace (Wu *et al.,* 2009).

According to (Geerdes *et al.,* 2015), maximum lump proportions of 10-15% in the blast furnace generally promotes higher productivity. This varies with lump quality, however. Certain Chinese blast furnaces use lump proportions of up to 20% without any adverse effects on production and economic results (Wu *et al*., 2009). Wu *et al.* (2009) recommends using a proportion of 25% lump in the blast furnace. This would reduce costs without compromising on production or the quality of metal produced. The study performed by Wu *et al.* (2009) also emphasises the importance of selecting the right type of lump ore for the blast furnace burden. It is important that the lump (and other burden materials) provided to the blast furnace is consistent, ensuring smooth furnace operation with minimal interferences (Fernández-González *et al.,* 2017).

Van der Vyver *et al.* (2009) studied the disintegration of several lump ore samples from the Northern Cape iron ore bodies, consisting of a mixture of brecciated, laminated, massive and conglomeratic ore textures. The mixture of ore types prevents the determination of proxies between ore textures and disintegration. However, van der Vyver *et al.* (2009) notes that the significant variation in samples, containing different mixtures, indicate that lump disintegration can be predicted through the careful blending of ore textures.

Producing lump ore with consistent and predictable metallurgical and physical properties would minimise the disadvantages associated with this ore type and encourage its low-cost use in the blast furnace. This study aims to promote this practice at Kolomela Mine and consequently enhance company reputation within the iron ore market.

Although several correlations have been identified between a specific physical or metallurgical property and a rock characteristic (for example alumina content, porosity, fracture density), there is limited literature assigning certain rock characteristics with a set range of physical or metallurgical properties. During this research project, correlations between rock characteristics (texture, grade and mineralogical content) and metallurgical/physical properties affecting blast furnace operation (TI, AI, DI, RDI and RI) are investigated.

5 BIF-Hosted Iron Ore Deposits

Considering worldwide iron metal systems, iron ore hosted in Banded Iron Formation (BIF) plays the biggest role in terms of iron ore production and reserves worldwide (Hagemann *et al.*, 2016). This is followed by channel iron deposits (CIDs) where iron ore was deposited along Tertiary-aged rivers channels, and magnetite-apatite ores (Clout, 2006). This section outlines the different types of BIF-hosted iron ore deposits and the factors affecting their enrichment to mineable ore deposits.

5.1 The Formation of BIF-Hosted Iron Ore

BIF-hosted iron ore comprises iron ore that is found within, or formed from, BIF protore. Iron formation is defined as a laminated, chemical sedimentary rock containing alternating layers of chert and iron, exhibiting chemistry values of at least 15 wt% iron (Beukes and Gutzmer, 2008). BIF is thus a type of iron formation that contains well-defined chert layers.

When comparing the iron ore deposit to the BIF host, the geology and mineralogy are similar. The iron ore body usually contains higher proportions of hematite or magnetite and fewer contaminant elements within the iron oxide bands (Clout, 2006). BIF itself is not usually mined as iron ore due to the typically low iron grades. BIF protore must first be enriched, from on average 30 to 35 wt% Fe (Klein, 2005), via several processes to result in a mineable ore reserve.

The major iron ore districts are confined to the Precambrian era, along Proterozoic mobile belts and Archean cratons. As can be seen in Figure 5.1, South America and Australia host some of the most significant iron ore districts in the world. The Hamersley district in Australia, and the Quadrilátero Ferrífero, Carajás and Corumba-Urucum districts in Brazil are the most significant, each hosting more than 15 Gt of iron ore. These deposits also offer some of the best quality ore in terms of Fe wt.%. Smaller deposits in the North of South America, West Africa and in North America, exhibit poorer iron grades and would result in less contained iron. Evidently, there is a vast difference between the grade and size of deposits in South America and Australia versus the rest of the world. Table 5.1 provides the details of these differences worldwide (Hagemann et al., 2016). The few companies who mine the giant deposits thus have a significant competitive advantage in

the global iron ore market, producing large quantities of high-grade iron ore and taking full advantage of economies of scale.

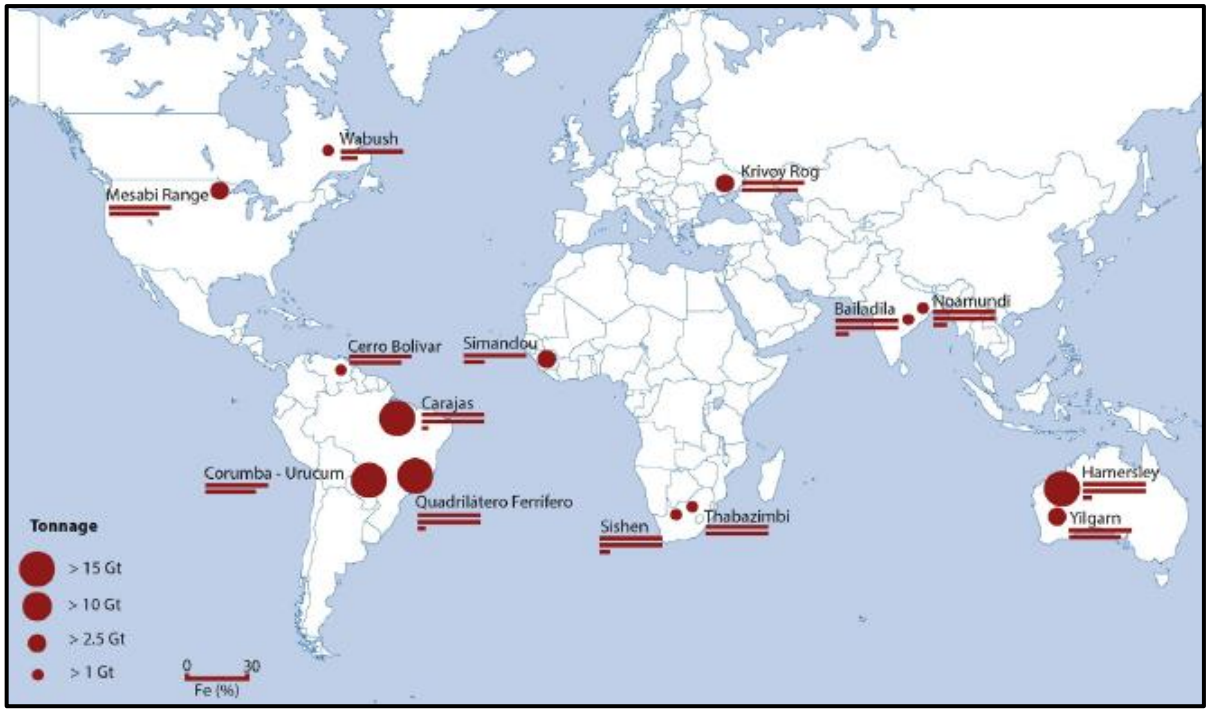

Figure 5.1 Major iron ore districts and deposits worldwide (Hagemann *et al.*, 2016)

Table 5.1 Major iron ore districts and deposits worldwide, after (Hagemann *et al.*, 2016)

Deposit/District Name	Country	Major Current Owner	Tonnage (Gt)	Fe (%)	Reference
Corumba-Urucum	Brazil	Vale	36	54.0	(Urban, Stribrny and Lippolt, 1992)
Hamersley District	Australia	BHP Billiton, Rio Tinto, FMG	19.2	64.0	(Thorne, Hagemann, Webb and Clout, 2008)
Quadrilátero Ferrífero	Brazil	Vale	17.5	64.0	(Rosíere, Spier, and Rios, 2008)
Carajás	Brazil	Vale	16.0	63.0	(Figueiredo e Silva, Lobato, Rosiére, Hagemann, Zucchetti, Baars, and Andrade, 2008)
Noamundi	India	Tata Steel Ltd.	3.3	61.0	(Mukhopadhyay, Gutzmer, Beukes, and Hayashi, 2008)

Deposit/District Name	Country	Major Current Owner	Tonnage (Gt)	Fe (%)	Reference
Mesabi Range District	USA	ArcelorMittal S.A., Cliffs Natural Resources Inc.	3.6	54.0	(Hagemann *et al.*, 2016; Morey, 1999)
Cerro Bolivar	Venezuela	Commodities and Minerals Ltd.	3.0	55.0*	(Hagemann *et al.*, 2016)
Krivoy Rog	Ukraine	ArcellorMittal S.A	2.8	57.0	(Dalstra and Guedes, 2004)
Yilgarn	Australia	Cliffs Natural Resources Inc., Sinosteel Midwest Corp. Ltd.	2.5	55.0	(Angerer, Hagemann and Danyushevsky, 2012)
Simandou	Guinea	Rio Tinto	2.8	40.0	(Cope, Wilkinson, Boyce, Chapman, Herrington, and Harris, 2008)
Sishen	South Africa	Anglo American plc	1.7	64.8	(Beukes, Gutzmer and Mukhopadhyay, 2003)
Bailadila	India	NMDC Ltd.	1.0	66.5	(Mukhopadhyay *et al.*, 2008)
Wabush	Canada	Cliffs Natural Resources Inc.	1.2	38.0*	(Hagemann *et al.*, 2016)

*Minimum grade

As noted by Hagemann *et al*. (2016), four main features control the formation and characteristics of BIF-hosted iron ore deposits:

- geotectonism,
- fluid movement and pathways,
- depositional sites
- ore preservation or alteration.

5.1.1 Geotectonic controls

BIF can be found in three main tectonic settings, described in Table 5.2. Some of the largest iron ore deposits are found in the Lake Superior type settings, followed by Algoma and Rapitan-Urucum. Different lithological associations are found in each tectonic setting, which are also correlated to specific geological eras.

Table 5.2 Tectonic Settings of BIF deposits

	Tectonic/Environmental Setting	Approximate Age	Lithological associations	Examples	References
Algoma-type BIF	Convergent margins	Archaean and Paleoproterozoic	Interlayered with sub-marine volcanic rocks in granite-greenstone belts	Yilgarn and Pilbara deposits, and Carajás deposit.	(Angerer, Duuring, Hagemann, Thorne and McCuaig, 2015; Figueiredo e Silva *et al.*, 2008; Gross, Canada and Steet, 1980)
Lake-Superior type BIF	Passive margin	Proterozoic	Sedimentary lithologies	Hamersley and Transvaal (for example the Sishen) deposits	(Angerer *et al.*, 2015; Beukes and Gutzmer, 2008; Gross *et al.,* 1980)
Rapitan-Urucum type BIF	Associated with Snowball Earth events	Neoproterozoic	Sedimentary and glacial lithologies	Urucum deposit (Brazil)	(Hoffman *et al.*, 1998; Kirschvink, 1992; Klein and Ladeira, 2004; Urban *et al.,* 1992)

It is generally accepted that BIFs form in anoxic ocean environments (before the Great Oxidation Event - GOE - around 2.4 Ga), where iron is derived from marine hydrothermal activity or from continental sediments (for example Krapež, Barley and Pickard, 2003; Urban *et al*., 1992). Iron and silica are then precipitated in alternating layers to form BIF, with the intermittent precipitation of iron controlled by environmental redox and chemical conditions. Most BIF's (~35 wt% Fe), particularly Lake Superior-type BIFs, are then enriched to high-grade iron ore (>58 wt% Fe) after the GOE (Taylor, Dalstra, Harding, Broadbent and Barley, 2001).

Rapitan-Urucum BIFs are peculiar in that they formed nearly 1 Ga after the previously-deposited BIF, and in an oxygenated atmosphere. Kirschvink (1992) as cited in (Hoffman, Kaufman and Halverson, 1998) proposed that the Neoproterozoic BIFs likely formed as ocean environments were sealed and separated from the oxygenated atmosphere by glaciers. This anoxic environment facilitated the formation of younger BIFs.

5.1.2 Fluid movement and pathways

Silica is leached from BIF during its upgrade to an iron ore deposit. Upwards-moving, hydrothermal, chlorine-rich brines (around 150-250°C) are proposed to provide the medium for the removal of silica within the chert bands (Thorne, Hagemann, and Barley, 2004), after which the BIF was further enriched by supergene processes. However, Manning (1994) stated that quartz is less-readily dissolved as fluid temperatures are lowered, creating obstacles for the above low-temperature silica dissolution. The low-temperature constraint is compensated by the movement of large volumes (~$10^9 m^3$ for an iron ore deposit of $3x10^8$ m^3) of fluid with pH values above 9, resulting in the dissolution of silica across large BIF deposits (Evans, McCuaig, Leach, Angerer and Hagemann, 2013). Enhanced permeability is thus required in the region, which can form via several structural events, such as that proposed by McLellan, Oliver and Schaubs (2004). Here, extensional events and topography supplied the upward and downward-moving fluids necessary to create the Hamersley deposits in Australia. Essentially, the structural features must allow the movement of fluids from aquifers to BIF depositional sites where they react with and enrich BIF protore to form high-grade iron ore (Hagemann *et al*., 2016).

5.1.3 Depositional sites

High-grade BIF-hosted iron ore deposits are predominately formed from BIF protoliths already containing around 30-35 wt% Fe (Hagemann *et al.*, 2016). As summarised by Hagemann *et al.* (2016), the following deposition-related factors control the enrichment of BIF to high-grade iron ore:

- The structural setting of the deposit during enrichment
- The alteration zones resulting from hypogene activity, as well as the mineralogy and geochemistry resulting from supergene enrichment
- The hydrothermal fluids acting in the system

Structural setting

As previously stated, structural features provide a path for fluids to move to the BIF depositional site, but they also play a significant role in preserving the iron ore from erosion (Dalstra, Rosiére, and Hagemann, 2008). However, Hagemann *et al.* (2016) clarifies that random mineral orientation and the lack of structural fabric in most iron ore

deposits indicates that mineralisation usually occurs after the deformation events. Hagemann *et al*. (2016) describes how structures could either form before, during or after BIF enrichment, and could each play a role in the present-day iron ore deposit characteristics. Structures formed before enrichment facilitate fluid flow and could promote mineralisation when reactivated. Porosity collapse breccias and normal faulting during enrichment further control iron ore characteristics during the upgrading of BIF. Structures formed after BIF-upgrading can modify, preserve and expose ore bodies, as well as affect their mineralogy and texture.

Hypogene and supergene alteration

Hypogene and supergene alteration causes the following stages during BIF enrichment (Hagemann *et al*., 2016):

- Dissolution of silica and formation of carbonates and magnetite
- The transformation of magnetite to hematite (or martite) and additional leaching of silica
- Chert bands that are high in aluminium can be replaced by clays upon leaching to form shale-like bands (Clout, 2006)
- Additional conversion of magnetite to hematite, and replacement of iron silicates by hematite. Microplaty and specular hematite form and carbonates are leached away from the depositional site.
- Metamorphism of iron ore to result in granoblastic textures with magnetite and hematite porphyroblasts or schistosity and shear zones, depending on the type of metamorphism.
- Lastly, magnetite and remnant carbonate are transformed to hydrous goethite, and fibrous quartz and clay minerals may develop.

The two major BIF deposit types, Algoma and Lake Superior, derive their fluids from different sources, reflective of their tectonic settings. Basinal brines are prevalent in Lake Superior-type BIF systems, whereas magmatic fluids dominate the Algoma-type systems studied to date (Hagemann *et al.*, 2016).

Hydrothermal fluids of high-grade BIF

Hagemann *et al.* (2016) explains that few mass balance tests have been conducted on BIF-hosted iron ore systems, but that they all indicate varying enrichment of Fe with a substantial decrease in SiO_2. This is accompanied by a 25% decrease in volume within the high-grade iron ore area.

Mass balance analyses also show enrichment of LOI, F, MgO, Ni, Fe_2O_3, C, Zn, Cr and P_2O_5, and reduction of CaO, S, K_2O, Rb, Ba, Sr and Na_2O in mafic alteration zones adjacent the BIF deposit (Hagemann *et al.,* 2016).

5.2 Fluid Sources for BIF Enrichment

Hagemann *et al.* (2016) proposes four end members for hypogene and supergene enrichment, which summarise the possible fluid sources that could contribute towards a high-grade iron ore deposit. Hypogene enrichment characterises the first three models, while supergene is dominant in the fourth. The Carajás-type deposit exemplifies the first end member. This consists of a strike-slip fault zone setting with a granite-greenstone belt where early magmatic fluids and meteoric water provide the main source of fluid for enrichment.

Secondly, a sedimentary basin setting containing normal faulting, basinal brines and meteoric water constitutes the Hamersley-type end member. The third end member also involves a sedimentary basin but is defined by graben structures and glacial activity typical of Urucum-type deposits. Lastly, the Capanema-type end member contains BIF enriched by supergene processes, goethite ore, and limited evidence for hypogene alteration. The Sishen deposit is a variation of this end member where BIF and high-grade iron ore was preserved from weathering in karstic features within underlying carbonates.

6 Kolomela Mine

The physical and metallurgical properties of the Kapstevel South (KSS) deposit, Kolomela Mine, will affect the mining and marketing of the deposit. This chapter provides a brief introduction to the geology of the area as well as Kolomela Mine and its operations.

6.1 Geological Background

6.1.1 Regional ore formation

The supergene, Sishen-type deposits found in the Northern Cape are focused around the Maremane Dome feature extending from Sishen Mine in the north to Kolomela Mine in the south. These ore types are found where the Gamagara unconformity transects Transvaal Supergroup BIF of the Griqualand West basin (Beukes *et al.*, 2003). The Gamagara unconformity formed around 2.8-2.2 Ga, after the folding and upliftment of Transvaal Supergroup strata, and thus transects several different lithologies (Beukes *et al.*, 2003). Figure 6.1 shows the typical stratigraphy of a Sishen-type supergene iron ore deposit. Iron ore grade generally decreases with depth and transitions to unmineralized BIF. Ferruginous detrital ore is often found atop the unconformity due to the weathering of underlying ore (Beukes *et al.*, 2003).

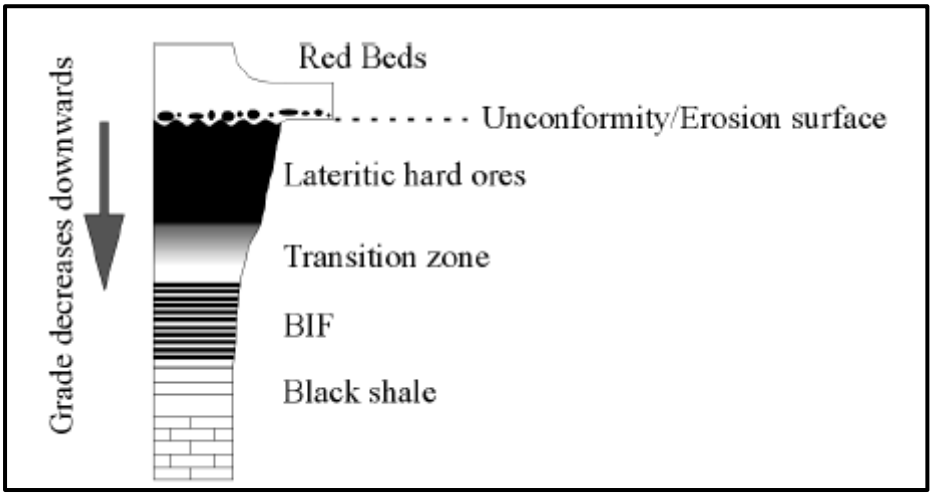

Figure 6.1 Illustration of the typical stratigraphy in Sishen-type supergene iron ore deposits (Beukes *et al.,* 2003)

Several small to large iron ore deposits are found along the extents of the Maremane Dome. Large iron ore deposits are found where Asbesheuwels BIF collapsed into karstic

features of the underlying Campbellrand Subgroup dolomites, protecting the iron ore from erosion (Beukes *et al*., 2003). Additionally, graben and synclinal features have also been known to preserve Sishen-type iron ore from regional erosion.

The formation of ore, and deposition of Gamagara red beds, occurred in a near equatorial environment, as evidenced by Paleomagnetic data (Evans, Beukes and Kirschvink, 2002). This further confirms the supergene enrichment of Sishen-Beeshoek iron ore deposits in a lateritic environment.

In addition to the supergene enrichment observed in the Northern Cape deposits, later-stage hydrothermal alteration is evidenced by specularite veins that infiltrate supergene hematite ore, conglomeratic ore as well as younger Gamagara shale and quartzite (Beukes *et al.*, 2003).

6.1.2 Regional geology

The Maremane Dome consists of Transvaal and Olifantshoek Supergroup lithologies that outcrop along a belt for about 60 km, as illustrated in Figure 6.2. It is located towards the western edge of the Kaapvaal craton and has experienced several deformation events, causing interference folding and faulting of the area.

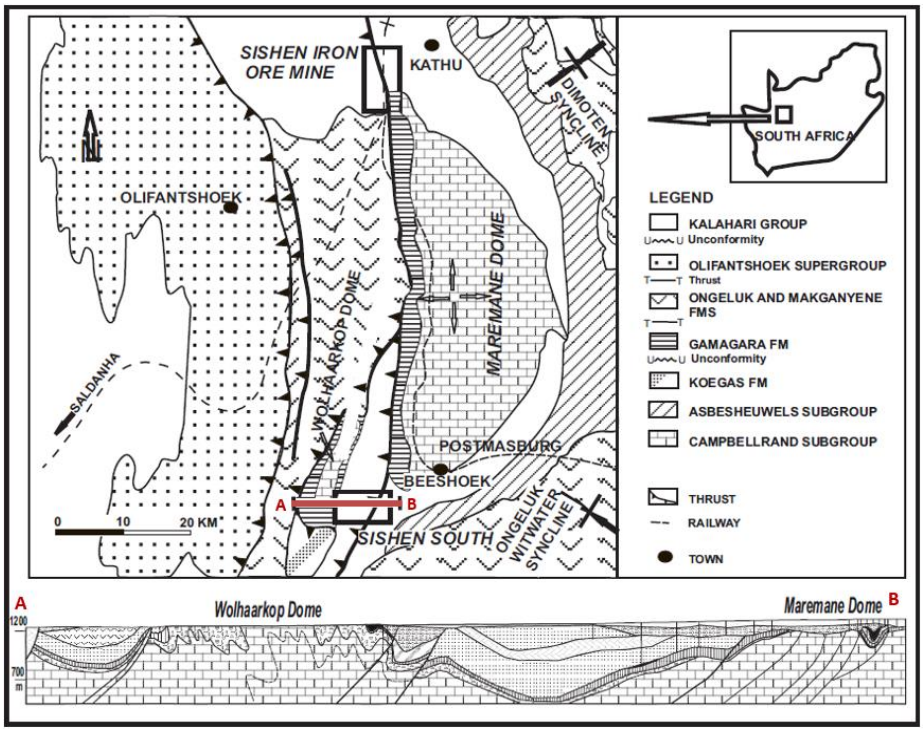

Figure 6.2 Regional geology of the Maremane Dome and surrounding iron ore deposits, after (Alchin and Botha, 2006)

The area stratigraphy includes the Campbellrand Subgroup dolomite (part of the Griqualand West Basin of the Transvaal Supergroup). This dolomite was deposited during the formation of the Ventersdorp Rift Basin around 2.78-2.64 Ga (Basson, *et al.*, 2018) and is dated around 2.6-2.46 Ga (Moore, Tsikos and Polteau, 2001). Deposition of Wolhaarkop chert breccia and Ghaap Group BIF occurred after the Campbell Rand dolomites formed, with chert breccia being the result of solution-collapse within karsts (Van Wyk, 1980). The Kolomela BIF forms part of the Kuruman Iron Formation, Asbesheuwels Subgroup (Smith and Beukes, 2016). It has been correlated with the Penge Iron Formation in the Transvaal Basin, and is approximately 2.5 Ga (Trendall, De Laeter and Nelson, 1995).

Uplift and erosion of the area during the Kalahari Orogeny around 2.22-2.1 Ga (Alchin, Lickfold, Mienie, Nel and Strydom, 2008) resulted in east-verging, north-south trending folds, and the creation of the Postmasburg Unconformity, which played a pivotal role in the supergene iron-enrichment of the upper portion of Kuruman Iron Formation BIF (Smith & Beukes, 2016). Clastic sediments of the Gamagara Formation, of the Olifantshoek Supergroup, were deposited above the unconformity (Alchin, *et al.,* 2008). These clastic sediments include sequences of shale, quartzite and conglomerate. Hematite-rich conglomerate is found at the base of the Olifantshoek Supergroup sediments.

The Kheis-Korannaberg Orogeny is the second major orogeny to affect the area and took place around 1.83-1.73 Ga. This again resulted in eastward-directed thrusting and folding (Altermann and Hälbich, 1991; Beukes and Smit, 1987). The Blackridge Thrust (Beukes and Smit, 1987) is responsible for juxtaposing older Ongeluk lavas and Makganyene diamictite (de Villiers and Visser, 1977) atop younger Olifantshoek Supergroup sediments.

The Lomanian Orogeny resulted in the North North-West (NNW) directed deformation along the southern extents of the Kaapvaal Craton around 1.35-1.0 Ga (Altermann, 1997; Altermann and Hälbich, 1991). The event is thought to be responsible for the slight Northward dip (~3^{o}) of the Maremane Dome (Basson *et al.,* 2018).

As noted by (Visser, 1971) a large proportion of the stratigraphy was removed via Dwyka glaciation, and redeposited as tillite. Lastly, tertiary regional erosion resulted in the deposition of the Kalahari Group, consisting of calcrete, dolocrete, clay and pebble layers (Alchin *et al.,* 2008).

Gabbroic sills intrude the area and are often found between iron ore and BIF in the Kolomela pit areas.

6.1.3 Local geology

Kolomela Mine, previously known as Sishen South, is located at the southern extent of the Maremane Dome, in the Northern Cape. The farms being explored and mined on the property include Kapstevel North, KSS, Ploegfontein, Leeuwfontein and Klipbankfontein (Figure 6.3). Currently Kapstevel North, Leeuwfontein and Klipbankfontein are active pits, while KSS is planned for future mining.

Ore types

The ore types found at Kolomela can be grouped into four main types: laminated, massive, collapse-breccia, and conglomeratic hematite. The aforementioned ore types are primarily a result of supergene enrichment of BIF (Smith and Beukes, 2016), and possible later hydrothermal alteration (Friese and Alchin, 2007).

Laminated ore is made up of alternating bands of higher- and lower-lustre hematite, while massive ore lacks this alternating banding and appears more uniform. Smith and Beukes, (2016) suggest that laminated ore is derived from microbanded BIF (ferhythmite) and massive ore originates from muddy, lutitic BIF. The ferhythmite microbands of laminated ore are thought to be a result of geochemical varves produced by photosynthesising organisms (Beukes, 1983).

Conglomeratic ore is comprised of subrounded to angular, poorly-sorted hematite clasts in a ferruginised shale or hematite matrix, with some specularite (Alchin *et al.,* 2008). Lastly, collapse-breccia ore is proposed to have resulted from the collapse of hematite ore into dolomitic karsts (Smith and Beukes, 2016).

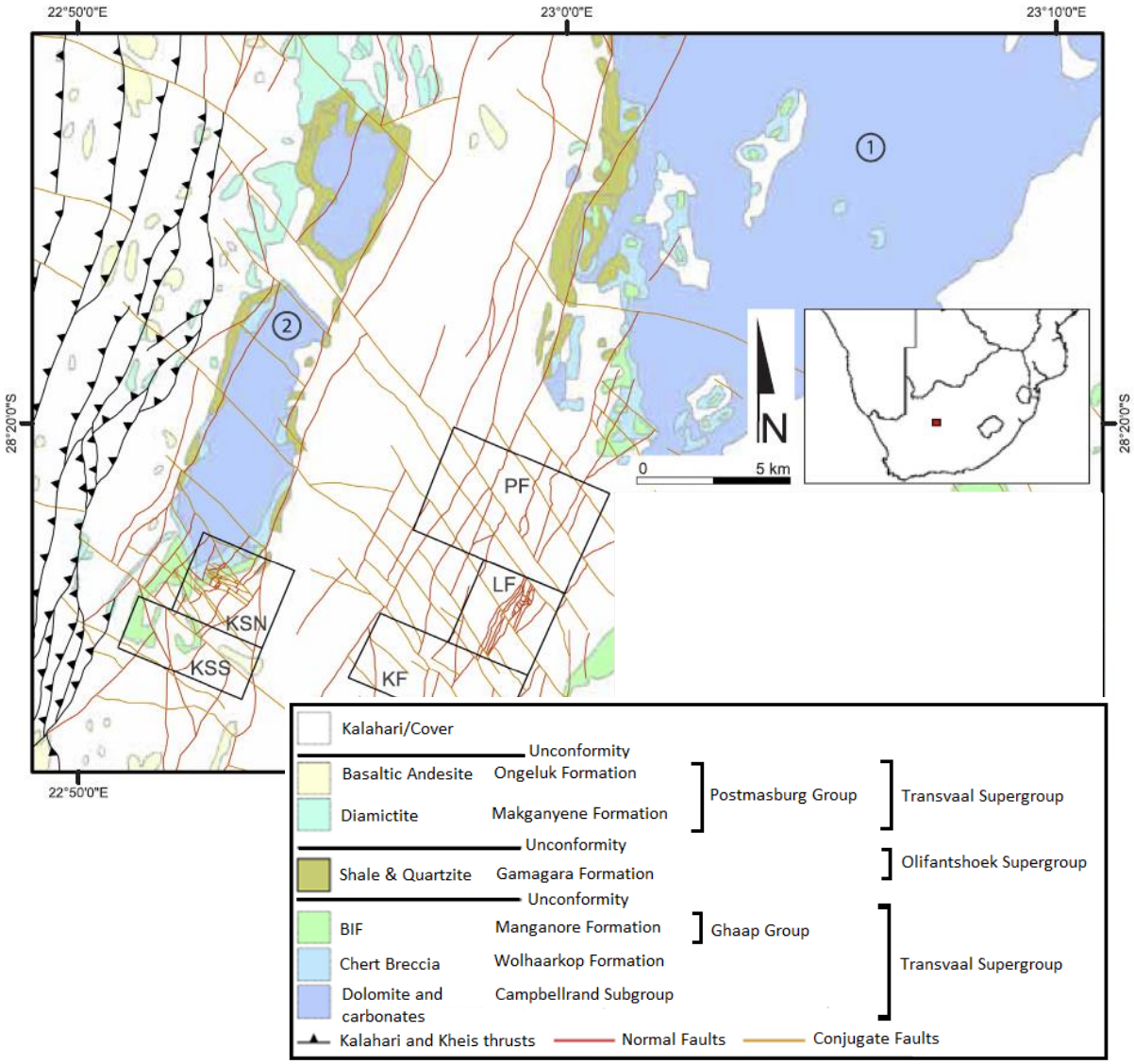

Figure 6.3 Geology of the Kolomela-Maremane Dome area, after (Basson *et al.,* 2018). KF: Klipbankfontein, LF: Leeuwfontein, PF: Ploegfontein, KSN: Kapstevel North, KSS: Kapstevel South

The most common ore textures observed at Kolomela Mine are laminated and massive. As of 2018, Kolomela ore comprised approximately 53.1% laminated, 28.9% massive, 6.5% brecciated and 11.4% conglomeratic ore (Basson *et al.,* 2018).

Local geology of the Kapstevel South deposit

The KSS ore body is situated towards the southern extent of the Wolhaarkop Dome, a smaller structure to the west of the Maremane Dome (Basson *et al.,* 2018). To date, four faults have been identified in KSS – two sub-vertical northeast-trending normal faults that delineate a down-faulted block, and two sub-vertical northwest-trending strike-slip faults

(Figure 6.4). These are delineated from exploration drill holes as well as regional geophysical data.

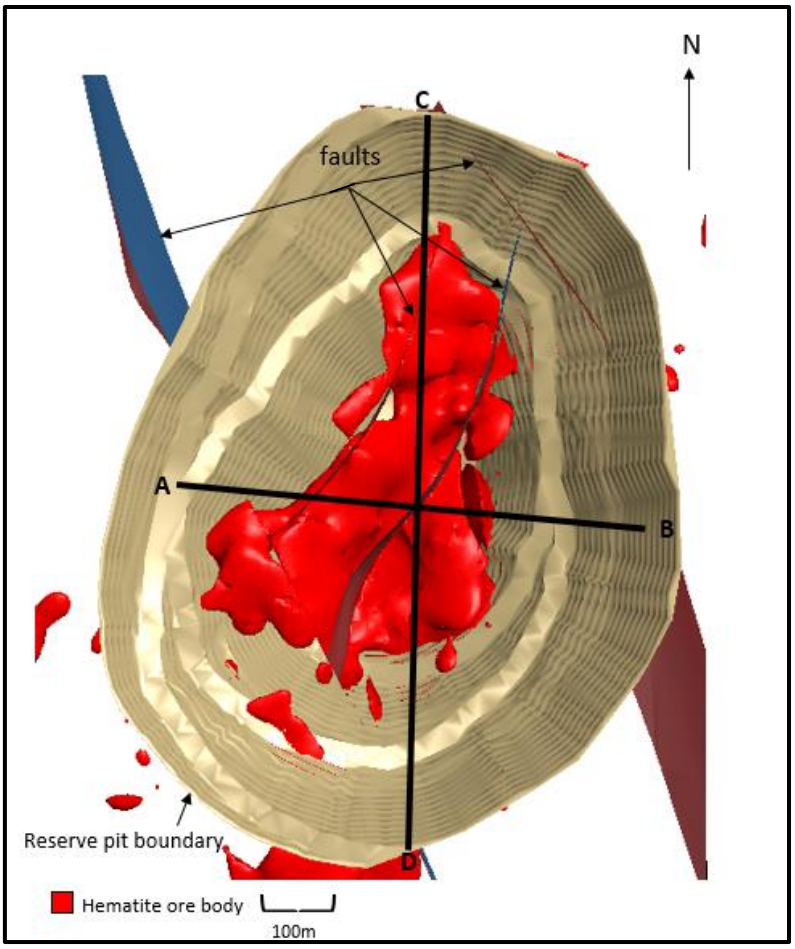

Figure 6.4 Illustration of the KSS ore body, planned pit boundary and delineated faults

The stratigraphy at KSS follows that observed on the rest of the mine, with one of the more significant differences being the thicker intersections of tillite, caused by Dwyka glaciation (Visser, 1971).

Whilst a gabbroic sill generally underlies the ore body in the LF and KF pits, it is found transecting the KSS ore body. Figure 6.5, created by the author using *Leapfrog Geo* version 5.1 software, shows cross sections containing such examples, with the trace lines of the sections displayed in Figure 6.4. According to Basson *et al*. (2018), the gabbroic sills have likely been emplaced by low-angle thrusts, as indicated by their dips and geometries.

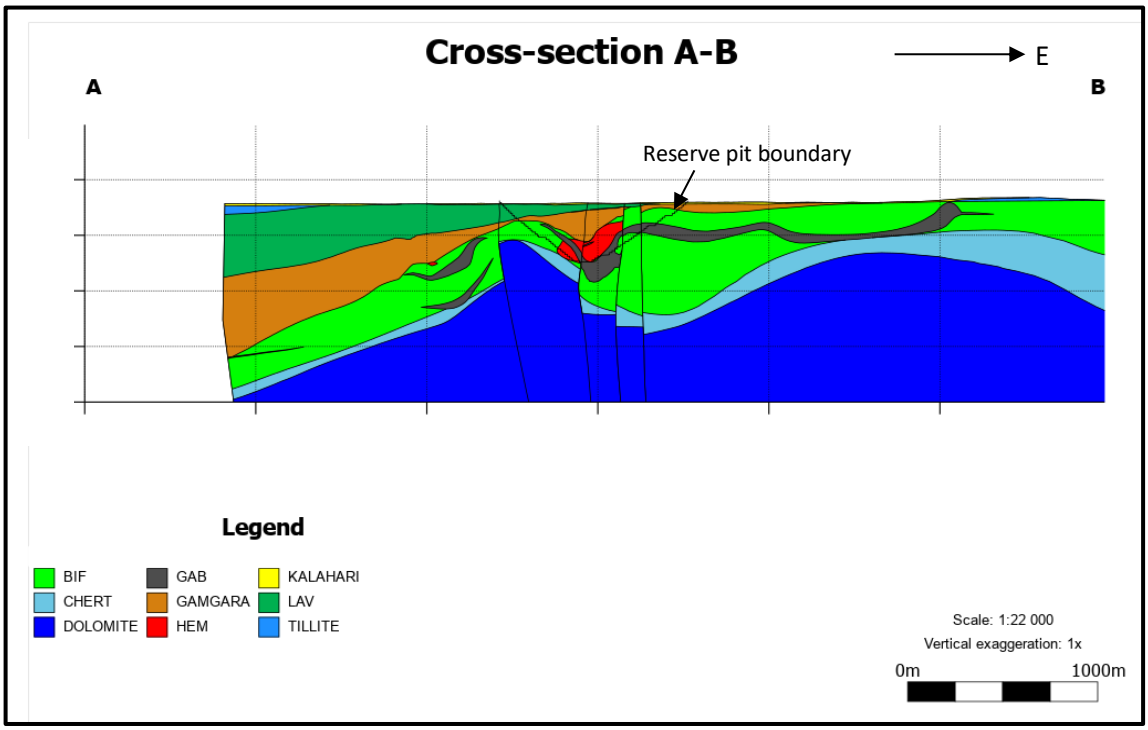

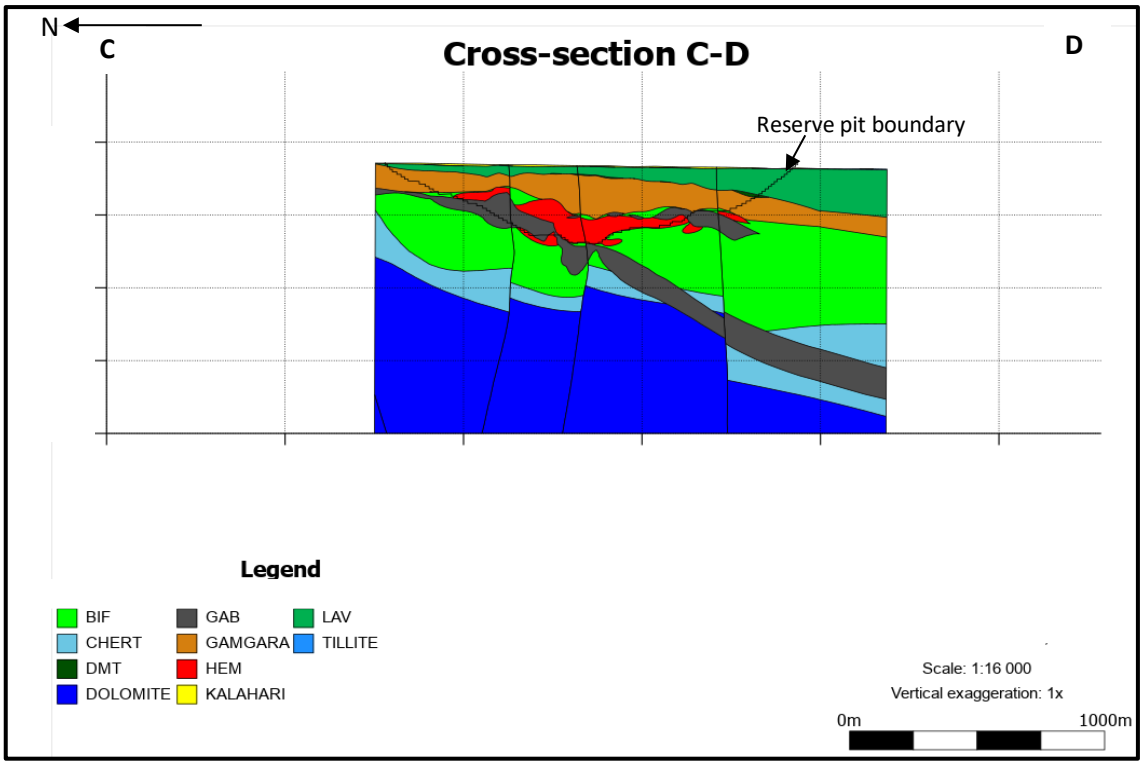

Figure 6.5 Cross sections of KSS. DMT: diamictite, GAB: gabbro, HEM: hematite, LAV: lava

Stratigraphy of the Kapstevel South deposit

The Campbell Rand Subgroup hosts the dolomites of KSS and forms the deepest lithology intersected by drill holes at KSS. Chert breccia of the Wolhaarkop Formation overlie the Campbell Rand dolomite. This lithology occurs in intersections of between 8 and 170 m thick, although few exploration drill holes reach this depth.

BIF of the Kuruman Formation, Asbestos Hill Subgroup, overlies the chert breccia, and reaches thicknesses of 500 m and greater. The costs and time associated with drilling these packages is one of the main factors inhibiting exploration drill holes from intersecting chert breccia and dolomite.

Laminated iron ore, enriched from Kuruman Formation BIF, occurs towards the top of the BIF package. Massive iron ore, occurring above the laminated, is derived from the chemically-similar Daniëlskuil Formation iron ore (Basson *et al.*, 2018; Klein and Beukes, 1989). Conglomeratic iron ore, generally above the massive-textured ore, provides evidence of sedimentary reworking of the iron ore deposit. This ore type is commonly found in synclinal and half-graben features of KSS.

Gritty, low to medium-grade conglomerate overlies the Gamagara unconformity, and at times conglomeratic iron ore, but is relatively thin (<0.5 m) with scattered occurrences. The remainder of the younger Gamagara Formation comprises thick shale units (30-175 m thick) that are periodically intercalated with quartzite lenses. Shale packages thicken in downthrown fault blocks, and gradually increase in thickness towards the west and (to a lesser-extent) south of the deposit. The shale units comprise tech shale, consisting of alternating layers of aluminous light green and brown shale, as well as thick intersections of brown, grey and at times dark grey, carbonaceous shale. Thick shale intersections within downthrown fault blocks often contain pebble-sized hematite clasts for up to 10 m above the bottom contact, indicating a higher-energy environment with syndepositional erosion of hematite.

Ongeluk lavas occur above the Gamagara package, with an increasing degree of calcretisation towards the surface, where the lithology has been exposed. Dwyka tillite overlies the Ongeluk lavas, which is in turn overlain by calcrete of the Kalahari Group.

Two gabbroic sills transect the KSS deposit, one towards the bottom of the BIF package and another towards the top contact. The upper gabbro sill intrudes laminated hematite in several places, although majority of the KSS ore is found above the gabbro sill.

6.2 Extraction, Processing and Marketing of Iron Ore

Kolomela Mine is an open-pit operation that primarily produces DSO. This entails the drilling, blasting, loading and hauling of hematite iron ore which is crushed, screened and then dispatched. Ore produced by Kolomela Mine is blended with that from Sishen Mine at the Saldanha export harbour and marketed as three Kumba products; including premium lump (65.5 %Fe), premium 20mm lump (65.2 %Fe) and standard fines (63.5 %Fe) (Kumba Iron Ore Limited, 2019a). In the 2018 financial year, the company produced 43.1 Mt of iron ore while the three biggest iron ore producers (BHP Billiton, Rio Tinto and Vale) collectively produced 904.4 Mt (BHP, 2018; Kumba Iron Ore Limited, 2019 b, Rio Tinto, 2019; Vale, 2019). The relatively small-scale mining from KIO highlights the importance of producing exceptional-quality ore, allowing the company to compete with global mass producers.

In order to achieve the product specifications required from Kolomela Mine, finger stockpiles of specific grade ranges are blended into the primary crusher together with direct-feed material from the pits. This blending practice is crucial at the DSO plant, as there is little downstream beneficiation to correct grade deviations.

Currently, grade control practices at the DSO plant focus on the chemistry of iron ore, and an average ratio is applied to determine the amount of lump and fine material that can be expected after crushing and screening. The average lump-fine ratio expected at Kolomela Mine is 60:40 (Kumba Iron Ore Limited, 2019 a), with the potential to increase this ratio through better understanding of the geometallurgical properties of the ore body. Improved geometallurgical understanding will also aid in determining the expected lump-fine ratio per rock type and geographic location, which are affected by variables such as hardness, AI and TI. Lump material with high AI or low TI values can be flagged with a risk of degrading to fine material during transport. Knowledge of this risk will allow the company to market the material appropriately and manage client expectations.

Kumba Iron Ore markets their product with average values for AI, TI, RDI, RI and DI. This approach is problematic when an area exhibiting abnormal metallurgical or physical

properties is mined. Thus, delineating areas with different AI, TI, RDI, RI and DI values will allow for proactive material blending to meet customer requirements. This research project will add value by identifying the relationships between metallurgical or physical properties and commonly logged geological properties, after which the different geometallurgical domains can be defined and included into the grade control model and grade control blending practices.

7 Research Methodology

The correlations between geological, physical and metallurgical characteristics of the KSS deposit were derived via the geometallurgical logging of core, sampling and subsequent data analysis. This chapter outlines how these steps were conducted.

7.1 Drilling and Logging of Geometallurgical Core

The study area focused on the KSS farm of Kolomela Mine, where mining is planned to commence in the year 2020. Exploration core drilling is prevalent in the area and has delineated the ore body as well as waste rock types, allowing for a geological model of the deposit to be built.

Throughout the study, drill holes were planned and interrogated using *Leapfrog* software. In order to identify the locations for geometallurgical drill holes, three sections were drawn approximately across strike of the KSS deposit (Figure 7.1). Exploration drill holes were identified along these sections, within the optimised pit shell, and twin drill holes planned approximately 5 m to the west or east of each exploration drill hole. Planning geometallurgical holes as twin drill holes to existing exploration drill holes allows the targeting of certain rock types and ore intersections. The drill holes were thus planned to intersect all ore types in the deposit, with good spatial representation across the three sections, amounting to a total of 15 planned drill holes.

Each drill hole was piloted via percussion drilling to approximately 10 m above mineralisation (~40% Fe) and then further drilled using PQ-sized diamond core drilling in order to attain core samples 85 mm in diameter. This is larger than the typical NQ-sized (47.6 mm) exploration drill holes, allowing for larger samples to be collected in order to meet the mass requirements for geometallurgical testing. Each geometallurgical drill hole was terminated approximately 10 m below mineralisation, except where drill hole instability prevented further drilling.

The core boxes were then transported to the core yard laydown area for geometallurgical logging. Geometallurgical logging entails the meticulous recording of rock details, paying attention to any changes that may occur in the rock, such as:

- Lithological changes

- weathering intensity
- degree of mineralisation and alteration
- joint and fracture intensity
- vein type and intensity
- Intensity of vugs or cavities
- Textural changes
- Colour changes

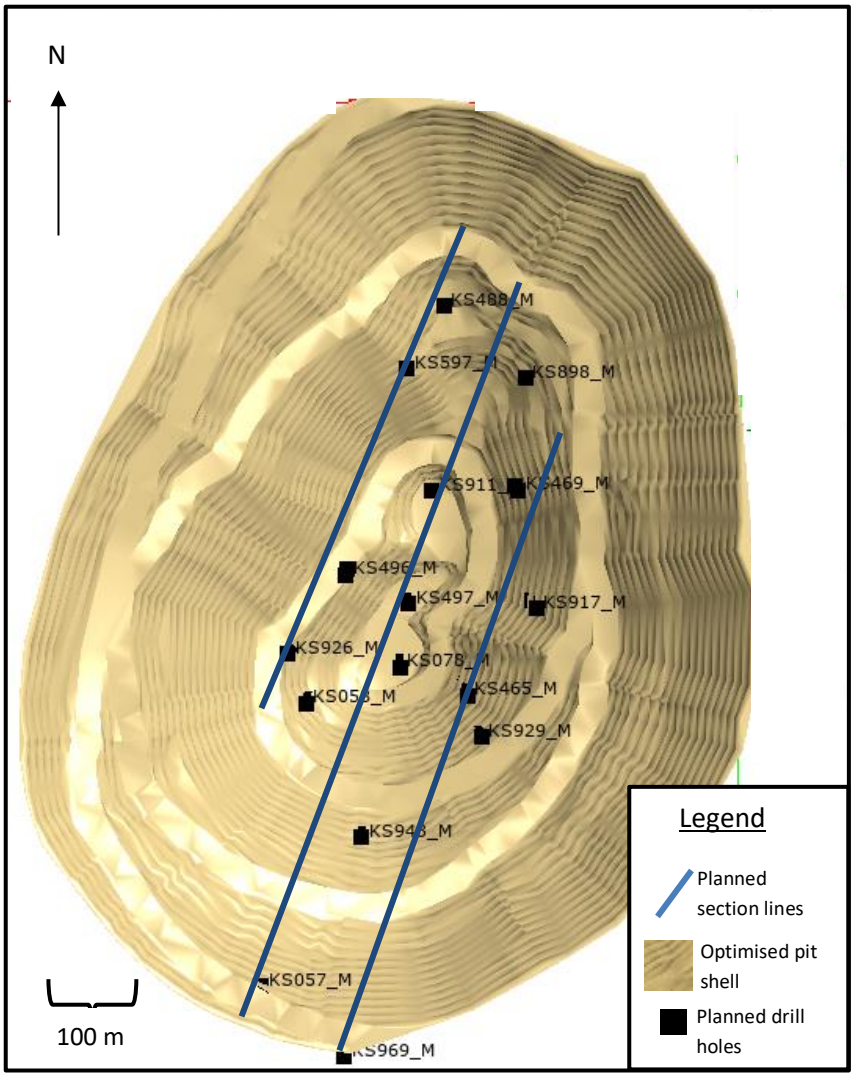

Figure 7.1 Geometallurgical drill holes are planned along three cross sections of the Kapstevel South deposit

On completion of drilling, each drill hole was surveyed by a contractor, using Gyro based equipment that consists of a non-magnetic electronic multi-shot tool. The hole

coordinates were measured using a dual frequency Trimble R10 global positioning system (GPS). This was done in order to plot the exact drill hole path and potential deflections.

Rock contacts were marked wherever one or more changes in the above characteristics occurred, limited to a minimum interval length of 50 cm. This meticulous logging allows for the identification of samples that are completely homogeneous. Geometallurgical comparisons can then be made between samples of varying properties, and the influence of each property can be assessed.

Geotechnical logging was subsequently performed on all drill holes, recording information such as faulting, slickenlines, joint intensity and spacing, joint roughness, joint form, and geological strength index (GSI). Samples were marked out in approximately one-meter intervals in order to be sent for chemical assay. Of these assay samples, the following samples were also marked:

- Archimedes density tests
- Crusher work index (CWi) tests
- Uniaxial compressive strength (UCS) tests
- Sag mill comminution (SMC) tests

Of the above-mentioned samples, CWi, UCS and SMC tests are batched separately as "hardness" batches. Each sample is required to meet competency and length specifications required for testing. Throughout geometallurgical logging, the internal Kumba Iron Ore *Geometallurgical Drilling Guideline and associated QC Protocol for Sampling, Sub-sampling and Testwork* (Govender, Denivelle and Britz, 2018) was followed, adhering to strict Quality Assurance/Quality Control (QA/QC) standards throughout data collection. This includes creating 20 samples per batch, adding a certified reference material (CRM) to each batch, as well as pulp and crush duplicates. Photographs are taken of each core box before physical sampling commences. This step as crucial as the entire core is sent for testing, leaving no core samples for future reference.

A total of 17 holes were drilled on the Kapstevel South deposit, including two re-drilled holes. The two re-drilled holes (KS497_Q and KS929_N) were drilled as PQ-sized core from surface due to stability problems in piloted holes. Table 7.1 lists all holes drilled on the farm, along with their end depths. Due to the large volume of core to be logged,

contractor employees aided in the logging of the holes, with the logging of each hole reviewed by the researcher.

Table 7.1 Geometallurgical holes drilled on the KSS farm

Hole ID	Piloted Depth (m)	Final Depth (m)	Total PQ-sized core meters
KS497_M	196.23	229.13	32.9
KS969_M	140.41	242.23	101.82
KS943_M	105.2	296.3	191.1
KS911_M	150.03	355.88	205.85
KS488_M	105.43	188.23	82.8
KS078_M	195.23	335.13	139.9
KS597_M	99.85	191.33	91.48
KS057_M	105.02	196.09	91.07
KS058_M	100.35	245.18	144.83
KS496_M	85.17	212.23	127.06
KS926_M	69.85	272	202.15
KS898_M	131	254.23	123.23
KS929_M	139.31	204.76	65.45
KS469_M	140.53	173.13	32.6
KS465_M	149.93	284.3	134.37
KS497_Q	0	320.3	320.3
KS929_N	0	278.29	278.29
Total			2365.2

7.2 Chemical Assaying and Hardness Testing of Samples

Figure 7.2 shows a schematic flow of the sample path after logging, with samples initially batched as either a hardness or normal batches. The hardness samples are sent to *RockLabs* in Pretoria and are retrieved after testing. Retrieval of the sample is done in order to perform chemical analysis at the *Anglo Technical Services* lab in Johannesburg. The hardness samples follow the same sampling route as the normal batches once testing is complete, after which assay results undergo a QA/QC process before being accepted into the *acQuire* database. This includes checking that the sample falls within the specified ranges of the CRM, and that the pulp and crush duplicates fall within specified ranges of each other. If a batch meets these requirements, the chemical assays are accepted. Each

sample is also checked for mass conservation during sample preparation. This is important as the remaining sample mass will be used for compositing and must be representative of the original sample. Mass loss from drying to crushing and splitting must fall within specified ranges, otherwise the individual sample is rejected and not used for compositing.

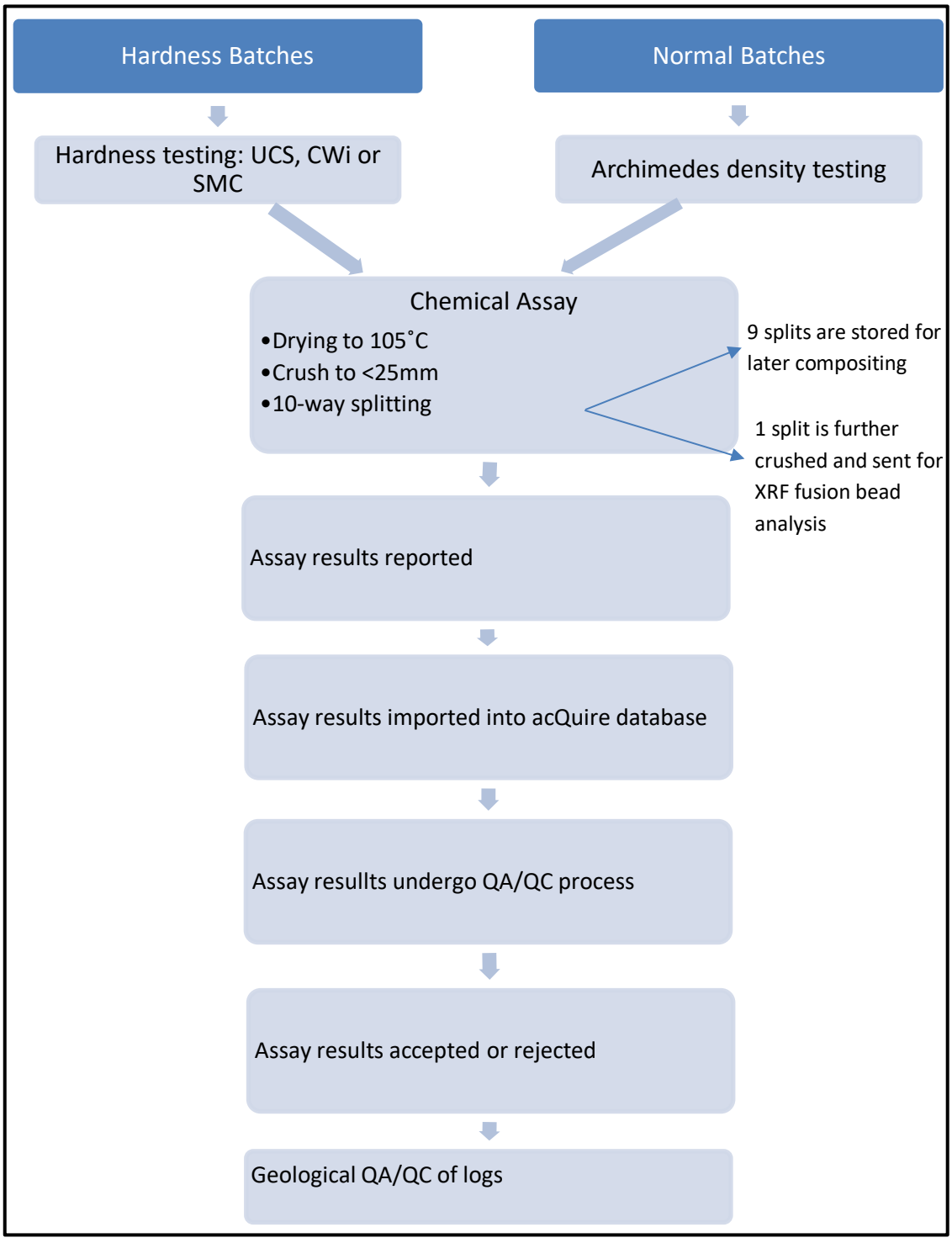

Figure 7.2 Sample path of hardness and normal batches

Once chemical assays are accepted, they are used to check the quality of geological logs. This includes changing intervals logged as hematite, but containing <60 %Fe, to another rock type based on chemistry and photographs of the core. Common examples include ferruginised shale, ferruginised conglomerate and BIF. Where samples are logged as a rock type other than hematite, but contain >60 %Fe, the interval is changed to hematite.

7.3 Metallurgical and Physical Test Work

Once the chemical assays are received, the remaining proportions of each sample not used during assay are composited. Samples are only composited where they occur consecutively in the same drill hole. An example illustrating the way that samples are composited is shown in Figure 7.3.

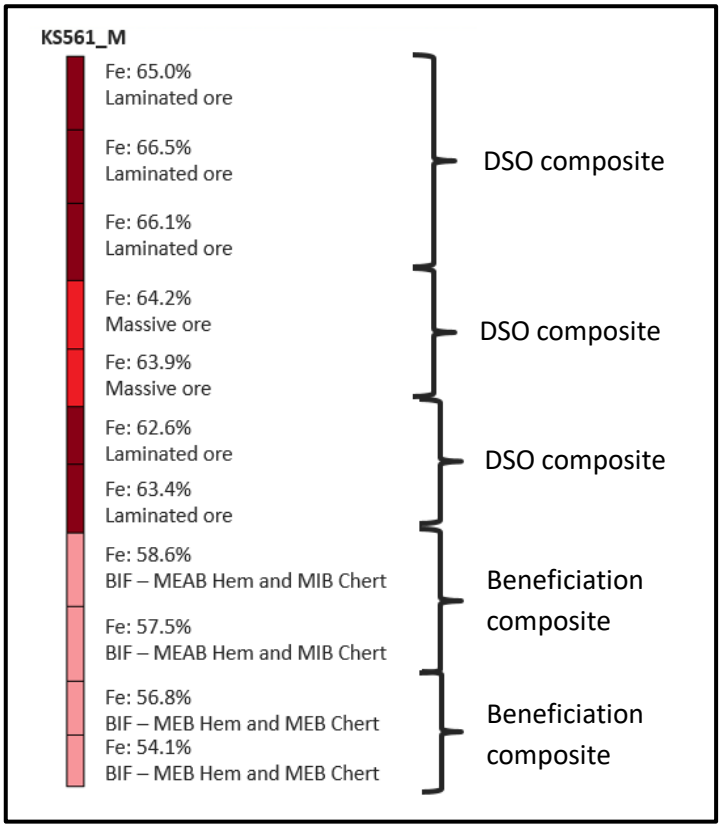

Figure 7.3 Example of the compositing of chemistry samples to create larger samples for physical and metallurgical testing. MEAB: meso- to macrobanded, MIB: microbanded, MEB: mesobanded

As stated by Keeney and Walters (2011), the compositing of samples presents a risk of blending out the variability of samples. To mitigate this, samples of the same lithology, material class and texture are composited to meet lab sample mass requirements. The material classes represent Kolomela Mine's ore classifications, which delineates ore to be

stockpiled separately. These stockpiles, as well as direct feed from the pit, are used to blend DSO to the right product specification.

In cases where there were insufficient consecutive samples of the same lithology, material class and texture to meet mass requirements, samples were composited according to what will likely be mined together. DSO composites are screened and the -25 +8 mm size fraction undergoes AI, TI, RDI, RI and DI testing at Anglo American's Value in Use Lab in Johannesburg. The -8 +1 mm and -1 mm size fractions, as well as the -25 +8 mm fraction once testing is complete, are sent for chemical analysis.

The DSO composite results are reported and imported into the *acQuire* database for QA/QC. This entails checking the mass and chemical conservation during physical compositing, crushing and screening, which are all required to fall within specified ranges. Failure to meet these ranges results in rejection of the composite.

7.4 Analysis of Physical and Metallurgical Results

The physical and metallurgical test results for all composites are attached in Appendix A: Chemistry, geology and physical/metallurgical properties of composites. The absence of results indicates insufficient sample in the -25 +8 mm size fraction to complete test work.

Four assumptions were withheld during collection and interpretation of physical and metallurgical results (Dohm, 2019):

- Assumption I: physical and metallurgical and chemistry results are precise. Unfortunately, the mass requirement for sampling does not allow for the inclusion of duplicate samples to test precision. Thus, precision is checked by comparing physical and metallurgical samples that are geologically similar.
- Assumption II: physical, metallurgical and chemistry results are accurate. Mass and chemical conservation checks are performed on all physical and metallurgical samples during sample preparation and compositing. Samples that fail these checks are rejected. Physical and metallurgical results are checked through logical QA/QC, and are obtained using ISO-accredited techniques (International Organisation for Standardisation 3271, 2015; International Organisation for Standardisation 4696-1, 2015; International Organisation for Standardisation 7215, 2015; International Organisation for Standardisation 8371, 2015).

- Assumption III: the samples analysed are a representative subset of the population. Thus, the samples acquired do not alter the behaviour of the remaining ore in Kapstevel South and are considered to represent the remaining ore.
- Assumption IV: the samples used in this study were obtained randomly and independently. Samples were attained across the ore deposit, without targeting certain areas or filtering for biased data.

7.4.1 Exploratory data analysis

The locations of samples used during the study are displayed in Appendix B: Locations of samples containing test results for (a) AI, (b) TI, (c) RI, (d) RDI, (e) DI. The samples show good vertical representation, and reasonable horizontal representation. However, it would be preferable to obtain more samples from different drill holes.

Physical and metallurgical properties of Kapstevel South versus Kolomela Mine

The mean, standard deviation and coefficient of variation was calculated for resultant datasets. The standard deviation provides a way to measure the variability of the data (Altman and Bland, 2005) as 95% of the data should fall within two standard deviations of the mean. It is beneficial to use the coefficient of variation (CoV) for comparison purposes as it is independent of the units of measurement for each variable (Herve, 2010). Dividing the standard deviation by the mean will yield the CoV. A small CoV approaching zero indicates that the standard deviation is small, with majority of the data falling within a narrow range around the mean, and thus little variation in the data.

The average, standard deviation (std. dev.) and CoV for each physical and metallurgical property on Kapstevel South is displayed in Table 7.2. This is compared to the physical and metallurgical properties of samples from the three active (currently mined) pits at Kolomela Mine: Leeuwfontein, Klipbankfontein and Kapstevel North. Each of these values is calculated from sample data submitted to the lab. As samples are submitted proportionally to the amount of each ore texture mined, and are derived from a wide spatial area, these values are considered a reasonable approximation of what can be expected from the ore deposits. Geometallurgical wireframes will need to be constructed

and included in the geological block model in order to calculate a more accurate mean, standard deviation and CoV of the metallurgical and physical properties.

Table 7.2 Average physical and metallurgical properties of Kapstevel South compared to the active pits at Kolomela Mine. n: number of samples analysed, std. dev: standard deviation, KOL: Kolomela Mine, CoV: coefficient of variation

	AI %		TI %		RI %		RDI %		DI %	
	KSS	KOL	KSS	KOL	KSS	KOL	KSS	KOL	KSS	KOL
Mean	10.78	11.11	84.81	82.44	26.32	31.42	3.99	10.82	0.16	0.11
Std. dev.	3.98	3.50	5.10	3.98	8.08	11.56	3.64	8.86	0.20	0.10
CoV	0.37	0.31	0.06	0.05	0.31	0.37	0.91	0.82	1.26	0.89
n	30	124	30	124	27	119	31	123	27	117
Preferred range for lump*	<10		>80-85		>60		<10		<15	

*(Barlow, 2020; Lu *et al.*, 2015).

The Kapstevel South farm shows slightly superior AI and TI results to that observed in the active Kolomela pits, while RI and RDI yield more significant differences. The RI for KSS is lower than usually experienced at Kolomela Mine, and further away from the preferred range from lump ore. This indicates the slower reduction of ore and a consequential increase in power consumption for the blast furnace. However, the RDI for KSS yields favourable values well within the preferred range and indicates that the ore is not as susceptible to fines generation during reduction.

The CoV of AI is 0.37, indicating relatively little variation in KSS data, however the mean is just over the preferred range for lump ore. It is important to be able to identify the rock types as that fall outside of the preferred range for lump ore to mitigate company risk.

The CoV of RI in KSS does not show significant variation and all samples fall well outside of the preferred range. RDI and DI show higher variation than the remaining physical and metallurgical variables of KSS. However, DI is well within the preferred range for lump ore and its variation does not pose a risk to the company.

In summary, while most physical and metallurgical variables on KSS do not show significant variation, there are samples that fall outside of the preferred ranges. Identifying the rock types that do not meet customer requirements will allow the Mine to slowly blend the unfavourable rock types into the high-quality feed, in order to achieve

specification. Alternatively, the company can market the less-preferable ore to clients that accept material with these properties in their blast furnaces.

Identification of outliers

Data outliers were identified using the method proposed by (Schwertman, Owens and Adnan, 2004) whereby the probability of finding an uncontaminated sample outside defined fences can be specified. This method also allows for the more accurate determination of outliers in normal to relatively asymmetric distributions of data. The equations for finding the upper and lower fence limit for outliers can be expressed using the equations:

$$q_2 - \frac{2(q_2 - q_1)}{k_n} Z_{\alpha/2} \quad \text{and} \quad q_2 + \frac{2(q_3 - q_2)}{k_n} Z_{\alpha/2}, \tag{7.1}$$

where q_2 is the median of the data, q_1 and q_3 represent the lower and upper quartiles respectively. The value for k_n is derived from Table 7.3, and Z_α represents the probability of an uncontaminated sample existing beyond the fence.

Table 7.3 Values for k_n used for each n value in eq. 7.1 (Schwertman *et al.*, 2004)

n	k_n	n	k_n	n	k_n	n	k_n	n	k_n	n	k_n
5	1.65798	22	1.33333	39	1.38071	56	1.34361	73	1.36635	90	1.34535
6	1.28351	23	1.4023	40	1.34165	57	1.3713	74	1.34454	91	1.36267
7	1.51475	24	1.33753	41	1.38021	58	1.34329	75	1.36557	92	1.34562
8	1.32505	25	1.40096	42	1.34104	59	1.37004	76	1.34495	93	1.36258
9	1.50427	26	1.33587	43	1.37779	60	1.34394	77	1.36543	94	1.3455
10	1.31212	27	1.39455	44	1.34226	61	1.36981	78	1.34478	95	1.3621
11	1.45768	28	1.33894	45	1.37737	62	1.34366	79	1.36474	96	1.34576
12	1.32968	29	1.39355	46	1.34175	63	1.36871	80	1.34514	97	1.36201
13	1.45268	30	1.3377	47	1.37536	64	1.34424	81	1.36461	98	1.34565
14	1.32353	31	1.38876	48	1.34278	65	1.36851	82	1.34499	99	1.36157
15	1.42975	32	1.34004	49	1.37501	66	1.34399	83	1.36398	100	1.34588
16	1.33318	33	1.38799	50	1.34235	67	1.36754	84	1.34532	200	1.34740
17	1.42684	34	1.33909	51	1.37331	68	1.3445	85	1.36387	300	1.34792
18	1.32959	35	1.38428	52	1.34322	69	1.36737	86	1.34517	400	1.34818
19	1.41322	36	1.34092	53	1.37301	70	1.34429	87	1.3633	∞	1.34898
20	1.33568	37	1.38367	54	1.34285	71	1.3665	88	1.34548		
21	1.41132	38	1.34017	55	1.37156	72	1.34474	89	1.36319		

The 0.025 and 0.975 fences represent a 5% chance of an uncontaminated sample lying outside of the specified range between F_1 and F_3, and a Z_α value of 1.96 is used to calculate these values. This Z value is derived using the normal distribution table attached in Appendix C: Percentage Points of the Normal Distribution (Lindley and Scott, 1995). Similarly, the 0.05 and 0.95 fences represent a 10% chance of an uncontaminated sample

lying outside of the specified range between f_1 and f_3 and a Z_α value of 1.645 is used to calculate these values.

The results of these calculations are displayed in Figure 7.4 where points falling between fences f1 and F1, or f3 and F3, are considered mild outliers. Points falling beyond fences F1 and F3 are considered significant outliers. All significant outliers were investigated for geological reasoning behind their anomalous characteristics and used to aid the grouping of data.

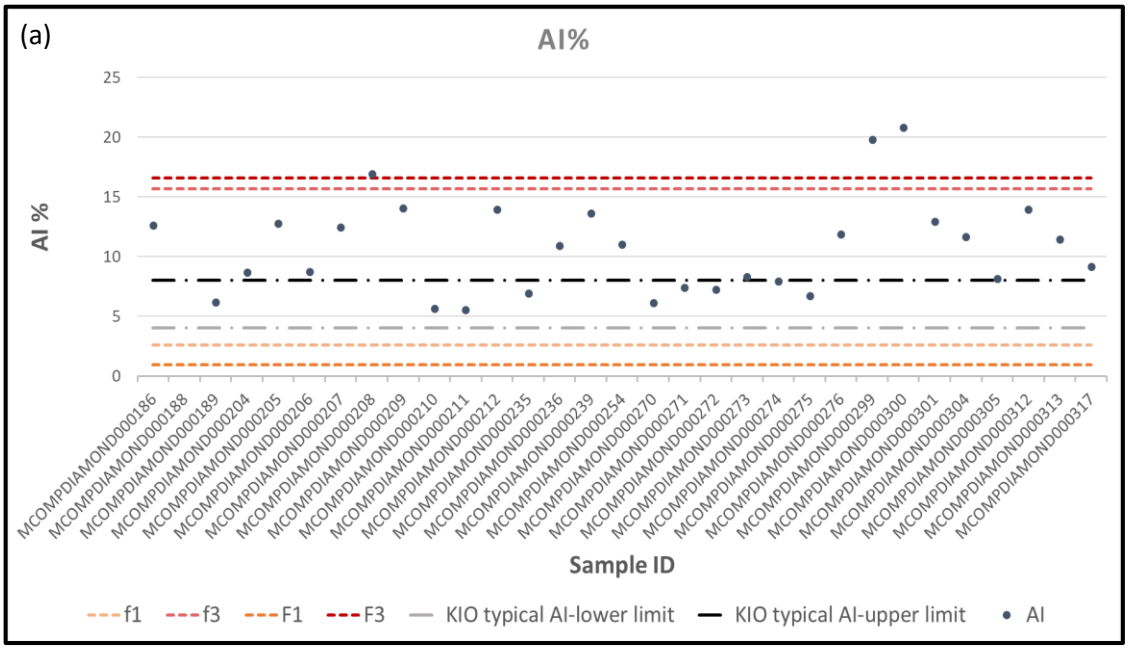

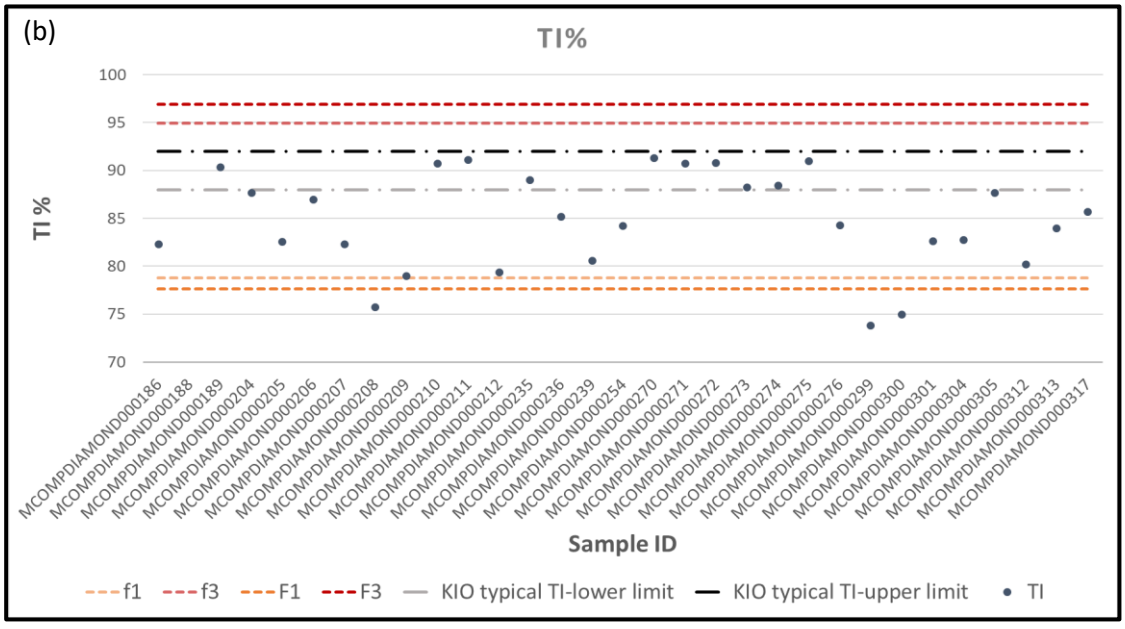

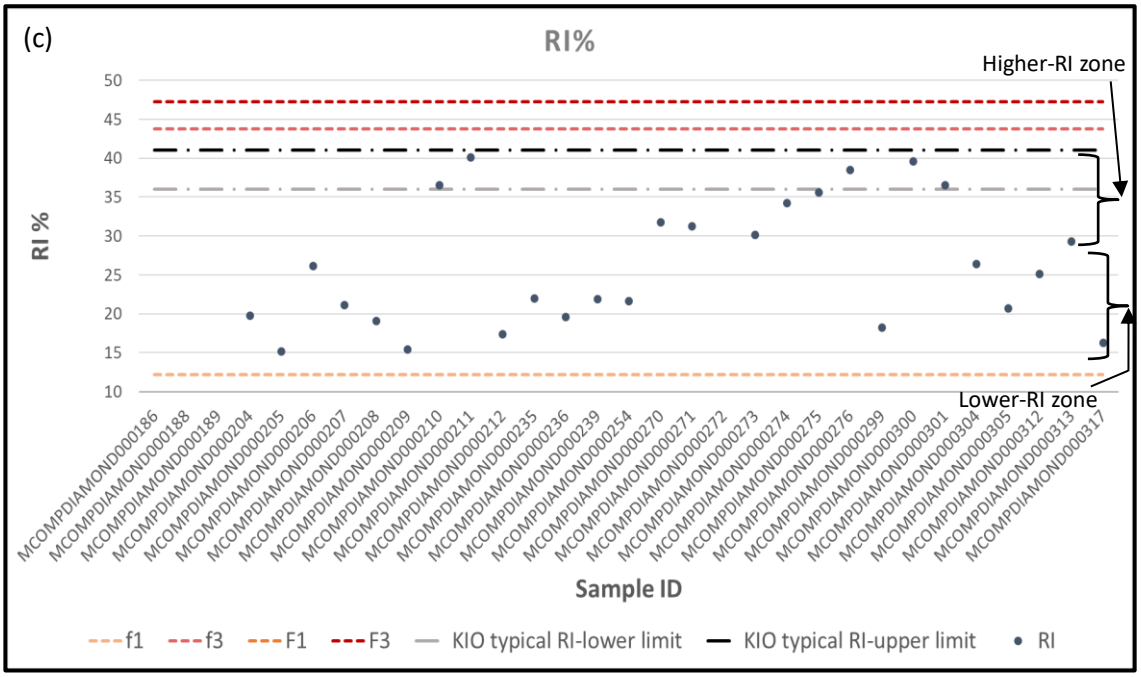
(c)
RI%
Higher-RI zone
Lower-RI zone
RI %
Sample ID
f1
f3
F1
F3
KIO typical RI-lower limit
KIO typical RI-upper limit
RI

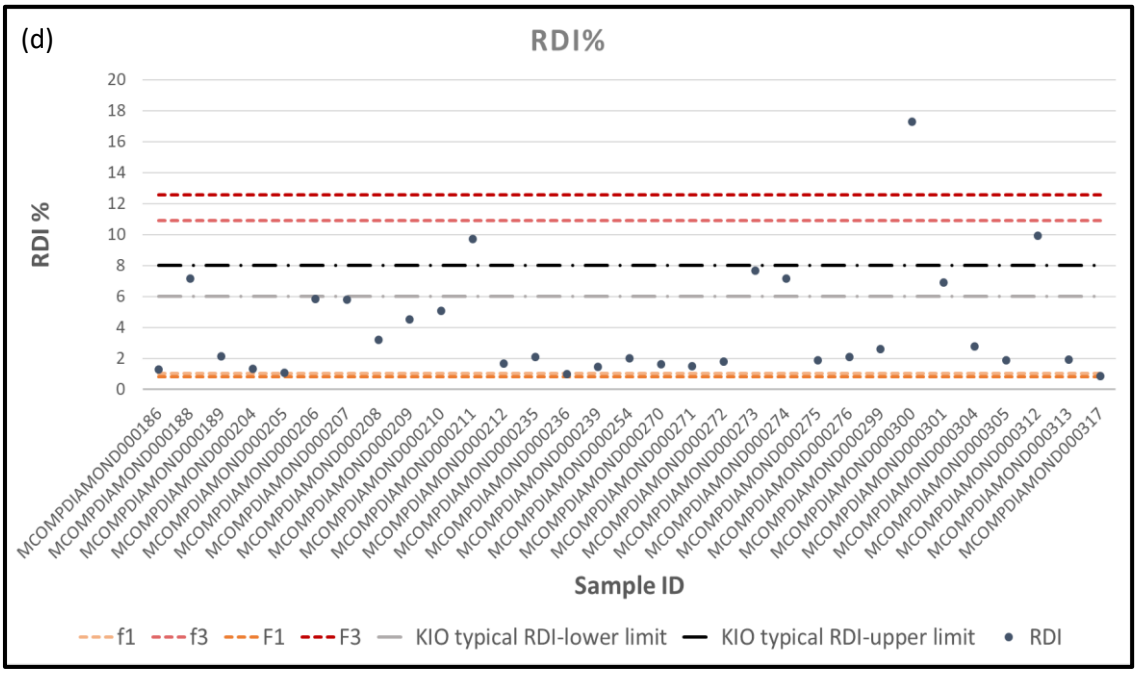
(d)
RDI%
RDI %
Sample ID
f1
f3
F1
F3
KIO typical RDI-lower limit
KIO typical RDI-upper limit
RDI

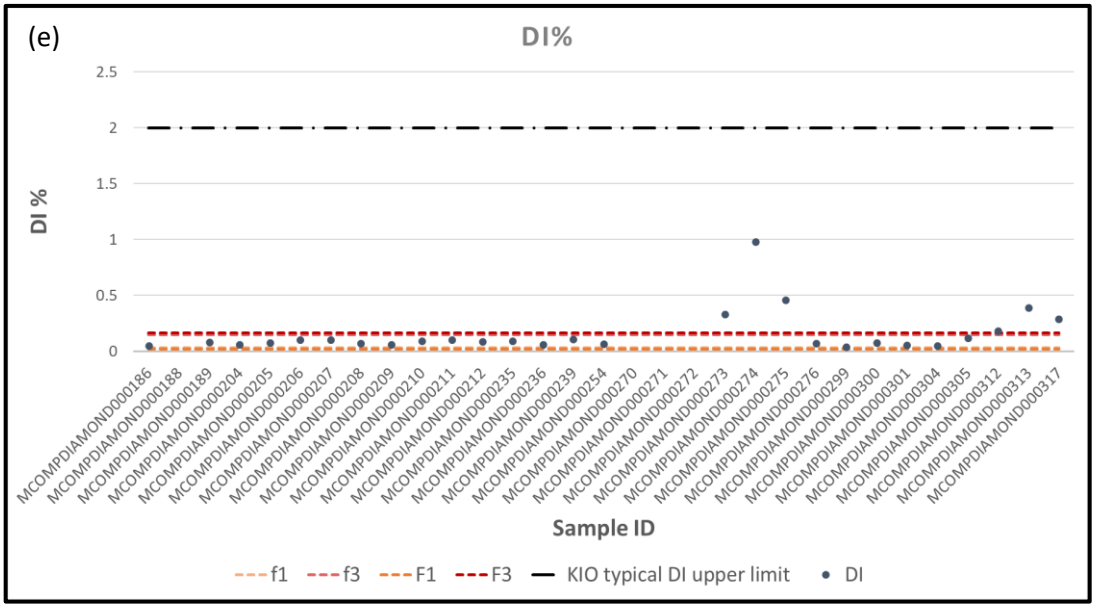

Figure 7.4 Identification of outliers in (a) AI, (b) TI, (c) RI, (d) RDI and (e) DI results. Mild outliers occur beyond fences f1 and f3, whilst significant outliers occur beyond fences F1 and F3. ID: identification.

Sample MCOMPDIAMOND000208, 299 and 300 occur as significant outliers in the AI and TI datasets. Upon inspection of the data, MCOMPDIAMOND000208 was found to be the only sample containing totally disintegrated core, in contrast to the competent or broken core exhibited in the remaining samples. This suggests a relationship between competency, AI and TI, and that the totally disintegrated core samples should be analysed as a separate data set. MCOMPDIAMOND000299 and 300 are obtained from hole KS057_M, which is the only hole to the west of a major NNW-trending strike-slip fault (Figure 7.5– "fault A"). These samples are logged as broken and competent, suggesting that an additional factor, besides competency, affects the AI and TI of ore. It is possible that all ore west of the fault A has undergone more extensive deformation than the remaining ore due to movement along the fault. However, further data from this area is required to substantiate this theory.

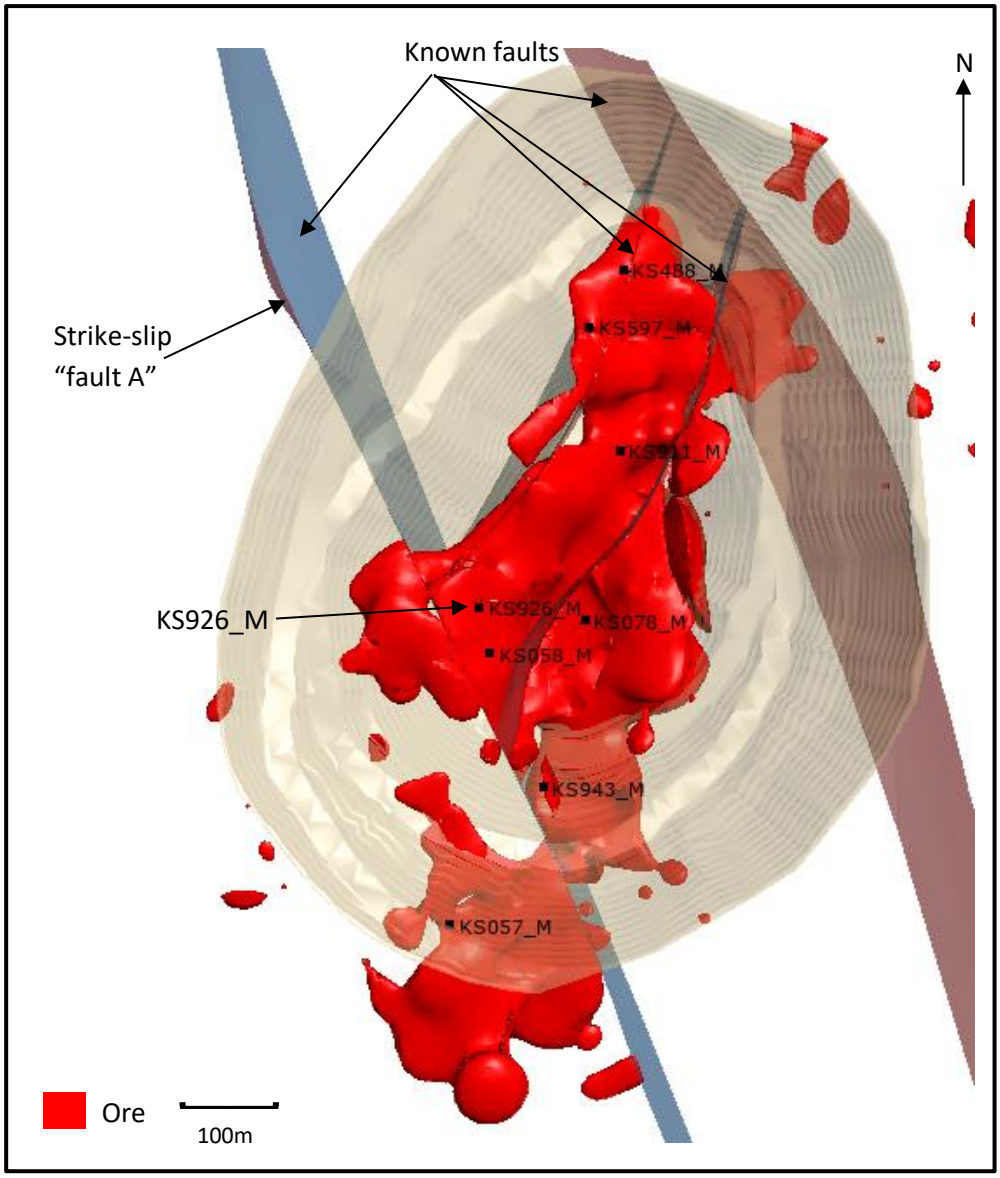

Figure 7.5 Illustration of the Kapstevel South pit with geometallurgical drill holes and known faults

No significant outliers are found in the RI dataset. However, visual inspection of the scatter plot suggests two zones of samples: the higher- and lower-RI zone. Inspection of these samples show that all samples in the higher-RI zone contain a laminated texture, while those in the lower zone are massive. The only sample not conforming to this trend is MCOMPDIAMOND000239, which contains steeply dipping laminations but behaves in the same way as massive ore. This sample should be further investigated for lab error, or for an alternative reason for the low reducibility. Samples MCOMDIAMOND000270 to 276 do not display distinct laminations but break along lamination planes and contain

lamination-parallel veining. This reinforces the importance of careful logging in order to distinguish between ambiguous ore textures that exhibit different metallurgical properties. Samples MCOMPDIAMOND000270 to 276 belong to hole KS926_M, which is close to the intersection of two major faults in KSS (Figure 7.5). Fluid flow and deformation along these two faults may have caused overprinting of the original laminated texture. Due to the two distinct zones in Figure 7.4 c, further data analysis will separate laminated and massive hematite samples.

The dataset for RDI contains only MCOMPDIAMOND000300 as a significant outlier. This sample does not display any obvious differences to the remaining ore samples. However, it is derived from hole KS057_M – the same hole exhibiting abnormal AI and TI values. This reinforces the theory that ore to the west of strike-slip fault A has undergone different geological processes, resulting in a change in physical and metallurgical properties.

Samples MCOMPDIAMND000211 and 312 exhibit higher RDI values than the typical upper limit for KIO. The only difference between these and the remaining samples is the presence of small amounts of goethite.

The DI dataset contains 5 significant outliers displaying high DI values. Four of these samples display remnant chert banding. The high-DI values also correlate with high-silica values when plotted spatially (Figure 7.6). It is important to note that higher silica contents only lead to higher DI values when the silica is present as chert bands that are at least 1cm thick. For example, high silica values are also observed in MCOMPDIAMOND000211 of hole KS488_M, but this is due to thin quartz veins. This high-silica sample does not show a significant change in DI.

MCOMPDIAMOND000317 yields a high DI value but does not contain thick chert lenses. There are no obvious differences between this sample and the remaining ore and more data is required to ascertain the reason for this higher DI value.

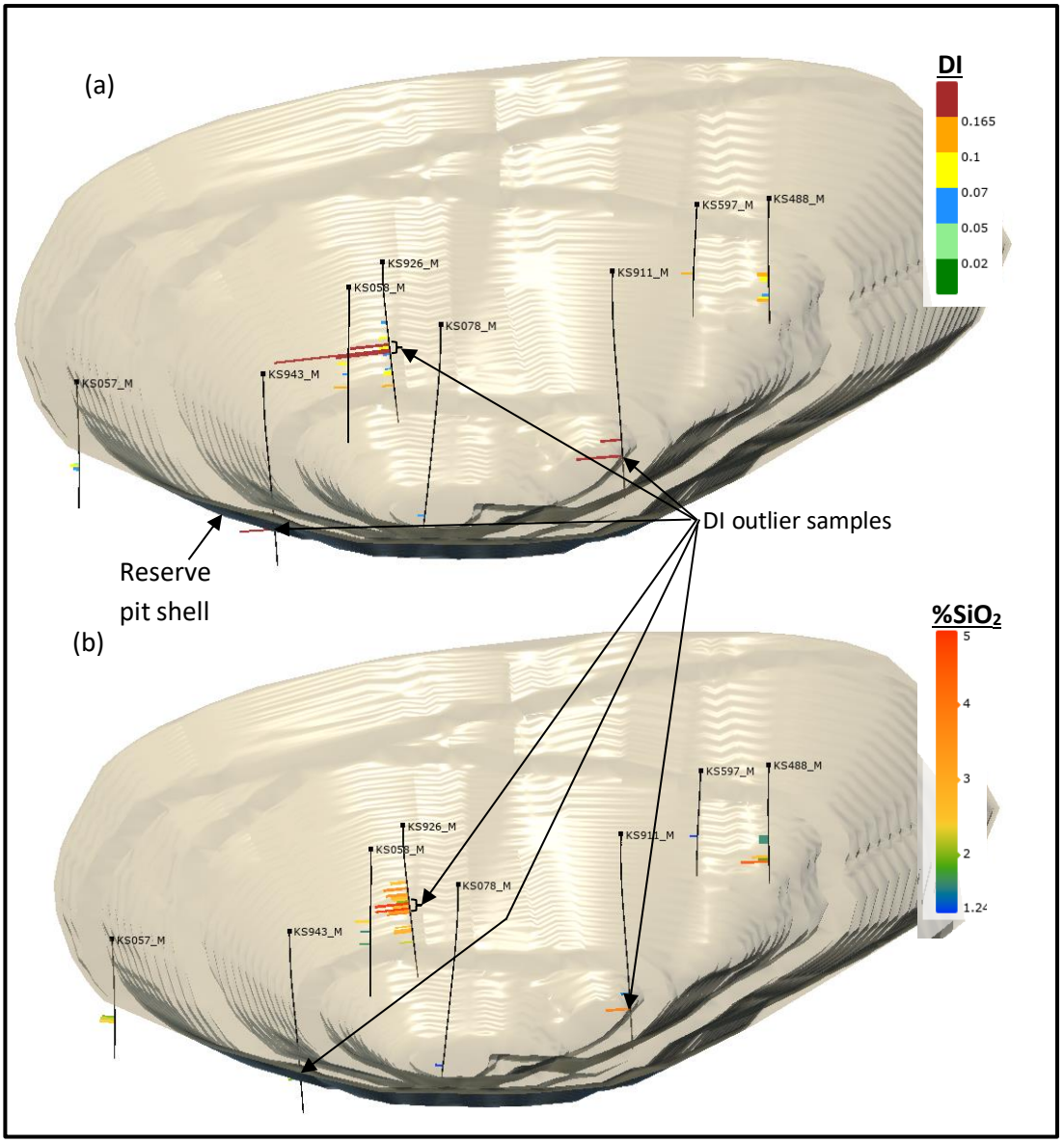

Figure 7.6 a) DI results in KSS and (b) SiO_2 percentages of DI samples

Data box plots

Results are plotted as separate box plots, based on the geological features that affected results during the identification of outliers. This was done in order to check for segregations that may extend to the remaining physical and metallurgical properties.

Figure 7.7 shows box plots of each physical and metallurgical property, separated according to rock competency. MCOMPDIAMOND000299 and 300 are analysed separately as “new geomet zone” in the AI and TI datasets. This is due to indications that the geographic source area west of fault A may exhibit different physical properties to the rest of the deposit. The plots visually confirm that totally disintegrated core displays AI

and TI values significantly different to the remaining competencies. Removing totally disintegrated core from the KSS box plot results in a data distribution that is closer to normal. There is no clear distinction between the respective competencies of RI, RDI and DI, and competency is not believed to affect these properties.

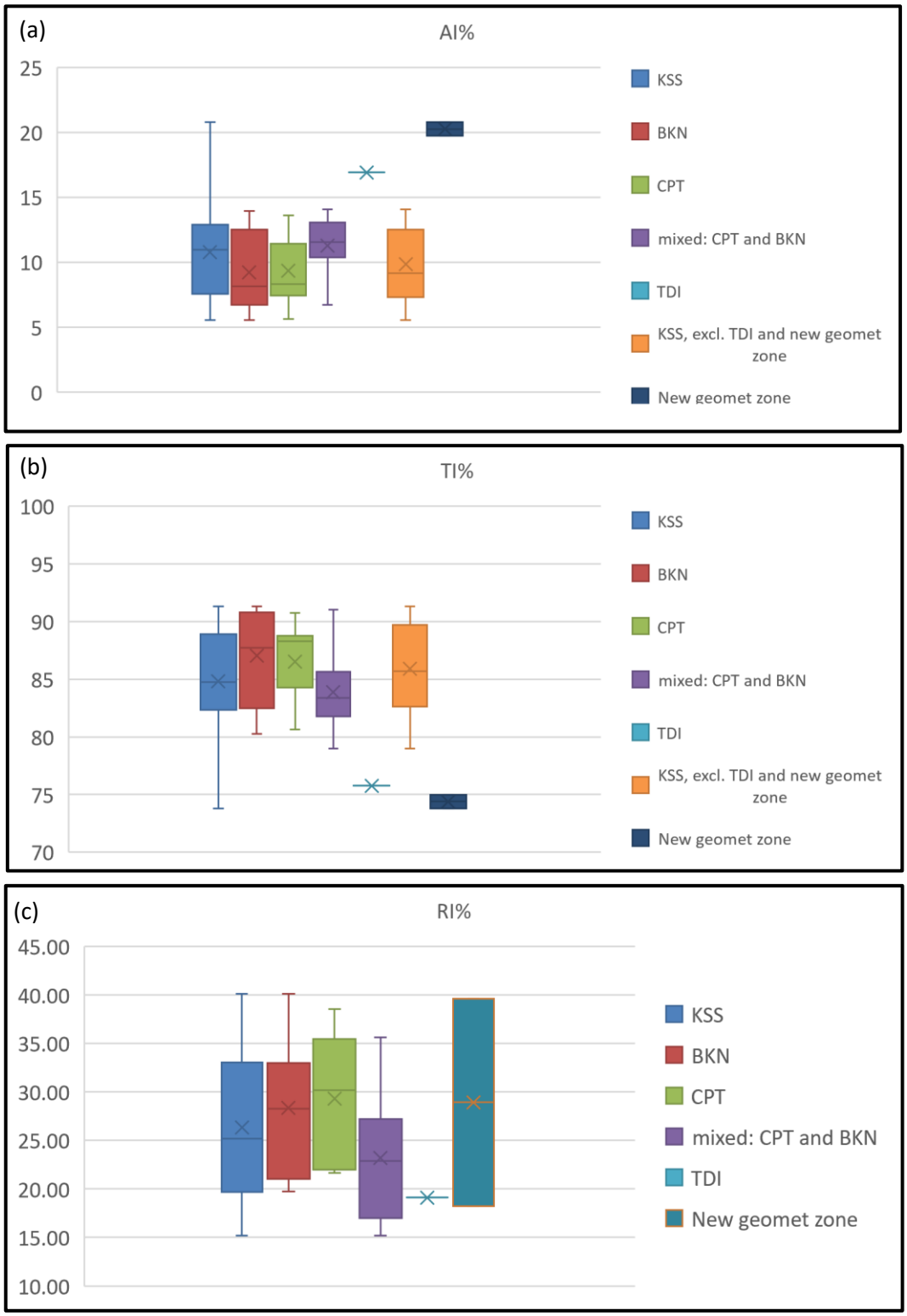

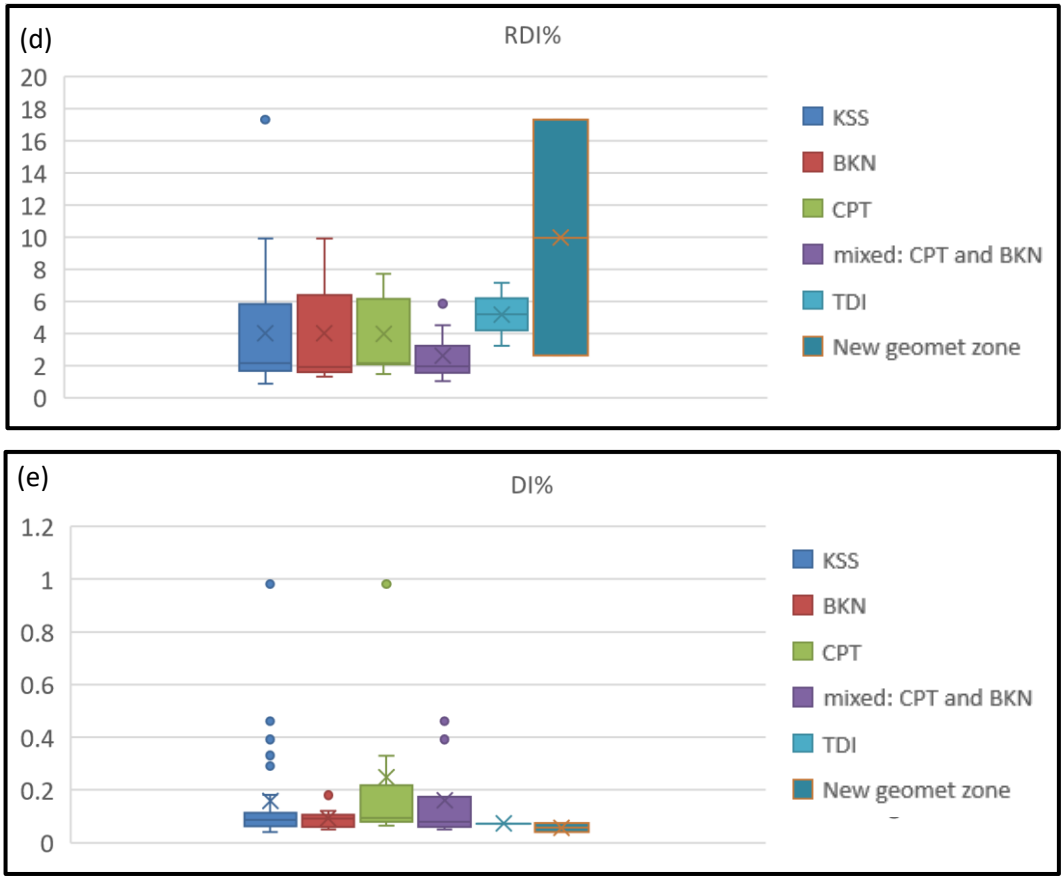

Figure 7.7 Box plots of (a) AI, (b) TI, (c) RI, (d) RDI and (e) DI, separated based on rock competency. KSS: entire Kapstevel South; BKN: broken; CPT: competent; CPT, BKN: mixture of competent and broken; TDI: totally disintegrated

Figure 7.8 displays box plots of each physical and metallurgical property, separated based on rock texture. Only massive and laminated hematite samples have been encountered in KSS thus far. The box plots confirm that laminated RI values are significantly higher than massive, with the minimum laminated RI value occurring just above the maximum massive RI value. Results for DI show potential differentiation between laminated and massive hematite, however this is likely due to remnant chert bands which have only been observed in laminated ore samples thus far.

AI and TI show slight differences between massive and laminated ore. There is no significant difference between the RDI properties of laminated and massive ore.

Figure 7.9 shows the physical and metallurgical properties of KSS, separated based on relative chert content. The only property showing a significant difference in results is DI, confirming the different DI properties of high-chert ore.

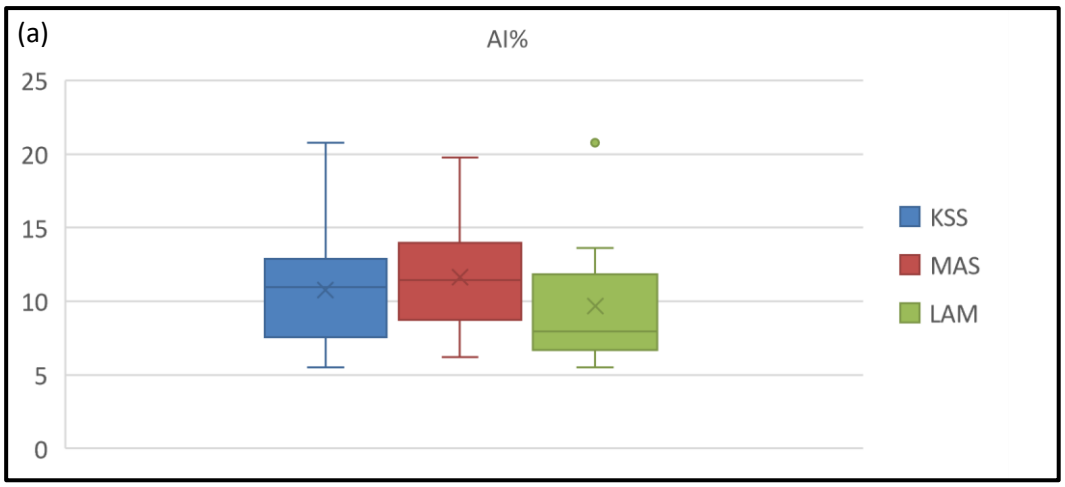
(a)
AI%
25
20
15
10
5
0
KSS
MAS
LAM

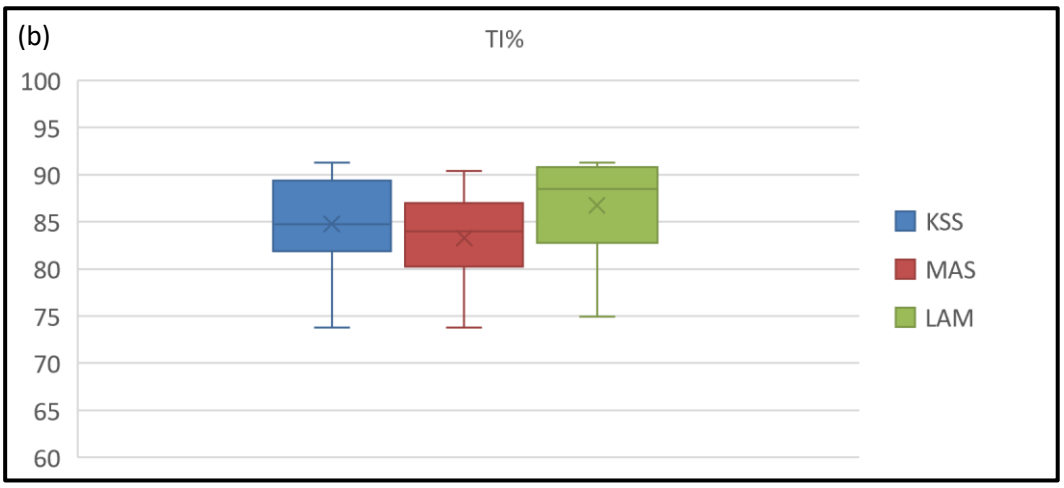
(b)
TI%
100
95
90
85
80
75
70
65
60
KSS
MAS
LAM

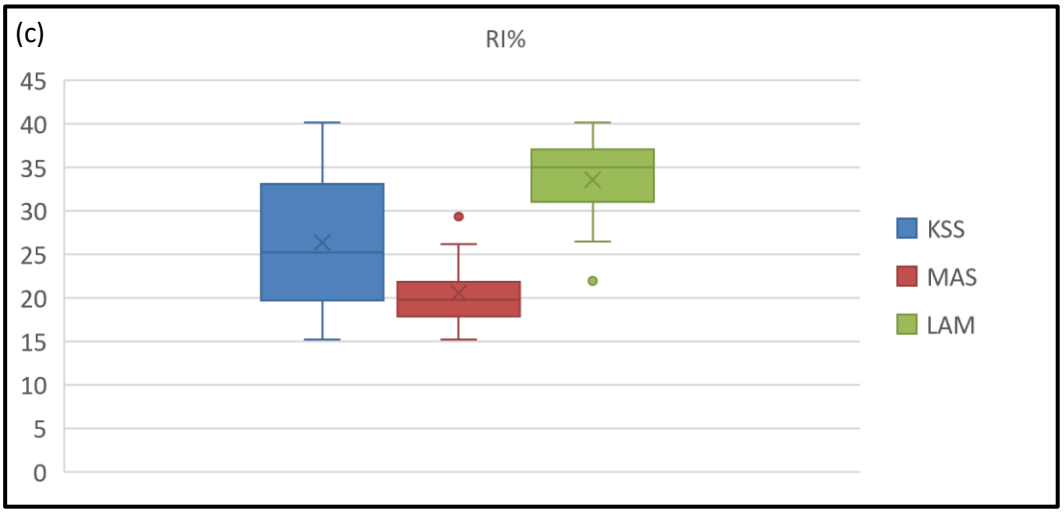
(c)
RI%
45
40
35
30
25
20
15
10
5
0
KSS
MAS
LAM

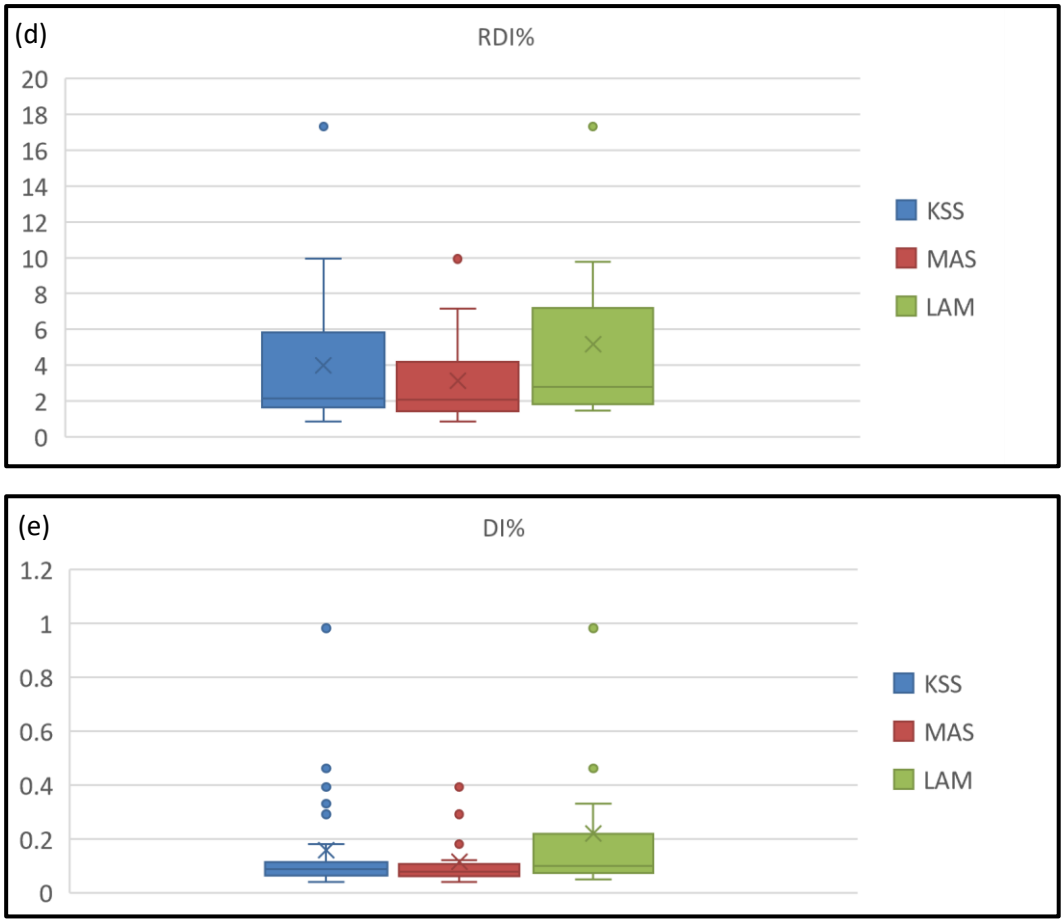

Figure 7.8 Box plots of (a) AI, (b) TI, (c) RI, (d) RDI and (e) DI, separated based on rock texture.

KSS: entire Kapstevel South; MAS: massive; LAM: laminated

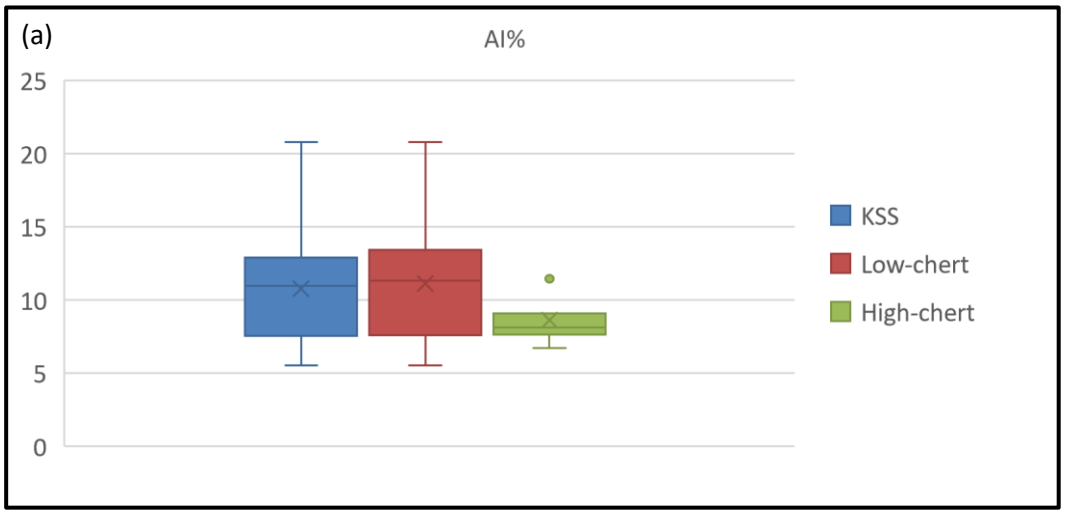

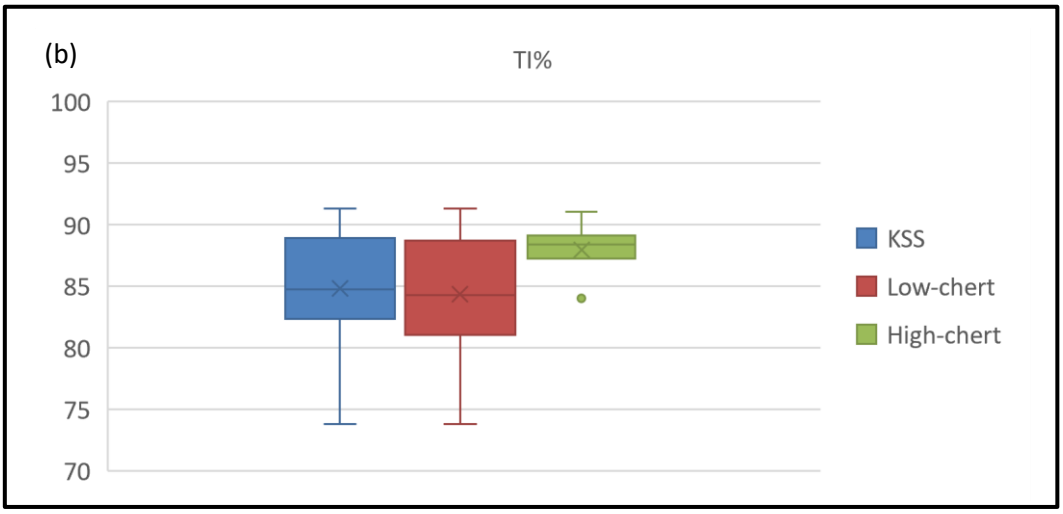
(b)
TI%
100
95
90
85
80
75
70
KSS
Low-chert
High-chert

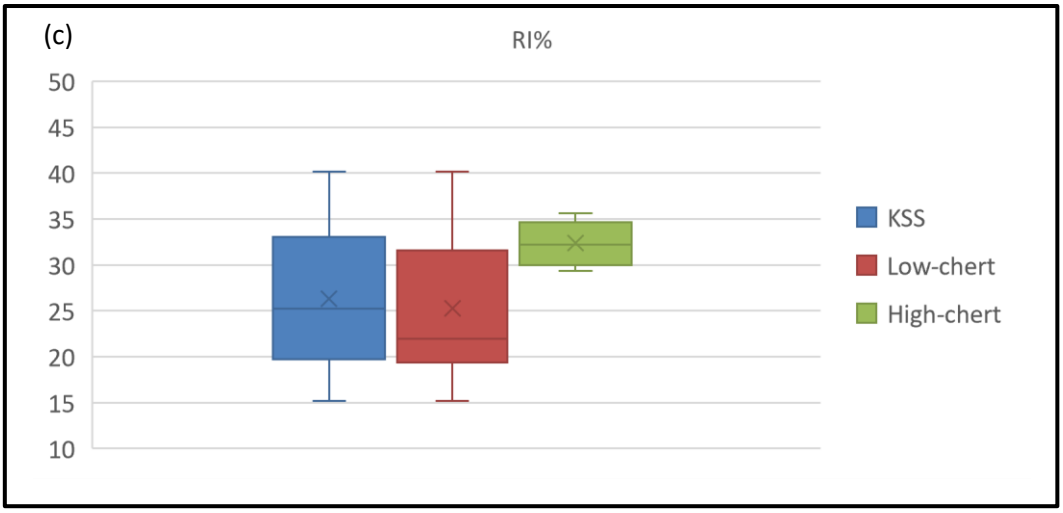
(c)
RI%
50
45
40
35
30
25
20
15
10
KSS
Low-chert
High-chert

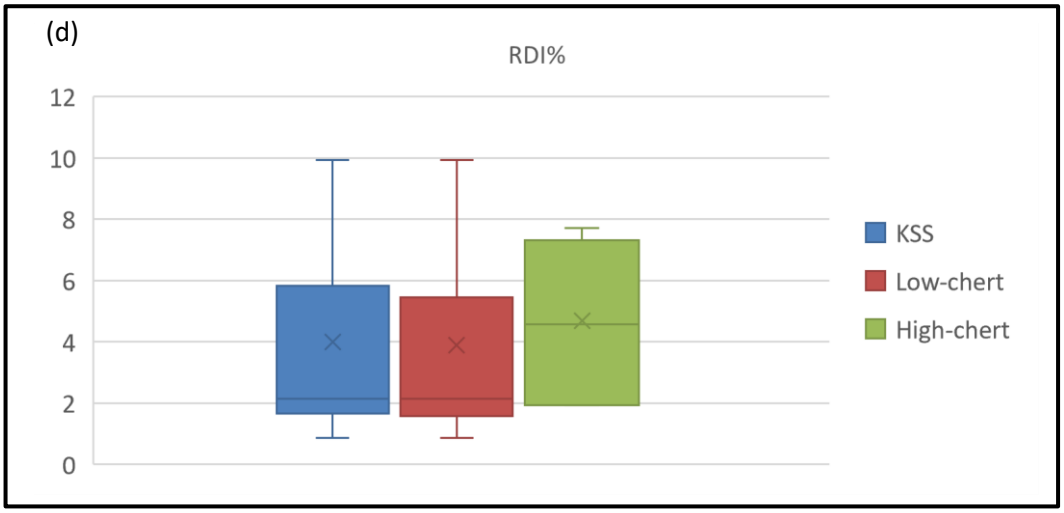
(d)
RDI%
12
10
8
6
4
2
0
KSS
Low-chert
High-chert

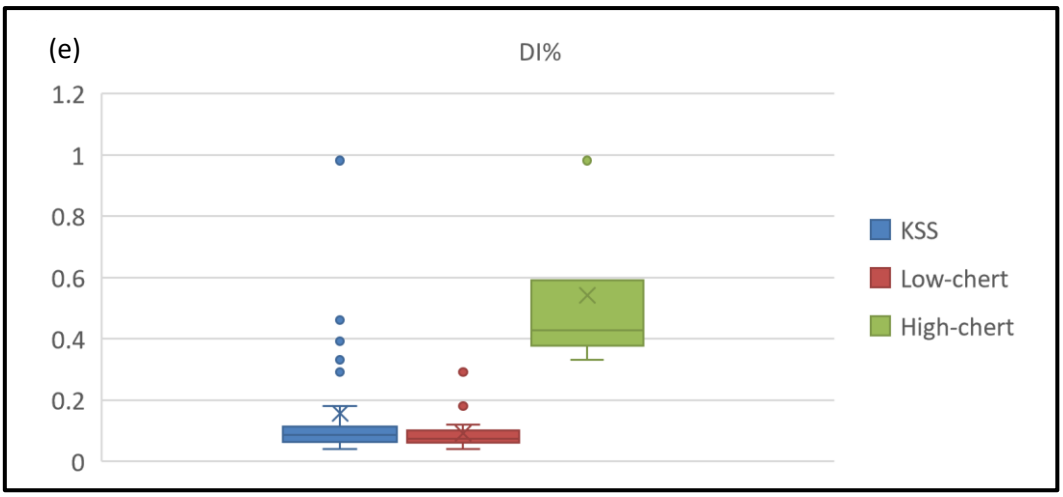

Figure 7.9 Box plots of (a) AI, (b) TI, (c) RI, (d) RDI and (e) DI physical and metallurgical results, separated based on chert content

7.4.2 Bivariate relationships between physical/metallurgical properties and assay data

The physical and metallurgical property data were individually plotted against chemical assay variables (Fe %, SiO_2 %, K_2O %, Al_2O_3 %, P %, S %, LOI %, moisture %, FeO % and Fe_2O_3 %) to check for any two-dimensional relationships. The physical and metallurgical results were grouped based on the textural, competency and chert-abundance criteria suggested during exploratory data analysis. The results of this are attached in Appendix D: Scatter plots of physical and metallurgical properties versus chemical assay data, along with the trendline R^2 value. The most suited trendline was selected based on the highest R^2 value - selecting between exponential, linear, logarithmic, polynomial and power trendlines.

Visual inspection and consideration of the R^2 values of the trendlines indicate that there are no bivariate correlations between physical/metallurgical properties and chemical assays. Correlations with moisture yield high R^2 values in places, but this deteriorates when more data is added to the plots. Similarly, the high R^2 values for high-chert DI results are likely due to a lack of data.

8 Results and Discussion

Table 8.1 summarises the physical and metallurgical subgroups identified thus far, derived from outlier identification and box plots. AI and TI results are subdivided based on competency, texture and the new geomet zone; RI is subdivided based on texture; DI is subdivided based on chert content; and RDI has not been subdivided. When compared to the results of Kapstevel South as a whole, all subgroups show improved CoV and thus less variation in the physical and metallurgical results. Average values can be assigned to each of these subgroups across the entire Kapstevel South deposit in order to calculate the physical and metallurgical properties of ore within reasonable confidence levels. The AI and TI of totally disintegrated ore is the main subgroup presenting a risk as there is only one sample for this category to date. RDI displays a relatively high CoV of 0.91 and should be subdivided in order to improve confidence in the assigned average value for ore. However, all RDI values are within the preferred limits for lump iron ore and do not pose a significant marketing risk.

Table 8.1 Summary of physical and metallurgical groupings thus far. BKN: broken, CPT: competent, TDI: totally disintegrated, MAS: massive ore, LAM: laminated ore, KSS: entire Kapstevel South, Std dev: standard deviation, n: number of samples, CoV: coefficient of variation

	AIX (BKN and CPT):				TIX (BKN and CPT):				AIX (TDI):	TIX (TDI):
	MAS	LAM	New geomet zone	KSS	MAS	LAM	New geomet zone	KSS	MAS	MAS
Mean	10.74	8.74	20.27	10.78	84.45	87.74	74.39	84.81	16.91	75.77
Std. dev.	2.61	2.94	0.72	3.98	3.50	4.01	0.82	5.10	n/a	n/a
CoV	0.24	0.34	0.04	0.37	0.04	0.05	0.01	0.06	n/a	n/a
n	15	12	2	30	15	12	2	30	1	1

	RI:			RDI:	DI:		
	MAS	LAM	KSS	KSS	High-chert	Low-chert	KSS
Mean	20.51	33.59	26.32	3.99	0.54	0.09	0.16
Std. dev.	4.01	5.50	8.08	3.64	0.26	0.05	0.20
CoV	0.20	0.16	0.31	0.91	0.48	0.59	1.26
n	15	12	27	31	4	23	27

8.1 Substantiation of Geometallurgical Subdivisions

In this section, the subdivisions of Table 8.1 will be substantiated with geological reasoning. Firstly, the subdivision of AI and TI based on competency is considered. AI and TI are subdivided based on the same criteria due to the strong linear relationship between the two (Figure 8.1). Thus, the factors affecting one variable are likely to affect the other in the opposite way.

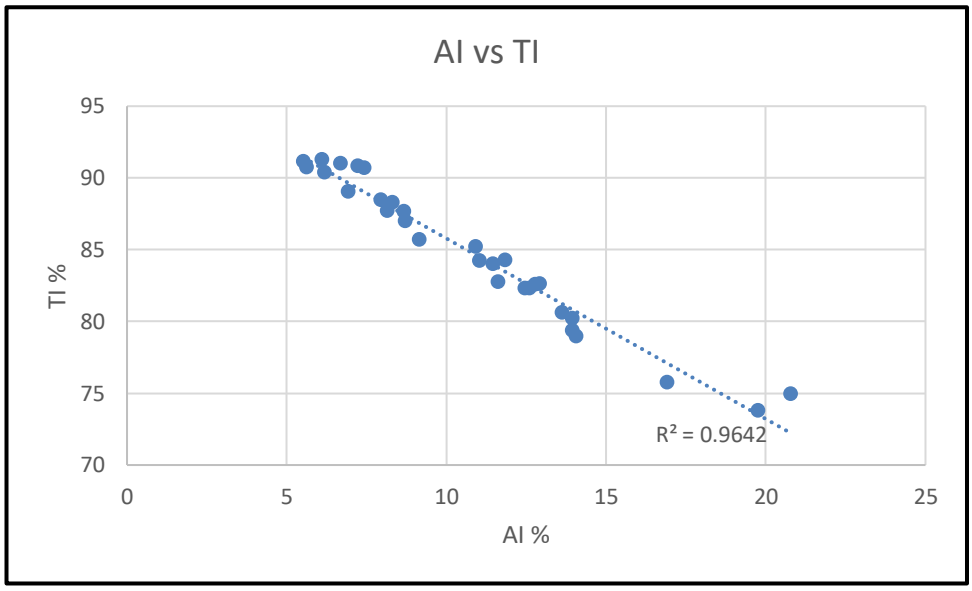

Figure 8.1 Scatter plot showing the AI versus TI results of Kapstevel South

The only sample containing totally disintegrated core exists within hole KS488_M, which is intersected by a normal fault. As explained by Rutter, Holdsworth and Knipe (2001), faulting in the upper crust involves the brittle breaking and high-friction sliding of rocks against each other. The result is fragmentation of surrounding rock and cohesion reduction. At times, this may be accompanied by the foliation of rock fabric (Rutter *et al.,* 2001). All these characteristics will lead to a weaker rock that is more susceptible to breakage during transport, yielding a higher AI and lower TI.

Figure 8.2 shows the factors that affect fault fabric and rheology, and thus the extent to which protolith AI and TI will be affected. The pressure and temperature of faults will not play a major role at Kolomela Mine, as all ore is mined in a shallow open cast environment. The remaining factors should be considered when assigning AI and TI values to fault-adjacent ore, and each fault treated individually. The greater the fault displacement and frequency of faults, the greater the impact on protolith AI and TI. Fluid alteration and weathering may also weaken the protolith and result in poorer AI and TI properties. When

logging geological core, it is important to take not of the competency, weathering and alteration of the ore, which will indicate amount that protolith AI and TI must be adjusted to compensate for weaker rock. The sample analysed in this study was logged as totally disintegrated, with no significant weathering or alteration. Thus, all ore occurring along this normal fault, and exhibiting the same properties, may be assigned the same AI and TI values.

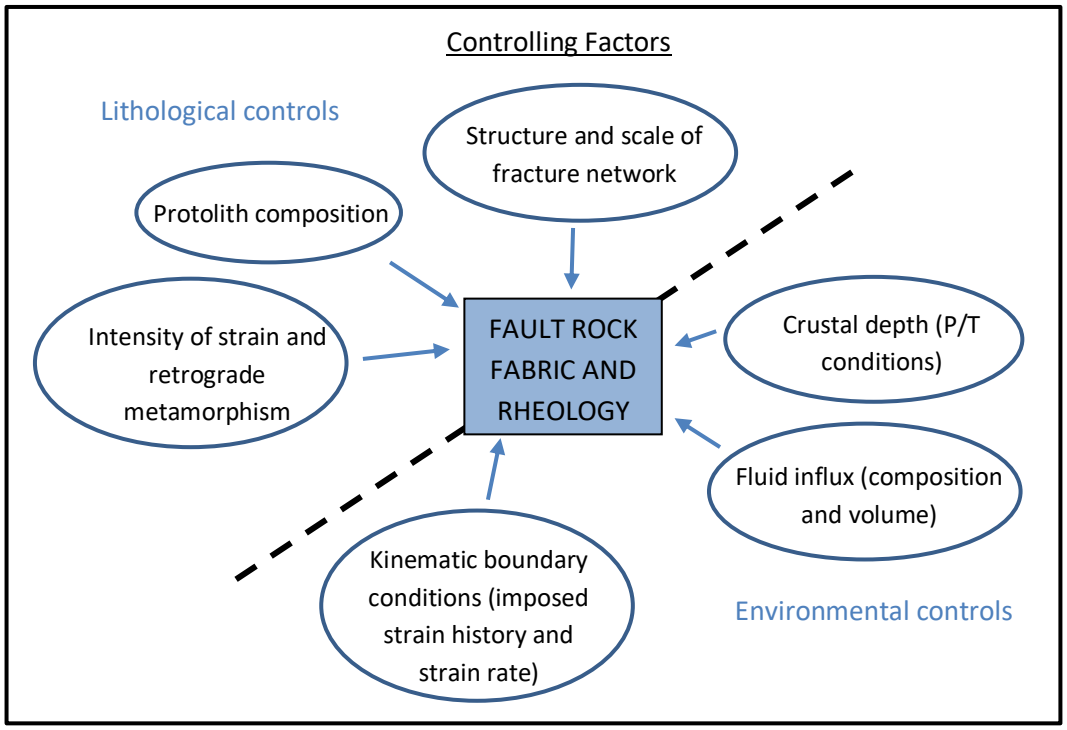

Figure 8.2 Diagram showing the factors influencing fault fabric and rheology, after (Holdsworth, Stewart, Imber and Strachan, 2001)

Next, the influence of massive and laminated hematite texture on AI and TI is considered. As previously mentioned, the ferhythmite microbands in laminated hematite are thought to be a result of geochemical varves produced by photosynthesising organisms (Beukes, 1983). It is possible that these geochemical varves bind the alternating laminations and result in a rock that is more resistant to impact than an isotropic rock such as massive hematite.

The reducibility of hematite in Kapstevel South is subdivided according to massive and laminated ore texture. According to literature (Anderson, 2014; Clout, 2003; Fernández-González *et al.*, 2017; Muwanguzi *et al.*, 2012), porosity plays a major role in the reducibility of ore, providing a greater surface area on which reduction can occur. There is insufficient data to compare relative densities (RD) of the 31 samples analysed during

the study, however Figure 8.3 shows the RD and iron content results of all samples at Kapstevel South, including those not sent for physical or metallurgical testing. It is evident that iron content is directly proportional to RD; as measured using the Archimedes principal to account for porosity (Berger, 2010). It can thus be expected that density will increase with iron content, except where ore contains higher porosity levels. Comparing the grade and relative density of massive and laminated hematite (Table 8.2), it is evident that laminated hematite contains a slightly higher average iron content, but lower RD. This is likely due to the slightly higher porosity of the ore, resulting in improved reducibility.

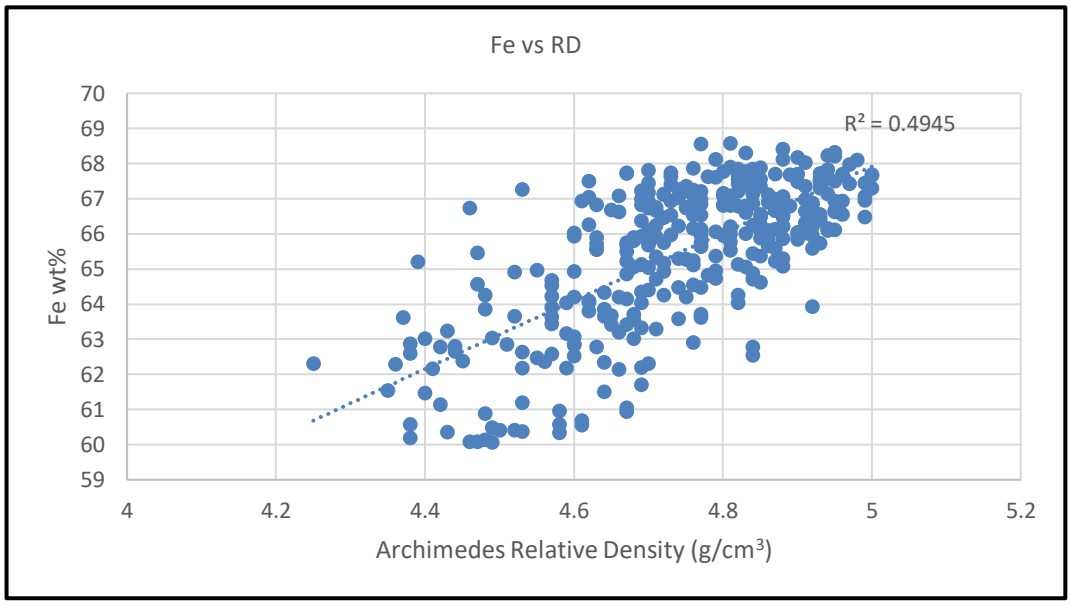

Figure 8.3 Scatter plot of iron content versus relative density at Kapstevel South

Table 8.2 Average relative density and iron content of massive and laminated hematite

Texture	Average RD	Average Fe
Massive	4.76	65.55
Laminated	4.72	65.79

The only sample that does not conform to the RI subdivision is MCOMPDIAMOND000239, which is found in drill hole KS597_M. This sample, although logged as laminated, behaved like massive ore during reduction. The possibility of a logging error was eliminated by inspecting core photographs, which show steeply dipping (near-vertical) laminations. The remaining factors known to affect reducibility are proportion of FeO and the presence of hematite versus magnetite (Fernández-González *et al.*, 2017; Geerdes *et al*., 2015; Maeda and Ono, 1985). The FeO of this sample is not significantly different to the remaining samples, eliminating this factor as a possible reason for the deviation. Unfortunately, the hole was not tested for magnetism while logging. It is thus recommended that all holes be tested for magnetite going forward. Until then, all laminated hematite in this area should be flagged for having lower RI.

The last subdivision is the high- and low-chert content of ore for DI. Although silica content is not related to DI, the presence of thick (>1 cm) chert remnants significantly increases the DI of the ore.

Several studies show that chert displays stress fractures and thermal damage when the rate of temperature increase is as low as 50˚C to 125˚C per hour (Patterson, 1995; Purdy, 1974 as cited in Patterson, 1995). During DI testing, the sample transitions from room temperature to a furnace of 700˚C in less than 30 minutes (International Organisation for Standardisation 8371, 2015) – much higher than the limits currently know in literature. The shattered chert leads to an ore sample with a higher ratio of fines, and thus higher DI.

RDI has not been subdivided in this study, however one sample that occurs above the typical limit for Kumba Iron Ore samples was investigated. Inspection of the geological log and photograph of this sample indicates the presence of small amounts of goethite (FeOOH) – an uncommon occurrence in the company's iron ore. According to Jang, K., Nunna, V.R.M., Hapugoda, S., Nguyen, A.V. and Bruckard, W.J. (2014), the reduction of goethite in the presence of CO and CO_2 gases can be described using the following equations:

$FeOOH \rightarrow Fe_2O_3 + H_2O$

$Fe_2O_3 + CO \rightarrow 2Fe_3O_4 + CO_2$

$Fe_3O_4 + CO \rightarrow 3FeO + CO_2$

$FeO + CO \rightarrow Fe + CO_2$

As previously mentioned, the main reason for the decrepitation of hematite is the increase in crystal structure volume upon transformation to magnetite, which weakens crystal structure and results in the breakdown of particles (Geerdes *et al.*, 2015).

A similar process is proposed for the reduction of goethite to hematite. There is currently no study confirming that the reduction of goethite causes particle disintegration. However, the crystal structure volume of goethite is known to be approximately 135-139Å and that of hematite is approximately 294-303Å (Ruan and Gilkes, 1995). This vast increase in crystal structure volume, along with the dense and low-porosity nature of Kapstevel South ore, would cause crystal structure weakening and disintegration of particles, as does occur during the reduction of hematite to magnetite.

There is insufficient data to confirm the effect of goethite on RDI, however the presence of goethite in ore should be closely monitored during mining and logging. Goethite-rich areas should be flagged as potentially exhibiting high-RDI values if encountered in the future.

8.2 Comparison of Kapstevel South Subdivisions with Data from the Leeuwfontein Pit

For statistical purposes, the analysis of only 31 samples from KSS is not ideal. To substantiate the correlations identified thus far, the metallurgical and physical results from the Leeuwfontein pit were investigated. This pit is slightly different geologically to KSS as the ore has been affected by karstification and larger-scale normal faulting (Basson *et al*., 2018) which preserved the ore from erosion. Thus, the average values for the metallurgical and physical properties may differ, but the same groupings may still apply. Here, the data were grouped according to the correlations identified in Kapstevel South and subsequently assessed.

The AI and TI results for 70 Leeuwfontein samples are displayed in Figure 8.4, grouped based on competency and texture. There is no clear difference between the AI and TI properties of these subgroups. Competent core exhibiting higher than usual AI values

were investigated and found to be brecciated, shaley and several were high in specularite. These textures were not observed in the KSS samples and did not affect groupings. It is thus suggested that extra precaution is taken should brecciated or high-specularite samples be observed in KSS in the future. These samples could exhibit abnormal AI and TI and should be grouped separately.

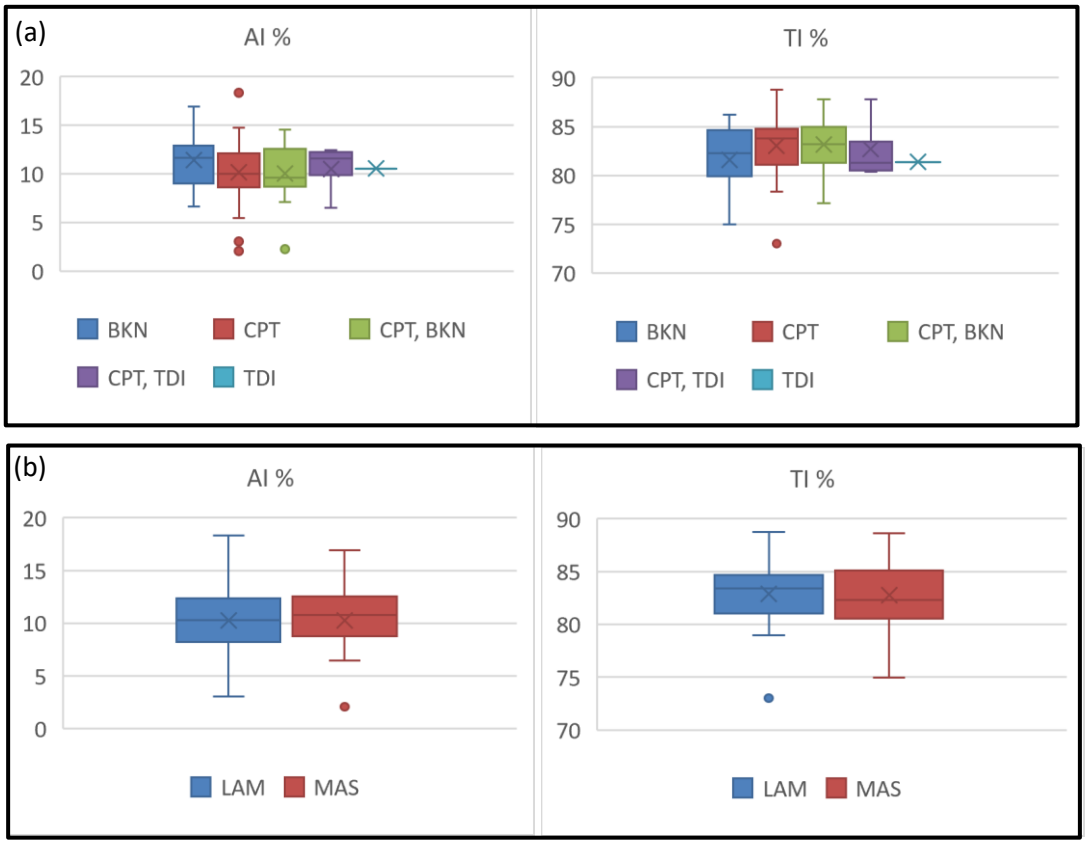

Figure 8.4 AI and TI boxplots of the Leeuwfontein pit, grouped based on (a) competency and (b) texture

Figure 8.5 shows the RI results for 68 Leeuwfontein samples. A clear separation is evident in this data, with laminated ore being more reducible than massive. The same relationship between RI and texture is observed in KSS (Figure 7.8 c), substantiating the separate modelling of ore textures. A total of 67 samples in Leeuwfontein were tested for DI. Of these, no samples contained significant chert pods or lenses. The resulting narrow range for DI is shown in Figure 8.6, which correlates with the "low-chert" DI values of KSS shown in Figure 7.9 e. This confirms that the absence of chert pods and lenses in samples result in lower DI values. Several outliers in the Leeuwfontein samples fall within the "high-chert" DI range. Inspection of these samples showed the presence of calcite veins. This

feature should thus be carefully monitored and logged in case another subgroup for high-calcite samples is required.

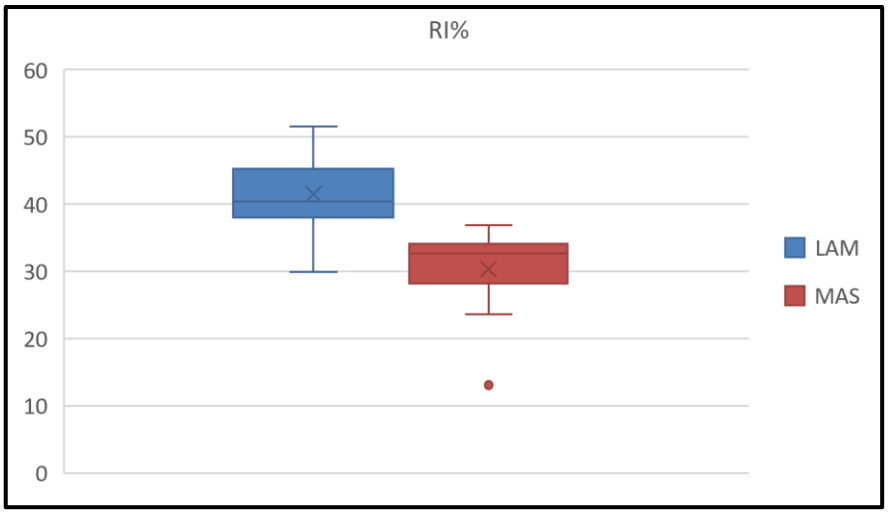

Figure 8.5 Boxplot showing the RI of the Leeuwfontein pit, grouped according to ore texture

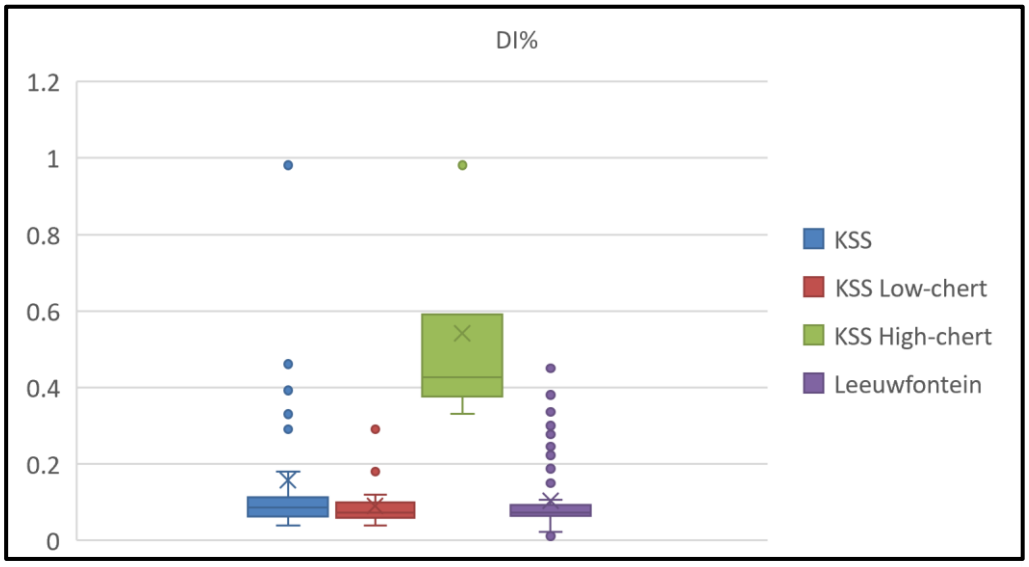

Figure 8.6 Boxplot showing the DI of KSS versus the Leeuwfontein pit

8.3 Comparison of Kapstevel South Physical/Metallurgical Properties with Typical Kumba Iron Ore Limits

The typical KIO limits for each physical and metallurgical property are displayed in Figure 7.4. Most KSS samples fall above the typical AI upper limit and below the typical TI lower limit for the company, but show improvement when compared to the currently-mined pits at Kolomela Mine (Table 7.2). This suggests that Sishen Mine, the remaining KIO mine,

typically lowers the AI and raises the TI values for the company. Once mining commences at KSS, the average AI and TI values for Kolomela Mine will improve and consequently enhance the AI and TI values of KIO.

Most ore in KSS is less reducible than the typical KIO and Kolomela ore and should be blended with higher-RI ore from other pits in order to minimise marketing risk. Where this is not possible, the ore must be marketed as low-RI to manage client expectations.

KSS ore is below or within the typical KIO values for RDI, with the uncommon presence of goethite being a potential risk to this property. The ore west of strike slip fault A (Figure 7.5) may exhibit significantly higher RDI values outside of typical KIO limits. However, this ore is not currently part of the reserve pit and is not planned to be mined. Further investigation of this area is recommended in case the reserve pit changes in the future. Excluding the ore west of fault A, the RDI of KSS is also far below the remainder of Kolomela Mine and will improve the quality of ore being dispatched, once the pit is mined.

All KSS ore, including outliers, is well-within the KIO limits for DI. The slight increase when compared to the rest of Kolomela Mine is negligible considering both values are low and within KIO limits.

In summary, all studied physical and metallurgical properties of KSS ore are favourable when compared to the current active pits of Kolomela Mine, except RI. The ore west of fault A should be monitored for abnormal physical and metallurgical properties. The mining of KSS is thus expected to improve the overall quality of exported KIO ore; if ore mined in the other KIO pits remains constant and reducibility is managed. Further test work and data analysis are required as the findings of this study are based on a limited number of samples. The analysed data provides a preliminary idea of the physical and metallurgical variation across KSS.

8.4 Comparison of Kapstevel South Physical and Metallurgical Subdivisions with Current Literature

The current physical and metallurgical correlations identified in literature are summarised in Table 8.3. Currently, there are insufficient UCS results for KSS to investigate the correlation between hardness, AI and TI. The gathering of point load or UCS data should be emphasised during future work at the mine as this could serve as an indicator of

changing AI and TI conditions. The main mineral encountered at KSS (and the rest of the mine) is hematite, hence the lack of mineralogical comparison for AI, TI and RI during the study.

Table 8.3 Summary of the AI, TI, RI, RDI and DI iron ore correlations in literature

Physical/ metallurgical property	Correlation	Reference
TI and AI	Ore with higher hardness levels exhibits lower AI and higher TI.	(Clout *et al.,* 2007)
	Mineralogy: hematite is harder than goethite and thus exhibits more favourable AI and TI.	(Clout and Manuel, 2015)
	Low porosity results in higher hardness and improved AI and TI properties.	(Clout and Manuel, 2015
RI	Slight increase in FeO has a negative effect on RI.	(Cores *et al.*, 2010)
	RI is higher in ore exhibiting greater porosity levels.	(Anderson, 2014; Clout, 2003; Fernández-González *et al*., 2017; Muwanguzi *et al.,* 2012)
	More hematite than magnetite is preferred for better RI.	(Fernández-González *et al.*, 2017; Maeda and Ono, 1985)
RDI	A higher bond strength between particles reduces RDI.	(Geerdes *et al.*, 2015)
	An increase in the proportion of FeO is favourable for RDI, provided the increase in FeO is due to magnetite content.	(Cores *et al.*, 2010; Geerdes *et al.*, 2015)
	Larger grain size increases RDI.	(van der Vyver *et al.*, 2009)
	The orientation of grain structure increases RDI.	(van der Vyver *et al*., 2009)
	Interconnected large pores enhances RDI.	(van der Vyver *et al.*, 2009)
	Hydrous minerals are known to increase RDI.	(van der Vyver *et al.,* 2009)
DI	The presence of water within the structure of iron minerals increases DI.	(Clout, 2003)
	Moisture and carbonate minerals increase the DI of ore.	(de Azevedo and Cardoso, 1983)
	Higher porosity results in lower DI.	(Lu *et al*., 2015)

Considering RD to be a function of porosity and iron content at Kapstevel South, it is possible to assess the effect of porosity on AI and TI by plotting the RD against these properties. Figure 8.7 shows the limited results available for RD, plotted against their AI and TI values. The RD has been standardised to remove the effect of iron content on this

value. This preliminary investigation shows no correlation in the data and the trend reported by Clout and Manuel (2015) cannot be confirmed. Further data is required to confidently assess the effect of porosity on AI and TI at KSS. However, this study indicates a correlation between core competency, AI and TI - adding to the correlations which have currently been identified in literature.

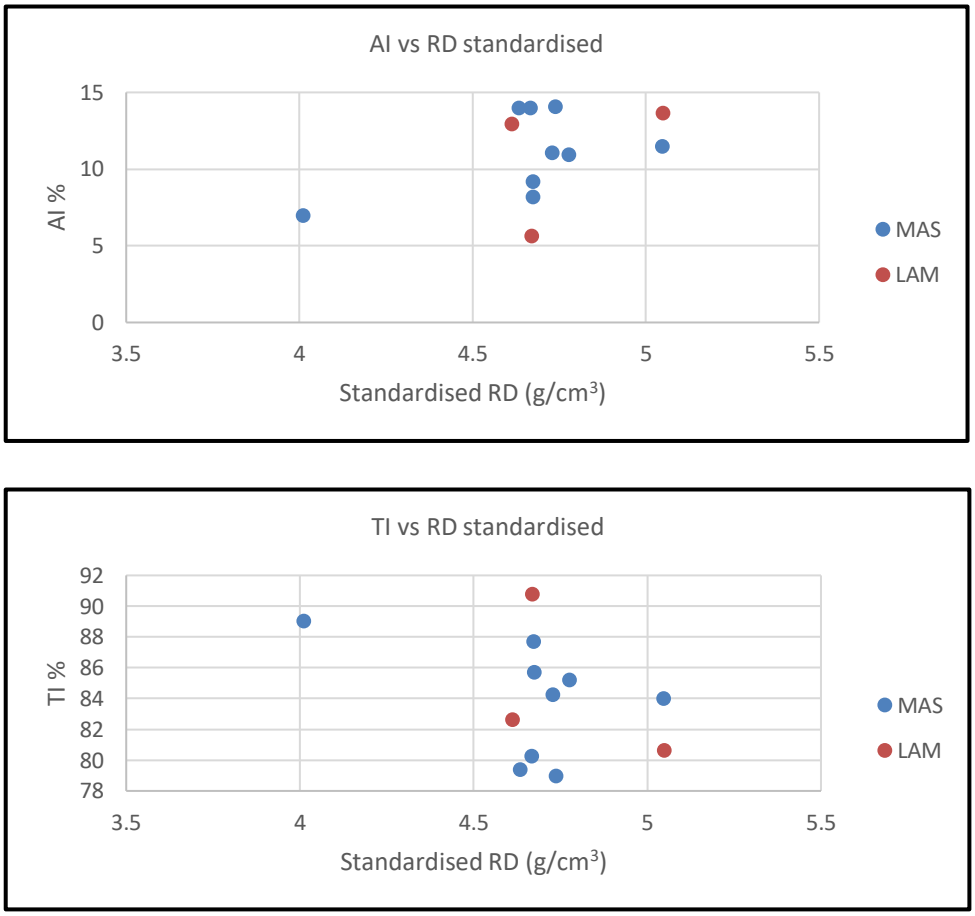

Figure 8.7 AI and TI versus standardised RD of samples at KSS

Changing FeO levels in the KSS samples does not have a significant effect on RI or RDI. This could be due to the occurrence of FeO in minerals other than magnetite, for example serpentine and goethite. Both serpentine and goethite have been observed in small amounts within KSS ore.

Although RD values are not available for majority of the analysed KSS samples, comparison of the RD and iron content of massive versus laminated ore in the whole of KSS indicates higher porosity levels in the latter. This confirms the correlations already observed in literature.

RDI has not been subdivided into low-variance groups in this study, thus there is no data to compare to the correlations of Table 8.3. However, the presence of goethite has been identified as a possible contributor to increased RDI and will add another correlation to literature if substantiated with further data.

KSS ore does not typically contain high levels of moisture or carbonate minerals that would affect DI. There is also currently insufficient data on RD or porosity to establish a relationship between these properties and DI. This study does, however, indicate a correlation between the presence of chert lenses or pods and higher DI values. This correlation has not yet been observed in literature.

9 Conclusion and Recommendations

The rapidly changing market conditions over the past 15 years have resulted in stronger competition between iron ore producers, forcing companies to lower costs and/or produce high-quality ore in order to attain premium iron ore prices. Kumba Iron Ore supplies a small fraction of the total iron ore available worldwide and cannot reap the benefits of economies of scale as much as its competitors. It thus becomes crucial for the company to fully understand and optimise the metallurgical and physical properties of the iron ore it produces. In doing so, the company will continue to secure its position as a quality producer of iron ore within the market, and consistently meet customer expectations. This study has helped understand the metallurgical and physical properties of iron ore at the KSS farm, where mining has yet to commence.

Ore texture, competency and the presence of chert lenses or pods is identified as being the primary features controlling AI, TI, RI, RDI and DI. Several correlations require further investigation to improve confidence in their results. Most importantly, it is recommended that more hardness (either UCS or point load) and RD data is collected for all samples that are sent for physical and metallurgical testing. This will confirm or reject a correlation between hardness, porosity, AI and TI. A mineralogical study of the ore may indicate the reason for high-RDI and high-AI ore in the extreme south of KSS, which differs from the rest of the deposit.

A correlation between DI and chert pods or lenses has been identified and confirmed when comparing with data from the Leeuwfontein pit. Further samples containing chert pods and lenses should be tested to substantiate this theory. Additionally, it is recommended that several non-DSO BIF samples be sent for DI testing. This will assess the extent to which chert impacts DI. It will also potentially provide high-DI data to be used in correlation studies. Non-DSO BIF is periodically used in the ore blend at Kolomela Mine and would affect the marketing of product beds containing this material.

The correlation between AI, TI and competency is evident when considering KSS data only. However, this correlation does not extend to the Leeuwfontein pit. This suggests that more factors, such as brecciated textures and specularite content, may also affect these properties. The occurrence of changing textures or mineral content should be monitored in KSS and flagged for AI and TI investigation.

The correlation between texture and reducibility is clear and carries a high confidence level. This is reinforced by the same correlation observed in samples from the Leeuwfontein pit.

AI, TI, RI, RDI and DI are not a linear function of chemistry at KSS, but are non-additive properties affected by structure and texture. Thus, encountering a new area with different mineralogy and structure may yield differing physical and metallurgical properties. This is mitigated by testing samples that occur across spatially representative cross-sections of the ore deposit, and across various ore textures. It is important to continue testing, collecting data, looking for changes in ore types, and refining correlations until results from all planned geometallurgical holes have been received. Meticulous geometallurgical logging should be continued in order to preserve a record of all variables that may later be identified as affecting physical or metallurgical properties. The current study is limited to 31 samples from KSS. Acquiring more data will add weight to the current findings and negate any small testing errors that may occasionally arise. It will also potentially allow for the correlation between multiple variables through multiple regression or projection pursuit regression.

The next step towards building a geometallurgical model is creating wireframes of the physical and metallurgical properties investigated. This includes wireframes separating ore of different competency and chert abundance to yield AI, TI and DI. Wireframes for the laminated and massive ore textures already exist and can be used to delineate areas of different RI values.

Wireframes can be assigned the average AI, TI, RI, RDI and DI values derived from this study to attain a spatial representation of these metallurgical and physical properties. Subsequently, metallurgical and physical properties can be included into the geological block model used during the planning process. This will allow the mining sequence to be planned in order to maximise company profit. Areas with varying metallurgical and physical properties may be mined and blended to achieve the product specifications required by the client. Where blending is not possible, client expectations can be managed in order to avoid disappointment and maintain company reputation.

Understanding the spatial variation in metallurgical and physical properties will allow the mine to target high-quality and profitable areas during strenuous times, such as dips in

iron ore price. Similarly, this ore can be stockpiled during favourable market conditions and used to help reduce company sensitivity to iron ore price fluctuations.

Spatial delineation of AI and TI values can help inform blast parameters and improve the lump:fine ratio of the mine, thus increasing profit. For example, high-AI areas that are planned to be stockpiled before blending, or that undergo more handling prior to crushing, can be blasted into coarser fragments to accommodate physical breakdown during transport. Alternatively, high-AI areas can be preferentially loaded directly into the crusher to avoid stockpiling, excessive handling and fines-generation.

In summary, all studied physical and metallurgical properties of KSS ore are slightly more favourable when compared to the current active pits of Kolomela mine. The only property presenting a marketing risk is RI which is lower than the average Kolomela sample. Iron ore from KSS should thus be blended with ore from other pits to mitigate this risk. Overall, the mining of the KSS deposit is expected to improve the quality of iron ore being exported by KIO.

References

Alchin, D., Botha, W.J., 2006. The structural/stratigraphic development of the Sishen South (Welgevonden) iron ore deposit, South Africa, as deduced from ground gravity data modelling. Applied Earth Science 115, 174–186

Alchin, D., Lickfold, V., Mienie, P.J., Nel, D., Strydom, M., 2008. An integrated exploration approach to the Sishen South deposit, Northern Cape Province, South Africa, and its implication for developing a structural/resource model for the deposits. Economic Geology (Society of Economic Geology Reviews) 15, 317–338

Alruiz, O.M., Morrell, S., Suazo, C.J., Naranjo, A., 2009. A novel approach to the geometallurgical modelling of the Collahuasi grinding circuit. Minerals Engineering 22, 1060–1067

Altermann, W., 1997. Sedimentological evaluation of Pb-Zn exploration potential of the Precambrian Griquatown Fault Zone in the Northern Cape Province, South Africa. Mineralium Deposita 32, 382–391

Altermann, W., Hälbich, I.W., 1991. Structural history of the southwestern corner of the Kaapvaal Craton and the adjacent Namaqua realm: new observations and a reappraisal. Precambrian Research 52, 133–166

Altman, D.G., Bland, J.M., 2005. Standard deviations and standard errors. British Medical Journal 331, 903

American Iron and Steel Institute, 2005. How a Blast Furnace Works. Accessed 5 April 2019, https://web.archive.org/web/20070510164459/http://www.steel.org/AM/Template.cfm?Section=Home&template=%2FCM%2FHTMLDisplay.cfm&ContentID=5433

Anderson, K.F.E., 2014. Geometallurgical Evaluation of the Nkout (Cameroon) and Putu (Liberia) Iron Ore Deposits (PhD Thesis). University of Exeter.

Angerer, T., Duuring, P., Hagemann, S.G., Thorne, W., McCuaig, T.C., 2015. A mineral system approach to iron ore in Archaean and Palaeoproterozoic BIF of Western Australia. Geological Society, London, Special Publications 393, 81–115

Angerer, T., Hagemann, S.G., Danyushevsky, L.V., 2012. Geochemical evolution of the banded iron formation-hosted high-grade iron ore system in the Koolyanobbing Greenstone Belt, Western Australia. Economic Geology 107, 599–644

Ashley, K.J., Callow, M.I., 2000. Ore Variability: Exercises in geometallurgy. Engineering and Mining Journal 201, 24–28

Barlow, L., 2020. Preferred Ranges. [email]

Barlow, L., 2018. Geometallurgy Samples [PowerPoint presentation]

Basson, I.J., Thomas, S.A.J., Stoch, B., Anthonissen, C.J., McCall, M.-J., Britz, J., Macgregor, S., Viljoen, S., Nel, D., Vietze, M., Stander, C., Horn, J., Bezuidenhout, J., Sekoere, T., Gous, C., Boucher, H., 2018. The structural setting of mineralisation at Kolomela Mine, Northern Cape, South Africa, based on fully-constrained, implicit 3D modelling. Ore Geology Reviews 95, 306–324

Berger, M.B., 2010. The importance and testing of density/porosity/permeability/pore size for refractories. Presented at the The Southern African Institute of Mining and Metallurgy Refractories 2010 Conference, The Southern African Institute of Mining and Metallurgy, pp. 101–116

Beukes, N.J., 1983. Palaeonenvironmental setting of iron-formations in the depositional basin of the Transvaal Supergroup, South Africa, in: Trendall, A.F., Morris, R.C. (Eds.), Iron Formation: Facts and Problems, Developments in Precambrian Geology 6. Elsevier, Netherlands, pp. 131–210

Beukes, N.J., Gutzmer, J., 2008. Origin and paleoenvironmental significance of major iron formations at the Archean-Paleoproterozoic boundary. Reviews in Economic Geology 15, 5–47

Beukes, N.J., Gutzmer, J., Mukhopadhyay, J., 2003. The geology and genesis of high-grade hematite iron ore deposits. Applied Earth Science 112, 18–25

Beukes, N.J., Smit, C.A., 1987. New evidence for thrust faulting in Griqualand West, South Africa: implications for stratigraphy and the age of red beds. South African Journal of Geology 90, 378–394

BHP, 2018. BHP operational review for the year ended 30 June 2018, accessed 25 February 2020, https://www.bhp.com/investor-centre/financial-results-and-operational-reviews/

Clout, J.M.F., 2006. Iron formation-hosted iron ores in the Hamersley Province of Western Australia. Applied Earth Science 115, 115–125

Clout, J.M.F., 2003. Upgrading processes in BIF-derived iron ore deposits: implications for ore genesis and downstream mineral processing. Applied Earth Science 112, 89–95

Clout, J.M.F., 1998. The effects of ore petrology on downstream processing performance: a review. The Australian Institute of Mining and Metallurgy 4, 43–50

Clout, J.M.F., Manuel, J.R., 2015. Mineralogical, chemical, and physical characteristics of iron ore, in: Iron Ore Mineralogy, Processing and Environmental Sustainability, Woodhead Publishing Series in Metals and Surface Engineering. Elsevier, United Kingdom, pp. 45–84

Clout, J.M.F., Maré, E., Ilich, B., Brandli, R., Bradley, M., 2007. Simulation of product size distributions of a Marra Mamba iron ore-comparison of conventional drill and blast versus surface miner product at the Cloud Break Deposit, in: Proceedings of Iron Ore 2007 Conference. Australasian Institute of Mining and Metallurgy, Perth, Western Australia, pp. 235–240

Cope, I.L., Wilkinson, J.J., Boyce, A.J., Chapman, J.B., Herrington, R.J., Harris, C.J., 2008. Genesis of the pic de fon iron oxide deposit, Simandou Range, Republic of Guinea, West Africa, in: Hagemann, S., Rosíere, C., Gutzmer, J., Beukes, N. (Eds.), Banded iron formation-related high-grade iron ore, Reviews in Economic Geology. Society of Economic Geologists, Littleton, Colorado, USA, pp. 339–360

Cores, A., Babich, A., Muñiz, M., Ferreira, S., Mochon, J., 2010. The influence of different iron ores mixtures composition on the quality of sinter. Iron and Steel Institute of Japan International 50, 1089–1098

Cores, A., Verdeja, L.F., Ferreira, S., Ruiz-Bustinza, Ì., Mochón, J., 2013. Editor's Page: Iron ore sintering. Part 1. Theory and practice of the sintering process. Dyna 180 152–171

Cornell, R.M., Schwertmann, U., 2003. The iron oxides: structure, properties, reactions, occurences and uses, 2., completely revised and extended edition. Wiley-VCH, Weinheim

Coward, S., Vann, J., Dunham, S., Stewart, M., 2009. The primary-response framework for geometallurgical variables. Seventh International Mining Geology Conference, Perth, Western Australia, 109-113

Dalstra, H., Guedes, S., 2004. Giant hydrothermal hematite deposits with Mg-Fe metasomatism: A comparison of the Carajás, Hamersley and other iron ores. Economic Geology 99, 1793–1800

Dalstra, H.J., Rosiére, C.A., Hagemann, S., 2008. Structural controls on high-grade iron ores hosted by banded iron formation: A global perspective. Reviews in Economic Geology 15, 73–106

de Azevedo, A.T., Cardoso, M.B., 1983. Decrepitation of iron ores: a fracture-mechanics approach. Ironmaking Steelmaking 10, 49–53

de Villiers, P.R., Visser, J.N.J., 1977. The glacial beds of the Griqualand West Supergroup as revealed by four deep boreholes between Postmasburg and Sishen. The South African Journal of Geology 80, 1–8

Dohm, C.E., 2019. Assumptions and probability theory, leture notes, MINN7007 Statistical Evaluation of Ore Reserves, University of the Witwatersrand, delivered 11-22 February 2019

Dominy, S., O'Connor, L., Parbhakar-Fox, A., Glass, H., Purevgerel, S., 2018a. Geometallurgy—a route to more resilient mine operations. Minerals 8, 560

Dominy, S., O'Connor, L., Glass, H., Xie, Y., 2018b. Geometallurgical study of a gravity recoverable gold orebody. Minerals 8, 1–31

Elliott, R., 1988. Cast Iron Technology, Butterworth and Company Publishers, Great Britain, pp243

Evans, D.A.D., Beukes, N.J., Kirschvink, J.L., 2002. Paleomagnetism of a lateritic paleoweathering horizon and overlying Paleoproterozoic red beds from South Africa: Implications for the Kaapvaal apparent polar wander path and a confirmation of atmospheric oxygen enrichment. Journal of Geophysical Research 107, EPM 2-1-EPM 2-22

Evans, K.A., McCuaig, T.C., Leach, D., Angerer, T., Hagemann, S.G., 2013. Banded iron formation to iron ore: A record of the evolution of Earth environments? Geology 41, 99–102

Faria, G.L., Vianna, N.C.S., Jannotti, N., Vieira, C.B., 2010. Decrepitation of Brazillian manganese lump, in: Sustainable Future. Presented at the Twelfth International Ferroalloys Congress, Helsinki, Finland, pp. 449–456

Fernández-González, D., Martín-Duarte, R., Ruiz-Bustinza, Í., Mochón, J., González-Gasca, C., Verdeja, L.F., 2016. Optimization of sinter plant operating conditions using advanced multivariate statistics: intelligent data processing. The Journal of the Minerals, Metals and Materials Society 68, 2089–2095

Fernández-González, D., Ruiz-Bustinza, I., Mochón, J., González-Gasca, C., Verdeja, L.F., 2017. Iron ore sintering: quality indices. Mineral Processing and Extractive Metallurgy Review 38, 254–264

Figueiredo e Silva, R.C., Lobato, L.M., Rosíere, C.A., Hagemann, S., Zucchetti, S., Baars, F.J., Andrade, I., 2008. A Hydrothermal Origin for the Jaspilite-Hosted, Giant Serra Norte Iron Ore Deposits in the Carajas Mineral Province, Para State, Brazil, in: Hagemann, S., Rosíere, C., Gutzmer, J., Beukes, N. (Eds.), Banded iron formation-related high-grade iron ore, Reviews in Economic Geology. Society of Economic Geologists, Littleton, Colorado, USA, pp. 255–289

Fordyce, W. 1860. A history of coal, coke, coalfields and iron manufacture in Northern England, Sampson Law, Son and Co., London, U.K. 164pp

Forsythe, R., Meissner, C., Mohr, J., 1922. The Blast Furnace and the Manufacture of Pig Iron. United Publishers Corporation, New York, 371pp

Friedman, J., 1994. From Statistics to Neural Networks: Theory and Pattern Recognition Applications. Springer, Berlin, pp414

Friedman, J.H., Tukey, J.W., 1974. A Projection Pursuit Algorithm for Exploratory Data Analysis. IEEE Transactions on Computers, C–23, 881–890

Friese, A.E.W., Alchin, D.J., 2007. New insights into the formation, structural development, and preservation of iron ore deposits in the Northern Cape Province, South Africa. Presented at the Iron Ore 2005 Conference, Australasian Institute of Mining and Metallurgy

Geerdes, M., Chaigneau, R., Kurunov, I., Lingiardi, O., Ricketts, J., 2015. Modern Blast Furnace Ironmaking - an introduction, Third. ed. IOS Press BV, Amsterdam, Netherlands, 177pp

Gordon, H.J.J., Miller, J.A., Becker, M., 2018. Using mineralogy for early stage geometallurgical domain definition: a cast study of the Swartberg polymetallic sulphide deposit. Presented at the Geometallurgy Conference 2018, Back to the Future, The Southern African Institute of Mining and Metallurgy, Cape Town, pp. 121–132

Govender, M., Denivelle, F., Britz, J., 2018. Geometallurgical Drilling Guideline and Associated QC Protocol for Sampling, Sub-Sampling and Testwork (Rev 3)

Gross, G.A., Canada, G., Steet, B., 1980. A classification of iron formations based on depositional environments. The Canadian Mineralogist 18, 215–222

Hagemann, S.G., Angerer, T., Duuring, P., Rosiére, C.A., Figueiredo e Silva, R.C., Lobato, L., Hensler, A.S., Walde, D.H.G., 2016. BIF-hosted iron mineral system: A review. Ore Geology Reviews 76, 317–359

Herve, A., 2010. Coefficient of variation. Encyclopedia of research design 1, 169–171

Hoffman, P.F., Kaufman, A.J., Halverson, G.P., 1998. A Neoproterozoic snowball earth. Science 281, 1342–1346

Holdsworth, R.E., Stewart, M., Imber, J., Strachan, R.A., 2001. The structure and rheological evolution of reactivated continental fault zones: a review and case study. Geological Society, London, Special Publications 184, 115–137

Hsieh, L.-H., 2005. Effect of raw material composition on the sintering properties. The Iron and Steel Institute of Japan International 45, 551–559

Hunt, J., Berry, R., Bradshaw, D., Triffett, B., Walters, S., 2014. Development of recovery domains: examples from the Prominent Hill IOCG deposit, Australia. Minerals Engineering 64, 7–14

Hunt, J.A., Berry, R.F., 2017. Geological contributions to geometallurgy: A Review. Geoscience Canada 44, 103–118

International Energy Agency, 2019, Tracking Industry. IEA, accessed 24 February 2020, https://www.iea.org/reports/tracking-industry-2019

International Organisation for Standardisation 3271, 2015. Iron ores for blast furnace and direct reduction feedstocks - determination of the tumble and abrasion indices

International Organisation for Standardisation 4696-1, 2015. Iron ores for blast furnace feedstocks - determination of low-temperature reduction-disintegration indices by static method - Part 1: Reduction with CO, CO2, H2 and N2

International Organisation for Standardisation 7215, 2015. Iron ores for blast furnace feedstocks - determination of the reducibility by the final degree of reduction index

International Organisation for Standardisation 8371, 2015. Iron ores for blast furnace feedstocks - determination of the decrepitation index

Jang, K., Nunna, V.R.M., Hapugoda, S., Nguyen, A.V., Bruckard, W.J., 2014. Chemical and mineral transformation of a low grade goethite ore by dehydroxylation, reduction roasting and magnetic separation. Minerals Engineering 60, 14–22

Jensen, M.L., Bateman, A.M., 1981. Economic Mineral Deposits, John Wiley and Sons, New York, 386-442

Johnson, J.E., 1918. The Principles Operation and Products of the Blast Furnace, First. ed. McGraw-Hill Book Company, Inc, London

Keeney, L., Walters, S.G., 2011. A methodology for geometallurgical mapping and orebody modelling, in: The First AUSIMM International Geometallurgy Conference, 10. The Australasian Institute of Mining and Metallurgy, Brisbane, Australia, pp. 217–225

Kirschvink, J.L., 1992. Late Proterozoic low-latitude global glaciation: the Snowball Earth in: The Proterozoic Biosphere: A multidisciplinary study, Schopf, K.W and Klein, C. (eds). Cambridge University Press, New York, pp51-52

Klein, C., 2005. Some Precambrian banded iron-formations (BIFs) from around the world: Their age, geologic setting, mineralogy, metamorphism, geochemistry, and origin. American Mineralogist 90, 1473–1499

Klein, C., Beukes, N.J., 1989. Geochemistry and sedimentology of a facies transition from limestone to iron-formation deposition in the early Proterozoic Transvaal Supergroup, South Africa. Economic Geology 84, 1733–1774

Klein, C., Ladeira, E., 2004. Geochemistry and mineralogy of Neoproterozoic Banded Iron-Formations and some selected, siliceous manganese formations from the Urucum District, Mato Grosso Do Sul, Brazil. Economic Geology 99, 1233–1244

Krapež, B., Barley, M.E., Pickard, A.L., 2003. Hydrothermal and resedimented origins of the precursor sediments to banded iron formation: sedimentological evidence from the Early Palaeoproterozoic Brockman Supersequence of Western Australia: Resedimented origins of banded iron formation. Sedimentology 50, 979–1011

Kumba Iron Ore Limited, 2019a. Ore Reserve (and Saleable Product) and Mineral Resource Report 2018, accessed 10 January 2020, https://www.angloamericankumba.com/investors/annual-reporting/reports-archive/2018

Kumba Iron Ore Limited, 2019b. Integrated Report 2018, accessed 25 February 2020, https://www.angloamericankumba.com/investors/annual-reporting/reports-archive/2018

Lechuti-Tlhalerwa, R., Coward, S., Field, M., 2019. Embracing step-changes in geoscientific information for effective implementation of geometallurgy. Journal of the South African Institute of Mining and Metallurgy 119, 355–360

Lindley, D.V., Scott, W.F., 1995. New Cambridge statistical tables. Cambridge University Press, Cambridge

Lishchuk, V., Koch, P.-H., Lund, C., Lamberg, P., 2015. The geometallurgical framework, Malmberget and Mikheevskoye case studies. Mining Science 22, 57–66

Lu, L., Pan, J., Zhu, D., 2015. Quality requirements of iron ore for iron production, in: Iron Ore Mineralogy, Processing and Environmental Sustainability, Woodhead Publishing Series in Metals and Surface Engineering. Elsevier, United Kingdom, pp. 475–504

Lund, C., Lamberg, P., 2014. Geometallurgy - a tool for better resource efficiency. European Geologist 37, 39–43

Lund, C., Lamberg, P., Lindberg, T., 2015. Development of a geometallurgical framework to quantify mineral textures for process prediction. Minerals Engineering 82, 61–77

Macfarlane, A.S., Williams, T.P., 2014. Optimizing value on a copper mine by adopting a geometallurgical solution. The Journal of the Southern African Institute of Mining and Metallurgy 114, 929–936

Maeda, T., Ono, Y., 1985. Behaviour of constituent minerals in the carbon monoxide reduction of sinter at 900 C. Iron and Steel Institute of Japan 25, 1191–1193

Manning, C.E., 1994. The solubility of quartz in H_2O in the lower crust and upper mantle. Geochemica et Cosmochimica Acta 58, 4831–4839

McKay, N., Vann, J., Ware, W., Morley, C.S., Hodkiewicz, P., 2016. Strategic versus tactical geometallurgy - a systematic process to add and sustain resource value, in: Proceedings of the International Geometallurgy Conference. Perth, Australia, pp. 15–16

McLellan, J.G., Oliver, N.H.S., Schaubs, P.M., 2004. Fluid flow in extensional environments; numerical modelling with an application to Hamersley iron ores. Journal of Structural Geology 26, 1157–1171

Menacho, J.M., 1986. Some solutions for the kinetics of combined fracture and abrasion breakage. Powder Technology 49, 87–95

Mitterlehner, J., Loeffler, G., Winter, F., Hofbauer, H., Schmid, H., Zwittag, E., Buergler, T.H., Pammer, O., Stiasny, H., 2004. Modeling and simulation of heat front propagation in the iron ore sintering process. Iron and Steel Institute of Japan International 44, 11–20

Mochón, J., Cores, A., Ruiz-Bustinza, Í., Verdeja, L.F., Robla, J.I., Garcia-Carcedo, F., 2013. Iron ore sintering part 2. Quality indices and productivity. Dyna 81, 168–177

Montoya, P.A., Keeney, L., Jahoda, R., Hunt, J., Berry, R., Drews, U., Chamberlain, V., Leichliter, S., 2011. Geometallurgical modelling techniques applicable to prefeasibility projects – La Colosa case study, in: Proceeding of the International Geometallurgy Conference. Brisbane, Australia, pp. 103–111

Moore, J.M., Tsikos, H., Polteau, S., 2001. Deconstructing the Transvaal Supergroup, South Africa: implications for Palaeoproterozoic palaeoclimate models. Journal of African Earth Sciences 33, 437–444

Morey, G.B., 1999. High-grade iron ore deposits of the Mesabi Range, Minnesota; product of a continental-scale Proterozoic ground-water flow system. Economic Geology 94, 133–142

Morris, R.C., 1985. Genesis of iron ore in banded iron-formation by supergene and supergene-metamorphic processes - a conceptual model., in: Wolf, K.H. (Ed.), Handbook of Strata-Bound and Stratiform Ore Deposits. Elsevier, Amsterdam, pp. 73–235

Mukhopadhyay, J., Gutzmer, J., Beukes, N.J., Hayashi, K.-I., 2008. Stratabound magnetite deposits from the eastern outcrop belt of the Archaean Iron Ore Group, Singhbhum craton, India. Applied Earth Science 117, 175–186

Muwanguzi, A.J.B., Karasev, A.V., Byaruhanga, J.K., Jönsson, P.G., 2012. Characterisation of the physical and metallurgical properties of natural iron ore for iron production. ISRN Materials Science 2012, 1–9

Mwanga, A., Rosenkranz, J., Lamberg, P., 2015. Testing of ore comminution behaviour in the geometallurgical context—a review. Minerals 5, 276–297

Patterson, L.W., 1995. Thermal damage of chert. Lithic Technology 20, 72–80.

Pearson, K., 1901. On lines and planes of closest fit to systems of points in space. The London, Edinburgh, and Dublin Philosophical Magazine and Journal of Science 2, 559–572

Pienaar, D., Guy, B.M., Pienaar, C., Viljoen, K.S., 2017. A geometallurgical characterization study of the Crystalkop Reef at the Great Noligwa Mine, Klerksdorp Goldfield, South Africa. South African Journal of Geology 120, 303–322

Purdy, B.A., 1974. Investigations concerning the thermal alteration of silica minerals: an archaeological approach. Tebiwa 17, 37–66

Rencher, A., C., Christensen, W., F., 2012. Chapter 10, Multivariate regression - Section 10.1, Introduction., in: Methods of Multivariate Analysis, Wiley Series in Probability and Statistics. John Wiley & Sons, p. 19

Rio Tinto, 2019. Annual Report 2018, accessed 25 February 2020, https://www.riotinto.com/invest/reports/annual-report

Rosíere, C.A., Spier, C.A., Rios, F.J., 2008. The itabirites of the Quadrilátero Ferrífero and related high-grade iron ore deposits: an overview. Reviews in Economic Geology 15, 223–254

Ruan, H.D., Gilkes, R.J. 1995. Dehydroxylation of aluminous goethite: unit cell dimensions, crystal size and surface area. Clays and Clay Minerals 43, 196–211

Rutter, E.H., Holdsworth, R.E., Knipe, R.J., 2001. The nature and tectonic significance of fault-zone weakening: an introduction. Geological Society, London, Special Publications 186, 1–11

Schouwstra, R., Vaux, D.D., Muzondo, T., Prins, C., 2013. A geometallurgical approach at Anglo American Platinum's Mogalakwena operation. Presented at the Second Australasian Institute of Mining and Metallurgy International Geometallurgy Conference, Brisbane, Australia, pp. 85–92

Schouwstra, R.P., Smit, A.J., 2011. Developments in mineralogical techniques – what about mineralogists? Minerals Engineering 24, 1224–1228

Schwertman, N.C., Owens, M.A., Adnan, R., 2004. A simple more general boxplot method for identifying outliers. Computational Statistics & Data Analysis 47, 165–174

Sepulveda, E., Dowd, P.A., Xu, C., Addo, E., 2017. Multivariate modelling of geometallurgical variables by projection pursuit. Mathematical Geosciences 49, 121–143

Shi, F., Kojovic, T., Larbi-Bram, S., Manlapig, E., 2009. Development of a rapid particle breakage characterisation device - The JKRBT. Minerals Engineering 22, 602–612

Simons, E.N., Gregory, E., 1940. Steel Manufacture, Simply Explained. Sir Isaac Pitman & Sons, London, pp205

Smith, A.J.B., Beukes, N.J., 2016. Paleoproterozoic banded iron formation-hosted high grade hematite iron ore deposits of Transvaal Supergroup, South Africa. Episodes 39, 269

Taylor, D., Dalstra, H.J., Harding, A.E., Broadbent, G.C., Barley, M.E., 2001. Genesis of high-grade hematite orebodies of the Hamersley Province, Western Australia. Economic Geology 96, 837–873

Teo, C.S., Waters, A.G., Nicol, S.K., 1990. Quantification of the breakage of lump materials during handling operations. International Journal of Mineral Processing 30, 159–184

Thorne, W., Hagemann, S., Webb, A., Clout, J., 2008. Banded iron formation-related iron ore deposits of the Hamersley Province, Western Australia, in: Hagemann, S., Rosiere, C., Gutzmer, J., Beukes, N. (Eds.), Banded Iron Formation-Related High-Grade Iron Ore, Reviews in Economic Geology. Society of Economic Geologists, Littleton, Colorado, USA, pp. 197–221

Thorne, W.S., Hagemann, S.G., Barley, M., 2004. Petrographic and geochemical evidence for hydrothermal evolution of the North Deposit, Mt Tom Price, Western Australia. Miner Deposita 39, 766–783

Trendall, A.F., De Laeter, J.R., Nelson, D.R., 1995. Chronology of Gondwana BIFs: progress report from recent zircon U-Pb analysis. Presented at the Third Australian Conference on Geochronology, pp. 1–3

Urban, H., Stribrny, B., Lippolt, H.J., 1992. Iron and manganese deposits of the Urucum District, Mato Grosso do Sul, Brazil. Economic Geology 87, 1375–1392

Vale, 2019. Annual report pursuant to section 13 or 15(d) of the securities exchange act of 1934 for the fiscal year ended: December 31 2018, accessed 25 February 2020, http://www.vale.com/EN/investors/information-market/annual-reports/20f/Pages/default.aspx

van der Vyver, W.F., Pistorius, P.C., Brand, S.A., Reid, M., 2009. Disintegration of Northern Cape iron ores under reducing conditions. Ironmaking & Steelmaking 36, 354–362

Van Wyk, J.P., 1980. Die geologie van die Roinekke-Matsap-Wolhaarkop in Noord-Kaapland met spesiale verwysing na die Koegas Subgroep en die Transvaal Supergroep. (M.Sc. Dissertation (unpubl.)). Randse Afrikaans University, Johannesburg, South Africa

Visser, J.N.J., 1971. The deposition of the Griquatown glacial member in the Transvaal Supergroup. South African Journal of Geology 74, 187–199

Vos, C.F., Stange, W., Bradshaw, D.J., 2014. A new small-scale test to determine flotation performance - Part 1: Overall performance. Minerals Engineering 66, 62–67

Williams, S.R., 2013. A historical perspective of the application and success of geometallurgical methodologies. Proceedings of the International Geometallurgy Conference, Brisbane, Australia 30

Wold, S., Esbensen, K., Geladi, P., 1987. Principal component analysis. Chemometrics and Intelligent Laboratory Systems 2, 37–52

Wolska, E., Szajda, W., 1985. Structural and spectroscopic characteristics of synthetic hydrohaematite. Journal of Materials Science 20, 4407–4412

World Steel Association, 2018. World Steel Figures in 2018. Accessed 9 March 2019, https://www.worldsteel.org/steel-by-topic/statistics/steel-statistical-yearbook.html

Wu, S., Liu, X., Wu, J., 2015. Reduction disintegration behaviour of lump ore in COREX shaft furnace. Iron and Steel Institute of Japan International 55, 1608–1616

Wu, S.-L., Xu, H.-F., Tian, Y.-Q., 2009. Evaluation of lump ores for use in modern blast furnaces as part of mixed burden practice. Ironmaking & Steelmaking 36, 19–23

Yildirim, B.G., Bradshaw, D., Powell, M., Evans, C., Clark, A., 2014. Development of an effective and practical Process Alteration Index (PAI) for predicting metallurgical responses of Cu porphyries. Minerals Engineering 69, 91–96

Yuan, M., Ekici, A., Lu, Z., Monteiro, R., 2007. Dimension reduction and coefficient estimation in multivariate linear regression. Journal of the Royal Statistical Society 69, 329–346

Appendix A: Chemistry, geology and physical/metallurgical properties of composites

Sample ID	Lithology	Competency	Min	Vugs	Fe %	SiO_2 %	Al_2O_3 %	K_2O %	P%	S%	LOI %	Fe_2O_3 %	FeO %	Moisture%	UCS (MPa)	Bulk RD (g/cm^3)	AI%	TI%	RI%	RDI %	DI %
MCOMPDIAMOND000186	HEM MAS	BKN	SPC	Minor	66.2	2.7	1.32	0.20	0.054	0.008	0.700	94.30	-	-	-	-	12.61	82.33	-	1.29	0.05
MCOMPDIAMOND000188	HEM MAS	TDI, minor BKN	SPC	None	64.8	3.9	1.17	0.33	0.034	0.031	0.680	92.30	0.35	0.26	-	-	-	-	-	7.16	-
MCOMPDIAMOND000189	HEM MAS	BKN	None	Low	65.7	2.8	1.34	0.22	0.022	0.031	0.700	93.60	0.30	-	-	-	6.19	90.37	-	2.15	0.08
MCOMPDIAMOND000204	HEM MAS	BKN, minor CPT	None	None	65.9	2.8	1.49	0.32	0.032	0.049	0.640	93.80	0.39	0.08	-	-	8.68	87.67	19.77	1.36	0.06
MCOMPDIAMOND000205	HEM MAS (LAM)	CPT, BKN	None	Moderate	66.1	3.1	1.19	0.20	0.059	0.019	0.580	94.20	0.33	0.10	-	-	12.78	82.57	15.19	1.08	0.07
MCOMPDIAMOND000206	HEM MAS (LAM)	CPT, BKN	None	Low	66.3	2.3	1.25	0.29	0.060	0.013	0.540	94.40	0.35	0.08	-	-	8.72	86.99	26.19	5.85	0.10
MCOMPDIAMOND000207	HEM MAS	BKN, minor TDI	SPC	None	66.8	1.6	1.07	0.16	0.022	0.093	0.680	95.30	0.24	0.08	-	-	12.47	82.32	21.15	5.81	0.10
MCOMPDIAMOND000208	HEM MAS	TDI, minor BKN	SPC	Minor	67.8	1.6	0.64	0.03	0.076	0.012	0.620	96.60	0.32	0.02	-	-	16.91	75.77	19.12	3.21	0.07
MCOMPDIAMOND000209	HEM MAS	CPT, BKN	Half SPC	Minor	66.2	2.8	1.36	0.10	0.056	0.006	0.780	94.30	0.35	0.10	-	4.79	14.07	78.99	15.51	4.53	0.06
MCOMPDIAMOND000210	HEM LAM (MAS)	CPT, minor BKN	SPC	None	67.4	1.8	0.81	0.05	0.077	0.003	0.540	96.10	0.29	0.06	-	4.81	5.63	90.77	36.60	5.09	0.09
MCOMPDIAMOND000211	HEM LAM, minor	BKN	SPC	None	65.6	4.5	0.45	0.03	0.052	0.003	0.460	93.40	0.38	0.10	-	-	5.53	91.14	40.14	9.75	0.10

	HEM MAS																				
MCOMPDIAMOND000212	HEM MAS	CPT, BKN	Half SPC	None	65.5	2.4	1.56	0.22	0.042	0.025	0.940	93.20	0.44	0.24	-	4.63	13.95	79.38	17.46	1.69	0.09
MCOMPDIAMOND000235	HEM MAS	CPT, minor BKN	None	None	65.1	2.7	1.26	0.16	0.020	0.012	1.140	92.80	0.29	0.06	-	3.99	6.94	89.03	22.06	2.13	0.09
MCOMPDIAMOND000236	HEM MAS	CPT, BKN	None	None	64.7	3.8	1.72	0.50	0.022	0.030	0.660	92.10	0.38	0.10	-	4.72	10.92	85.20	19.63	1.03	0.06
MCOMPDIAMOND000239	HEM LAM	CPT	SPC	None	66.9	1.3	0.59	0.03	0.042	0.218	0.660	95.30	0.35	0.38	-	5.16	13.62	80.63	21.94	1.47	0.11
MCOMPDIAMOND000254	HEM MAS, minor HEM LAM	CPT	None	None	68.1	1.2	0.22	0.02	0.079	0.006	0.640	96.90	0.39	0.04	-	4.93	11.04	84.25	21.66	2.02	0.06
MCOMPDIAMOND000270	HEM LAM (MAS)	BKN	Low CAL	Minor	65.8	3.6	1.33	0.21	0.028	0.011	0.785	94.01	2.73	-	-	-	6.10	91.30	31.82	1.64	-
MCOMPDIAMOND000271	HEM LAM (MAS)	BKN	Low SPC	None	66.3	2.5	0.97	0.13	0.020	0.170	0.535	93.40	2.81	-	-	-	7.42	90.73	31.33	1.53	-
MCOMPDIAMOND000272	HEM LAM (MAS)	BKN	Minor SPC	None	67.0	2.0	0.95	0.13	0.026	0.032	0.500	95.94	0.30	-	-	-	7.22	90.82	-	1.82	-
MCOMPDIAMOND000273	HEM LAM (MAS)	CPT	None	Minor	66.3	5.5	1.45	0.21	0.020	0.077	0.525	90.92	0.63	-	-	-	8.31	88.29	30.17	7.70	0.33
MCOMPDIAMOND000274	HEM LAM (MAS)	CPT	None	Moderate	63.5	5.6	0.90	0.14	0.031	0.105	0.900	90.49	0.26	0.14	65.7	-	7.95	88.48	34.29	7.19	0.98
MCOMPDIAMOND000275	HEM LAM (MAS)	CPT, BKN	None	None	65.6	3.5	1.43	0.28	0.026	0.008	0.615	93.59	1.84	-	-	-	6.70	91.04	35.65	1.92	0.46
MCOMPDIAMOND000276	HEM LAM (MAS)	CPT	Minor SPC	None	65.8	2.9	1.64	0.32	0.050	0.054	0.675	93.45	0.94	-	-	-	11.84	84.30	38.54	2.11	0.07

MCOMPDIAMOND000299	HEM MAS	BKN	Minor SPC	None	66.5	2.0	1.11	0.09	0.041	0.032	0.010	96.28	0.95	-	-	-	19.77	73.81	18.24	2.62	0.04
MCOMPDIAMOND000300	HEM LAM (MAS)	CPT	Minor SPC	None	66.1	2.2	1.40	0.14	0.019	0.124	0.013	95.26	0.56	-	115.2	-	20.78	74.97	39.61	17.32	0.07
MCOMPDIAMOND000301	HEM LAM (MAS)	BKN	Minor SPC	Minor	66.0	2.4	1.48	0.10	0.035	0.090	0.014	95.12	0.11	-	-	4.65	12.92	82.63	36.56	6.94	0.05
MCOMPDIAMOND000304	HEM LAM (MAS)	CPT, BKN	Low SPC	None	67.4	1.6	0.59	0.03	0.043	0.068	0.102	97.01	0.25	-	-	-	11.63	82.75	26.48	2.81	0.05
MCOMPDIAMOND000305	HEM MAS	BKN	Minor SPC	Minor	67.0	1.7	1.05	0.14	0.023	0.009	0.014	96.10	0.22	-	-	4.78	8.16	87.71	20.77	1.90	0.12
MCOMPDIAMOND000312	HEM MAS	BKN	Minor SPC	Low	67.4	1.4	1.01	0.11	0.020	0.100	0.013	97.49	0.34	-	-	4.81	13.95	80.24	25.21	9.93	0.18
MCOMPDIAMOND000313	HEM MAS	CPT, BKN	Low	None	63.7	4.0	3.13	0.45	0.026	0.005	0.023	91.07	0.56	-	-	4.91	11.46	84.01	29.33	1.94	0.39
MCOMPDIAMOND000317	HEM MAS	CPT	Minor SPC	Low	67.1	2.0	1.08	0.12	0.033	0.022	0.015	96.33	0.53	-	-	4.79	9.15	85.71	16.33	0.87	0.29

Abbreviations used in table:

HEM	hematite
LAM	laminated
MAS	massive
BKN	broken
CPT	competent
TDi	totally disintegrated
SPC	specularite
( )	secondary texture

Appendix B: Locations of samples containing test results for (a) AI, (b) TI, (c) RI, (d) RDI, (e) DI

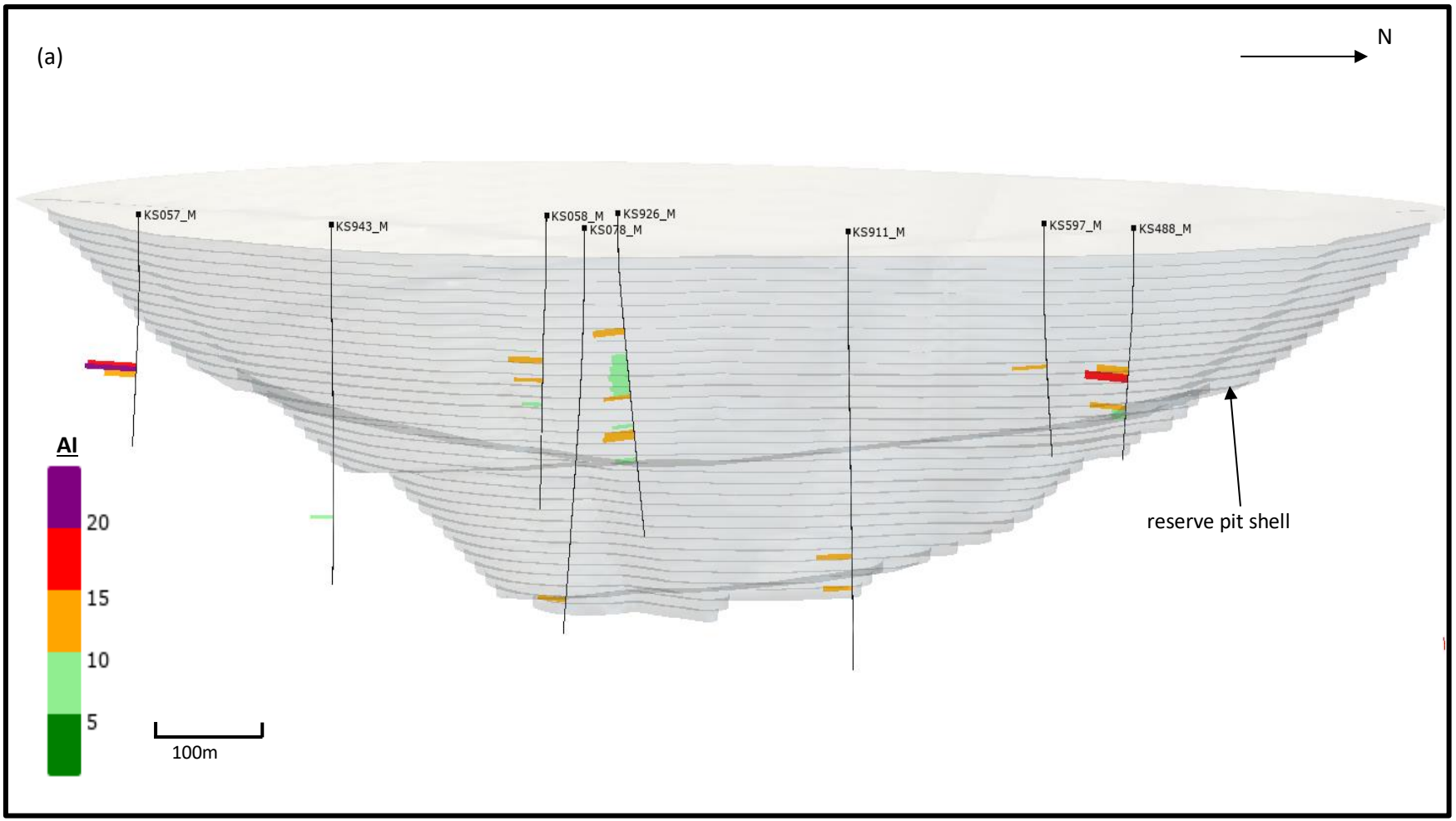

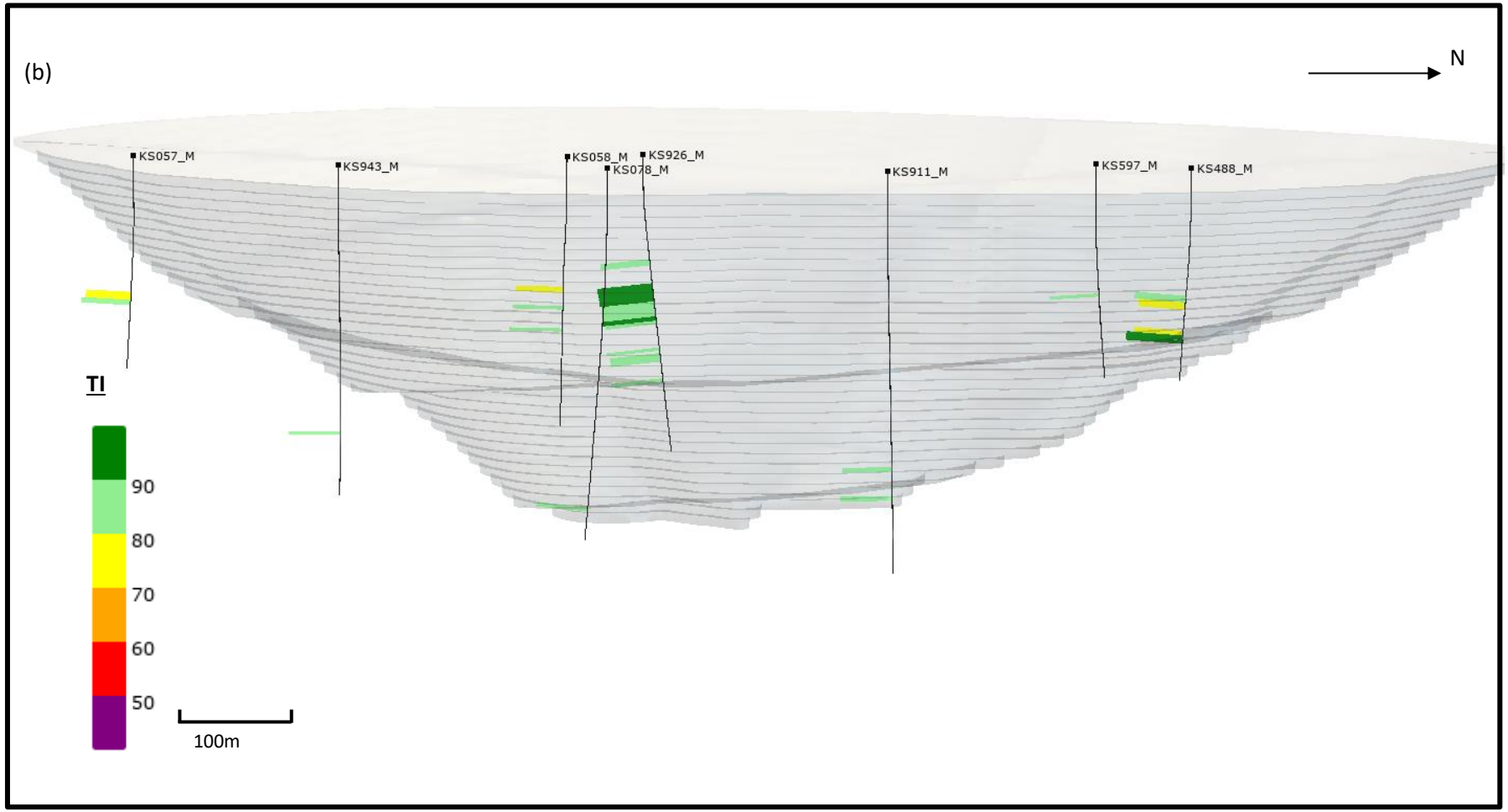
(b)
N
KS057_M
KS943_M
KS058_M
KS926_M
KS078_M
KS911_M
KS597_M
KS488_M
TI
90
80
70
60
50
100m

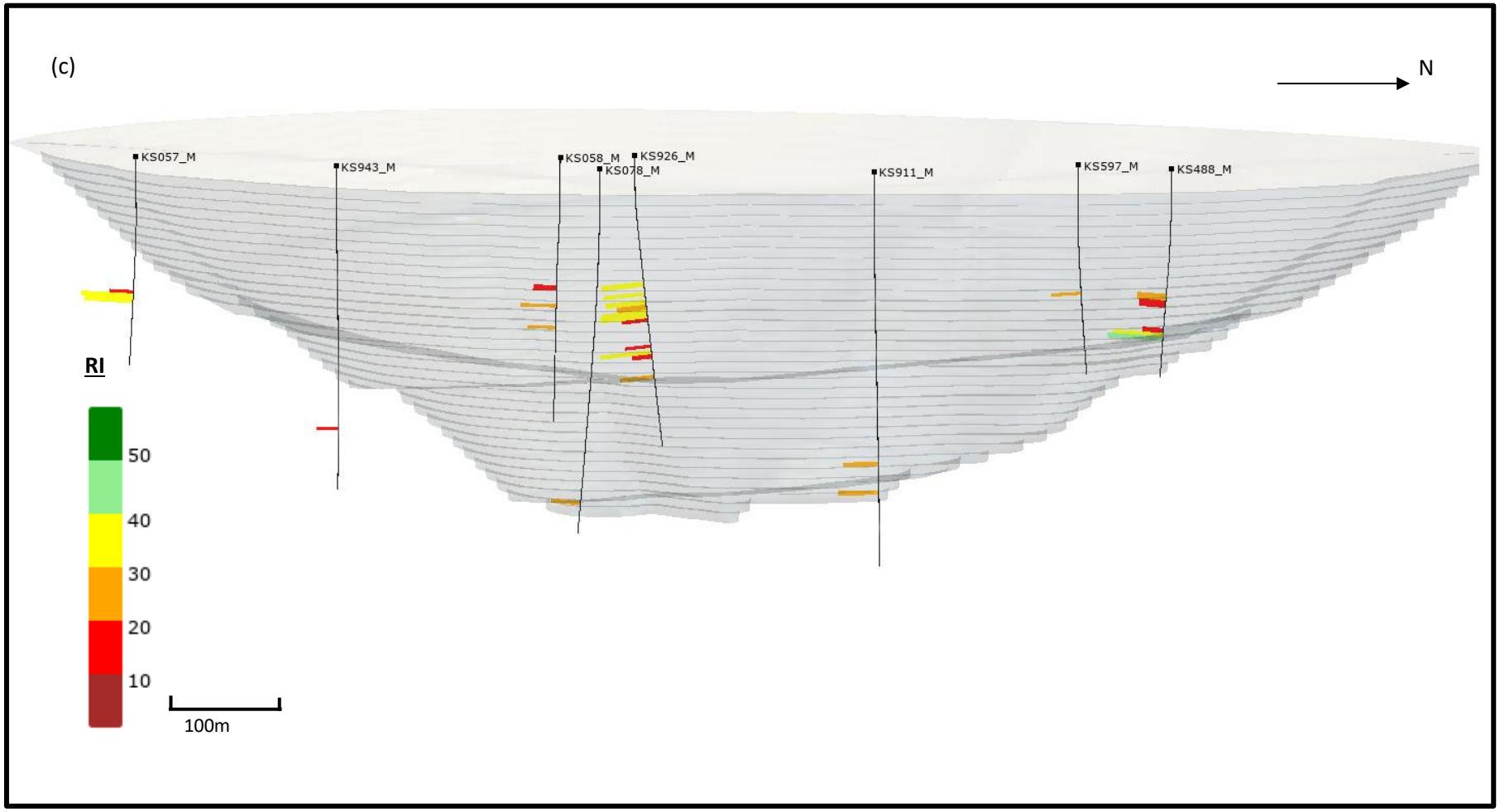
(c)
N
KS057_M
KS943_M
KS058_M
KS926_M
KS078_M
KS911_M
KS597_M
KS488_M
RI
50
40
30
20
10
100m

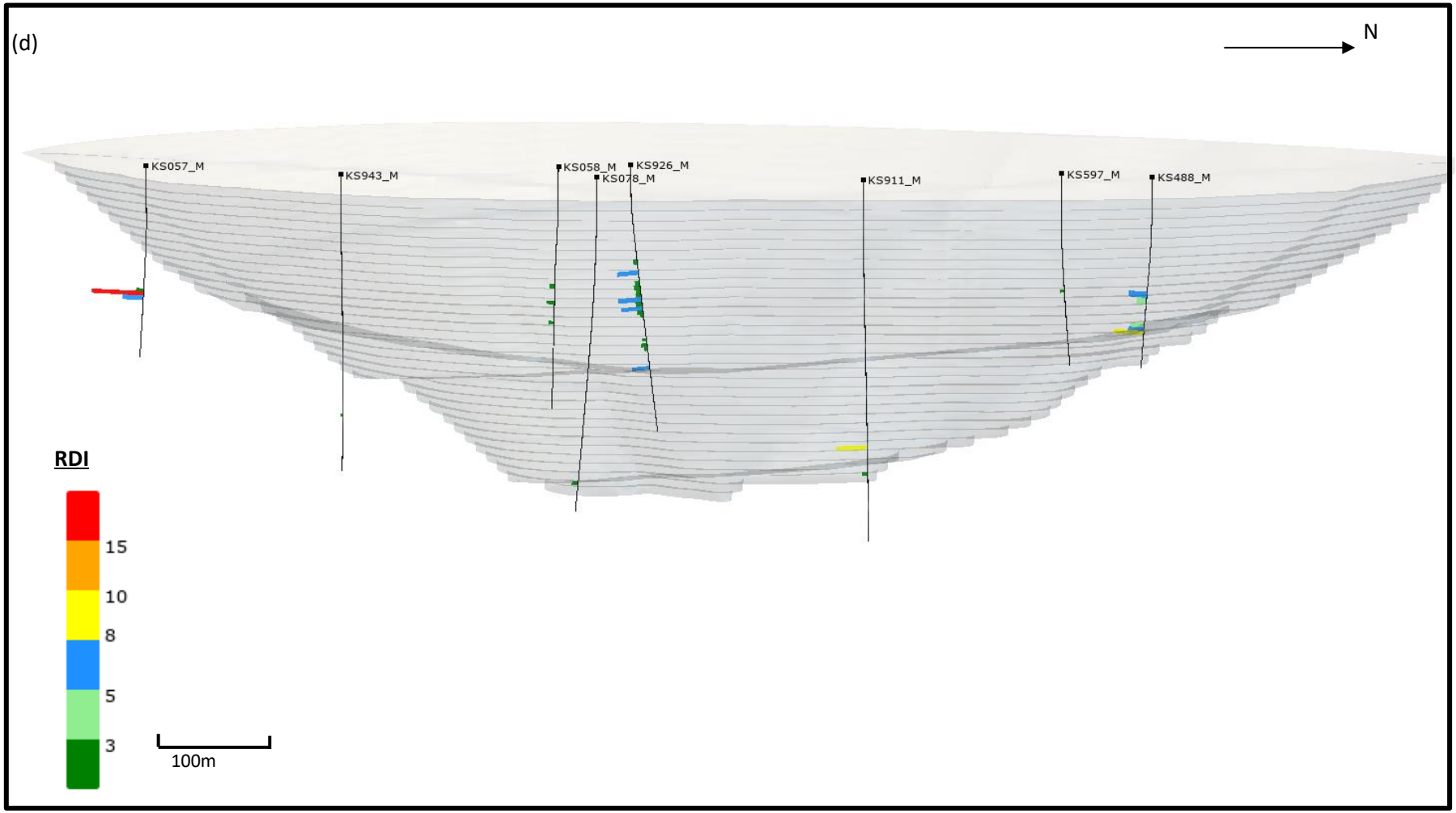
(d)
N
KS057_M
KS943_M
KS058_M
KS926_M
KS078_M
KS911_M
KS597_M
KS488_M
RDI
15
10
8
5
3
100m

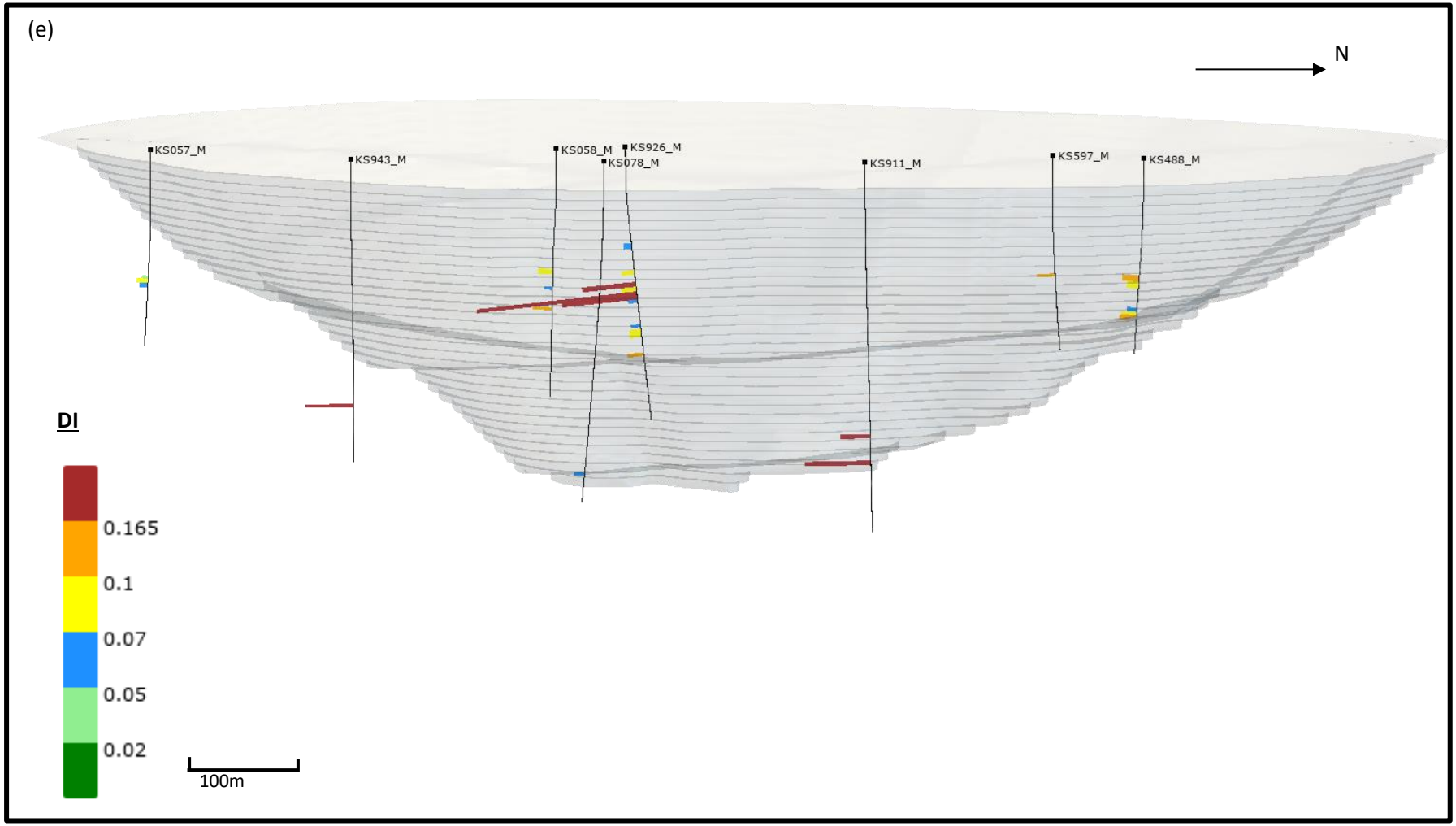
(e)
N
KS057_M
KS943_M
KS058_M
KS926_M
KS078_M
KS911_M
KS597_M
KS488_M
DI
0.165
0.1
0.07
0.05
0.02
100m

Appendix C: Percentage Points of the Normal Distribution (Lindley and Scott, 1995)

This table gives percentage points $x(P)$ defined by the equation

$$\frac{P}{100} = \frac{1}{\sqrt{2\pi}} \int_{x(P)}^{\infty} e^{-\frac{1}{2}t^2}\, dt.$$

If X is a variable, normally distributed with zero mean and unit variance, $P/100$ is the probability that $X \geqslant x(P)$. The lower P per cent points are given by symmetry as $-x(P)$, and the probability that $|X| \geqslant x(P)$ is $2P/100$.

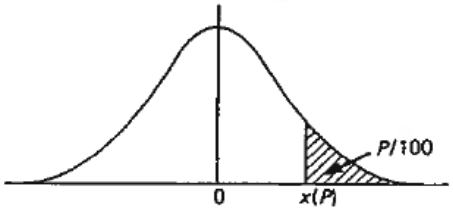

P	$x(P)$	P	$x(P)$	P	$x(P)$	P	$x(P)$	P	$x(P)$	P	$x(P)$
50	0·0000	5·0	1·6449	3·0	1·8808	2·0	2·0537	1·0	2·3263	0·10	3·0902
45	0·1257	4·8	1·6646	2·9	1·8957	1·9	2·0749	0·9	2·3656	0·09	3·1214
40	0·2533	4·6	1·6849	2·8	1·9110	1·8	2·0969	0·8	2·4089	0·08	3·1559
35	0·3853	4·4	1·7060	2·7	1·9268	1·7	2·1201	0·7	2·4573	0·07	3·1947
30	0·5244	4·2	1·7279	2·6	1·9431	1·6	2·1444	0·6	2·5121	0·06	3·2389
25	0·6745	4·0	1·7507	2·5	1·9600	1·5	2·1701	0·5	2·5758	0·05	3·2905
20	0·8416	3·8	1·7744	2·4	1·9774	1·4	2·1973	0·4	2·6521	0·01	3·7190
15	1·0364	3·6	1·7991	2·3	1·9954	1·3	2·2262	0·3	2·7478	0·005	3·8906
10	1·2816	3·4	1·8250	2·2	2·0141	1·2	2·2571	0·2	2·8782	0·001	4·2649
5	1·6449	3·2	1·8522	2·1	2·0335	1·1	2·2904	0·1	3·0902	0·0005	4·4172

Appendix D: Scatter plots of physical and metallurgical properties versus chemical assay data

Abrasion Index*

*Totally disintegrated samples are not plotted due to insufficient data

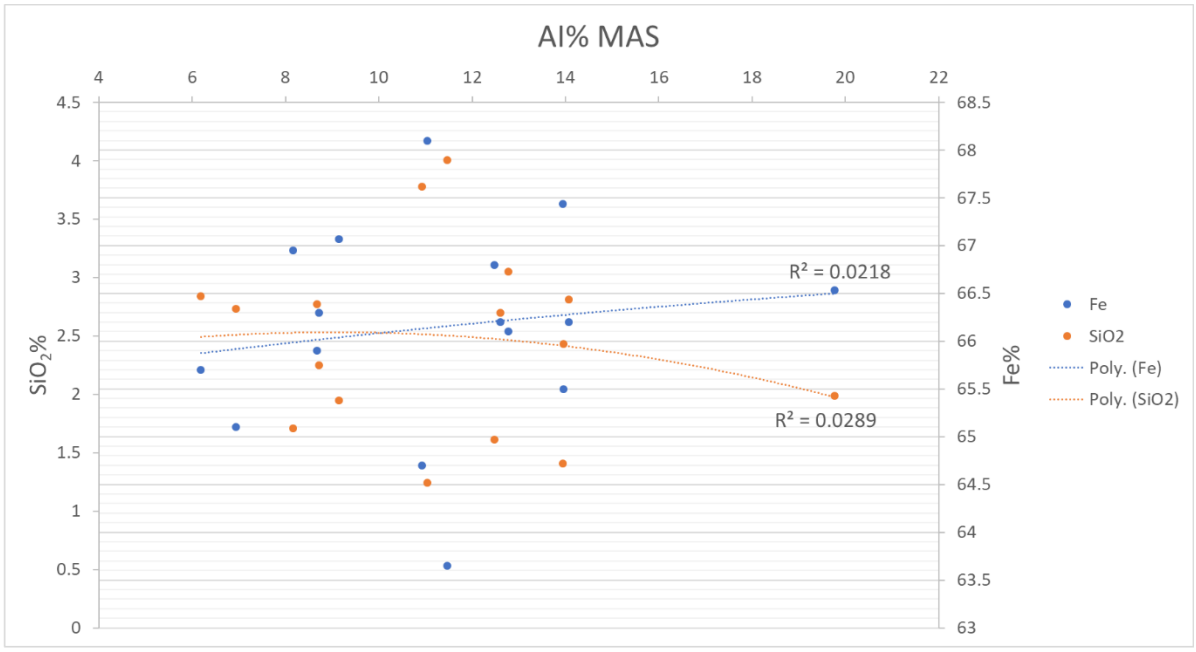

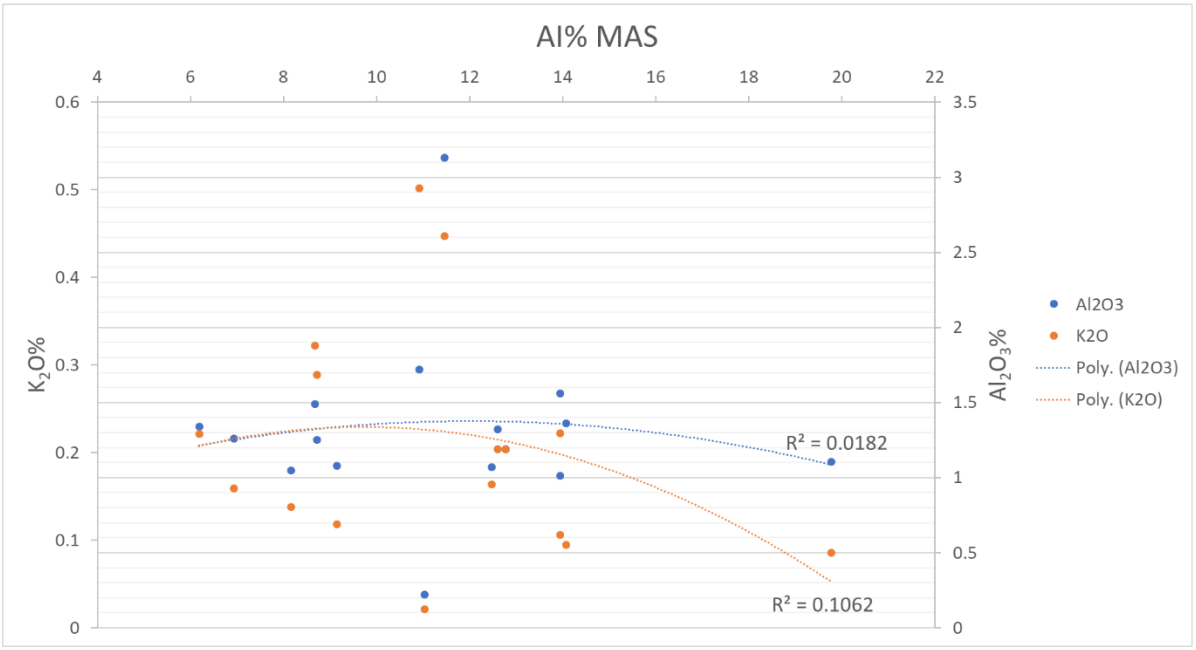

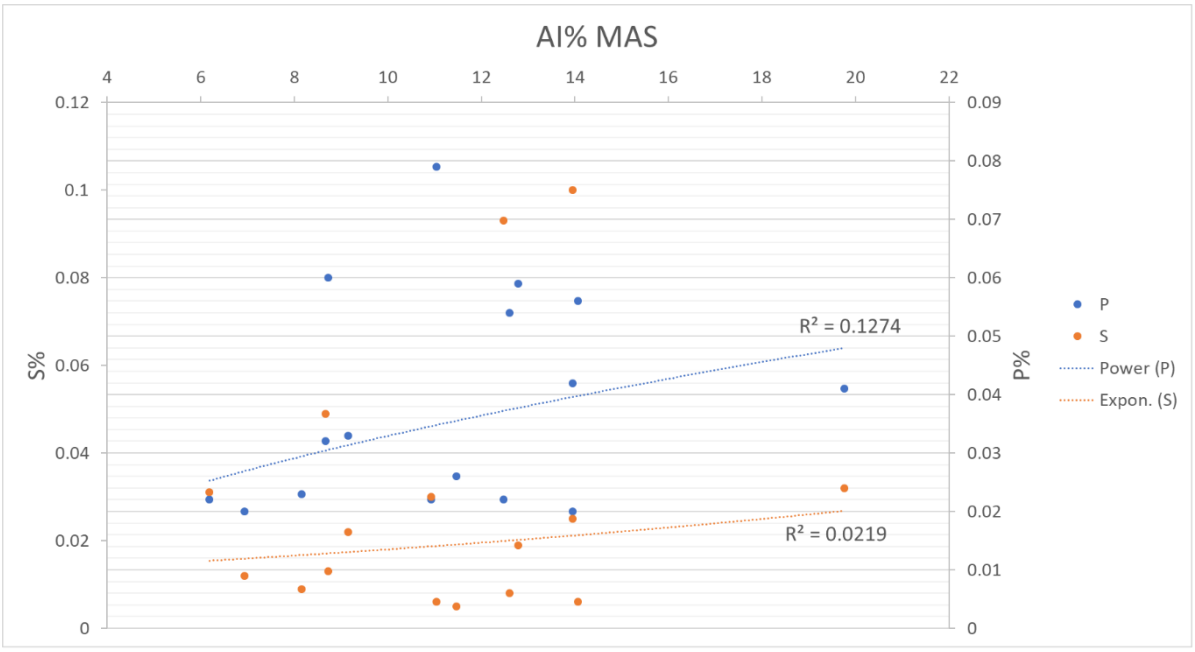
Al% MAS
S%
P%
R² = 0.1274
R² = 0.0219
P
S
Power (P)
Expon. (S)

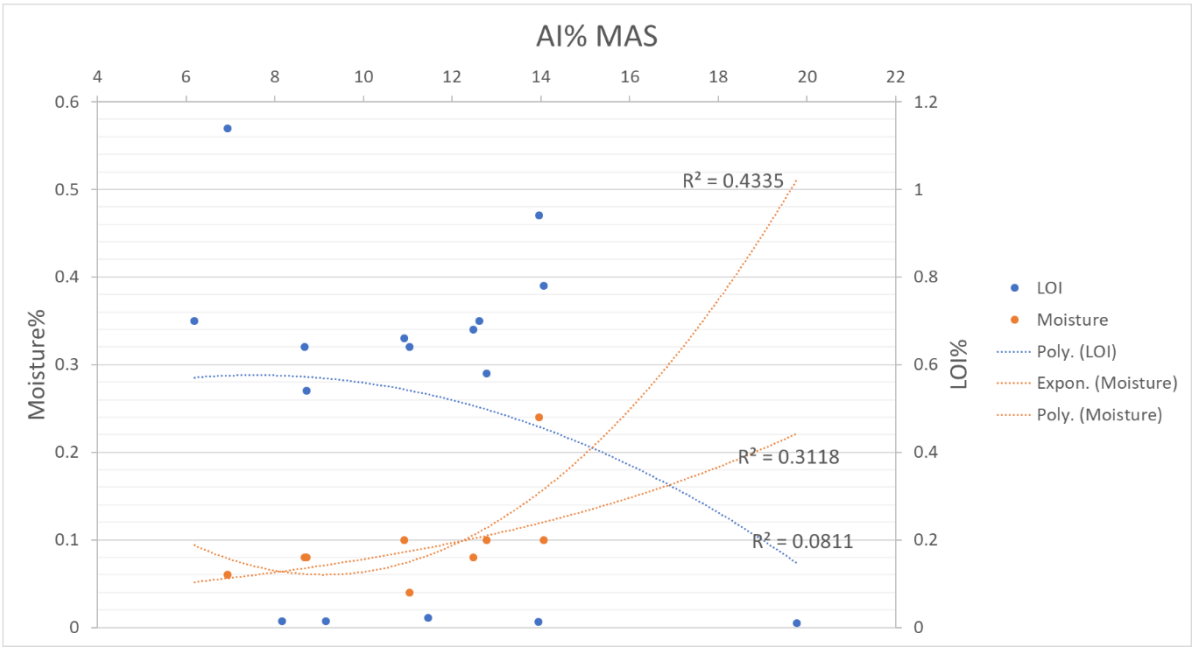
Al% MAS
Moisture%
LOI%
R² = 0.4335
R² = 0.3118
R² = 0.0811
LOI
Moisture
Poly. (LOI)
Expon. (Moisture)
Poly. (Moisture)

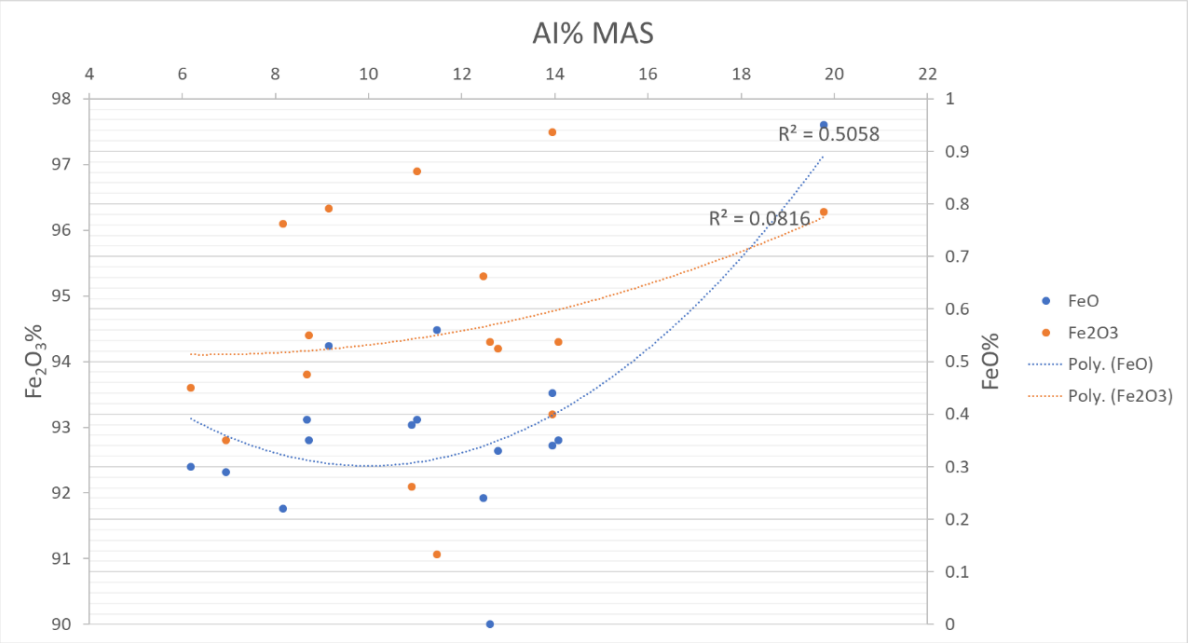
AI% MAS
4
6
8
10
12
14
16
18
20
22
98
97
96
95
94
93
92
91
90
1
0.9
0.8
0.7
0.6
0.5
0.4
0.3
0.2
0.1
0
R² = 0.5058
R² = 0.0816
Fe2O3%
FeO%
FeO
Fe2O3
Poly. (FeO)
Poly. (Fe2O3)

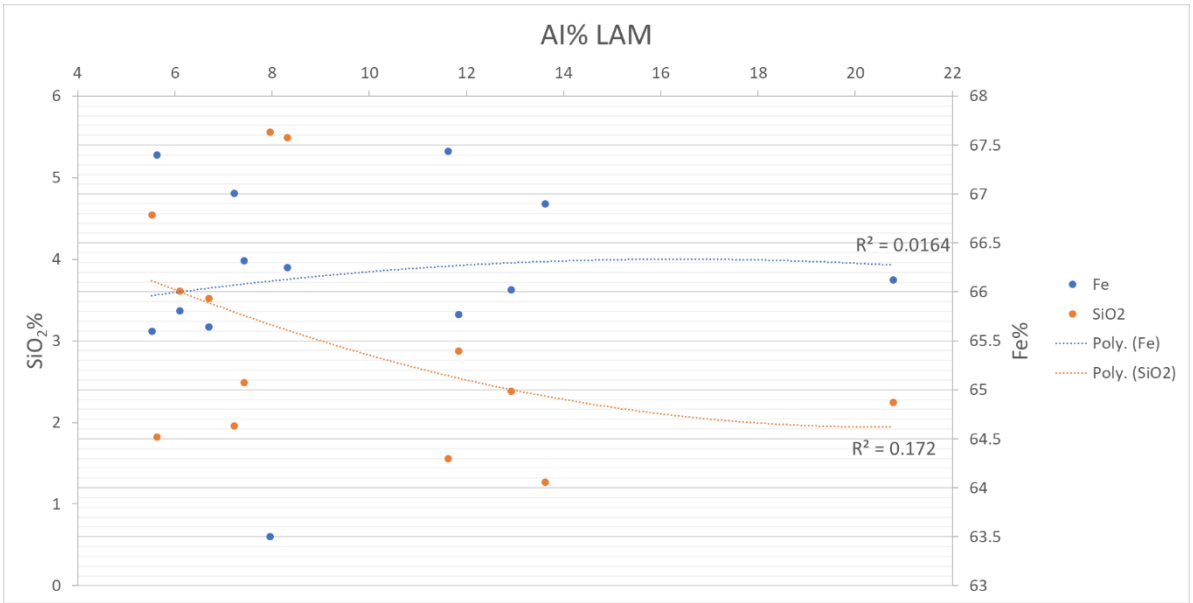
AI% LAM
4
6
8
10
12
14
16
18
20
22
6
5
4
3
2
1
0
68
67.5
67
66.5
66
65.5
65
64.5
64
63.5
63
R² = 0.0164
R² = 0.172
SiO2%
Fe%
Fe
SiO2
Poly. (Fe)
Poly. (SiO2)

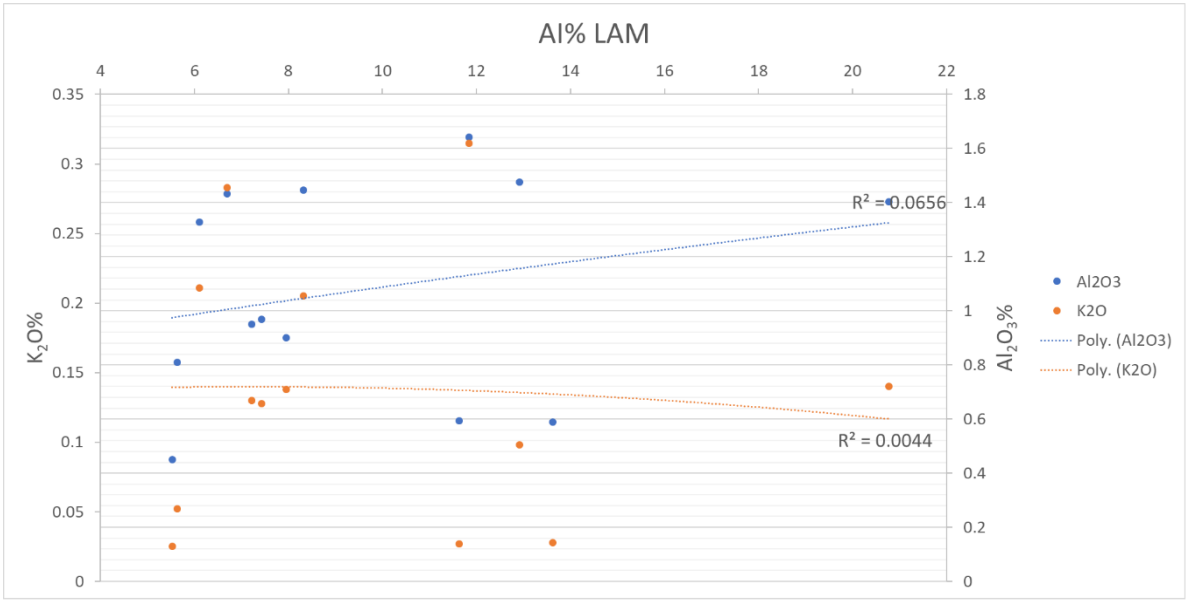
Al% LAM
4
6
8
10
12
14
16
18
20
22
0.35
0.3
0.25
0.2
0.15
0.1
0.05
0
1.8
1.6
1.4
1.2
1
0.8
0.6
0.4
0.2
0
R² = 0.0656
R² = 0.0044
K2O%
Al2O3%
Al2O3
K2O
Poly. (Al2O3)
Poly. (K2O)

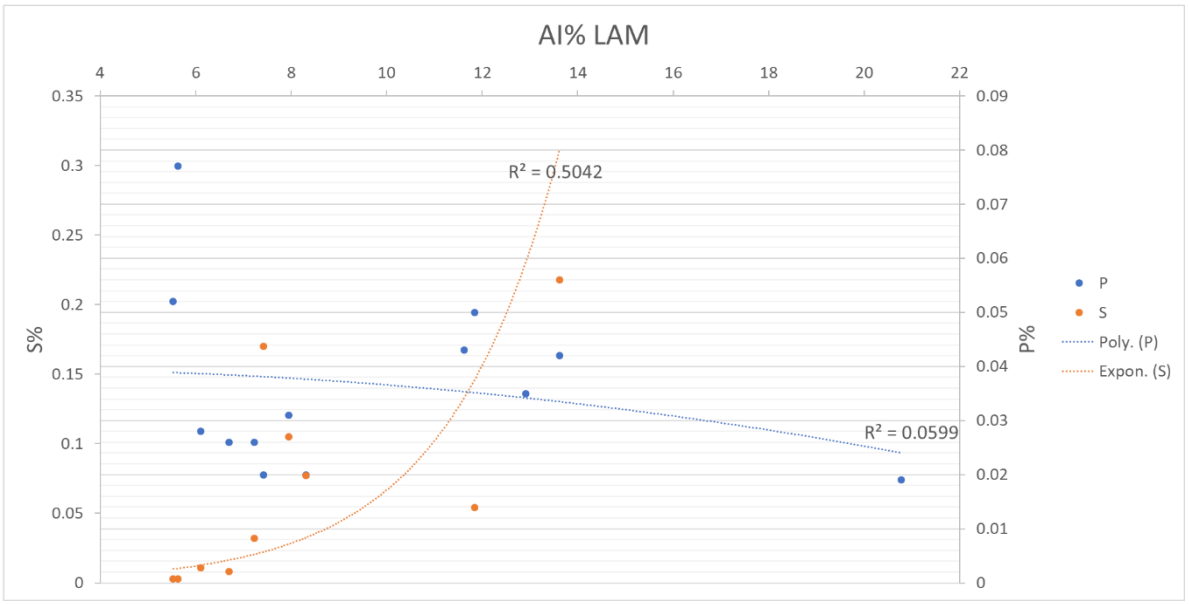
Al% LAM
4
6
8
10
12
14
16
18
20
22
0.35
0.3
0.25
0.2
0.15
0.1
0.05
0
0.09
0.08
0.07
0.06
0.05
0.04
0.03
0.02
0.01
0
R² = 0.5042
R² = 0.0599
S%
P%
P
S
Poly. (P)
Expon. (S)

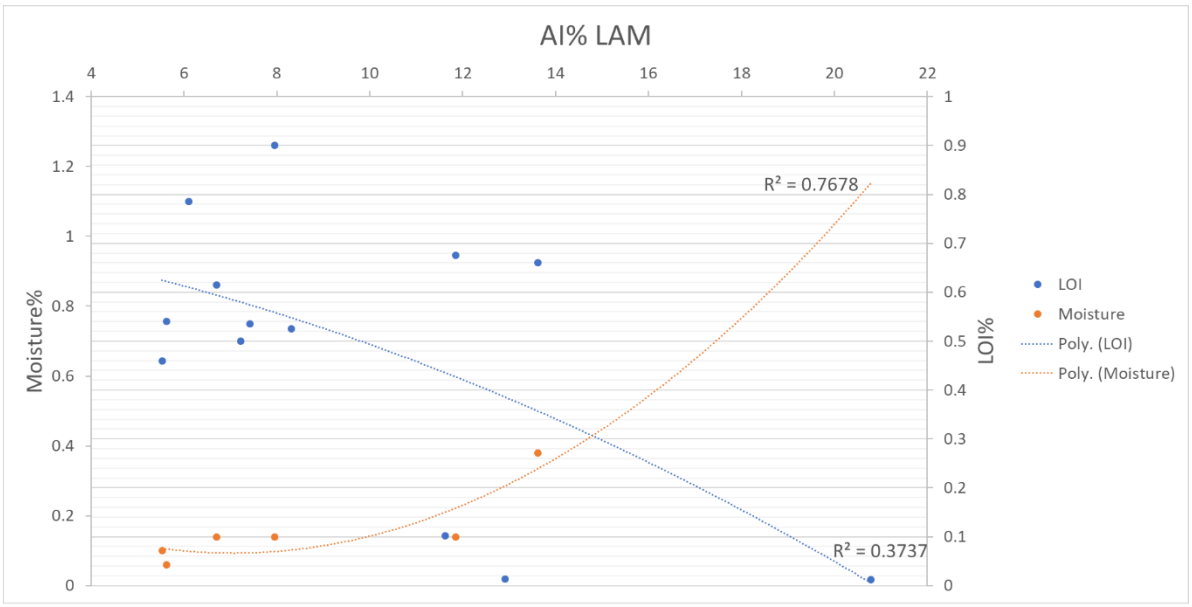
Al% LAM
Moisture%
LOI%
R² = 0.7678
R² = 0.3737
LOI
Moisture
Poly. (LOI)
Poly. (Moisture)

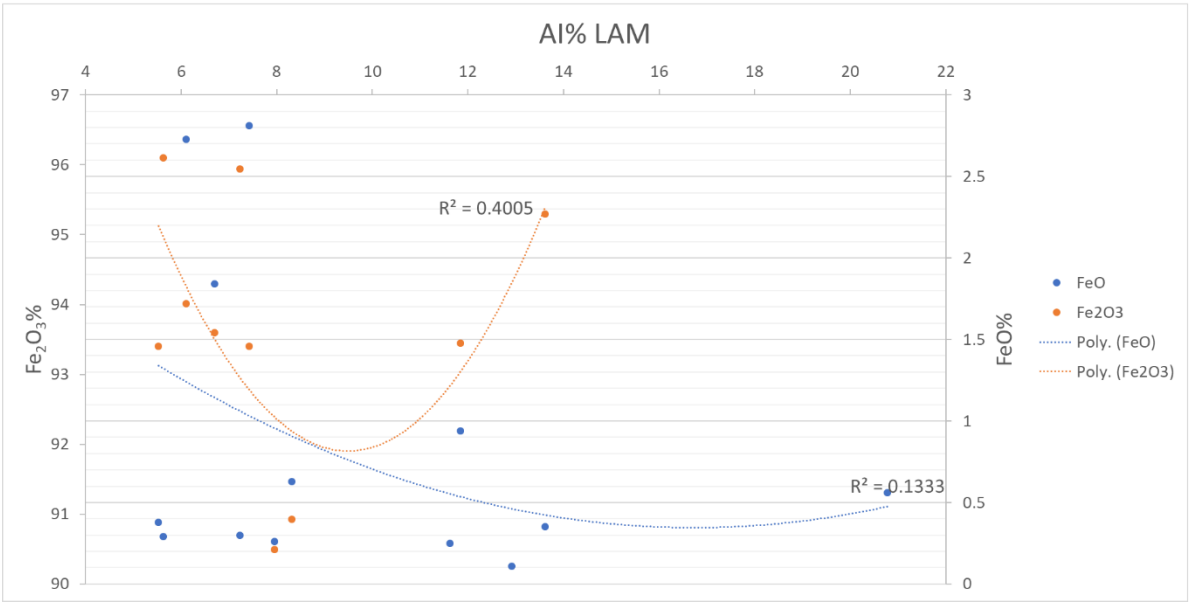
Al% LAM
Fe2O3%
FeO%
R² = 0.4005
R² = 0.1333
FeO
Fe2O3
Poly. (FeO)
Poly. (Fe2O3)

Tumble Index*

*Totally disintegrated samples are not plotted due to insufficient data

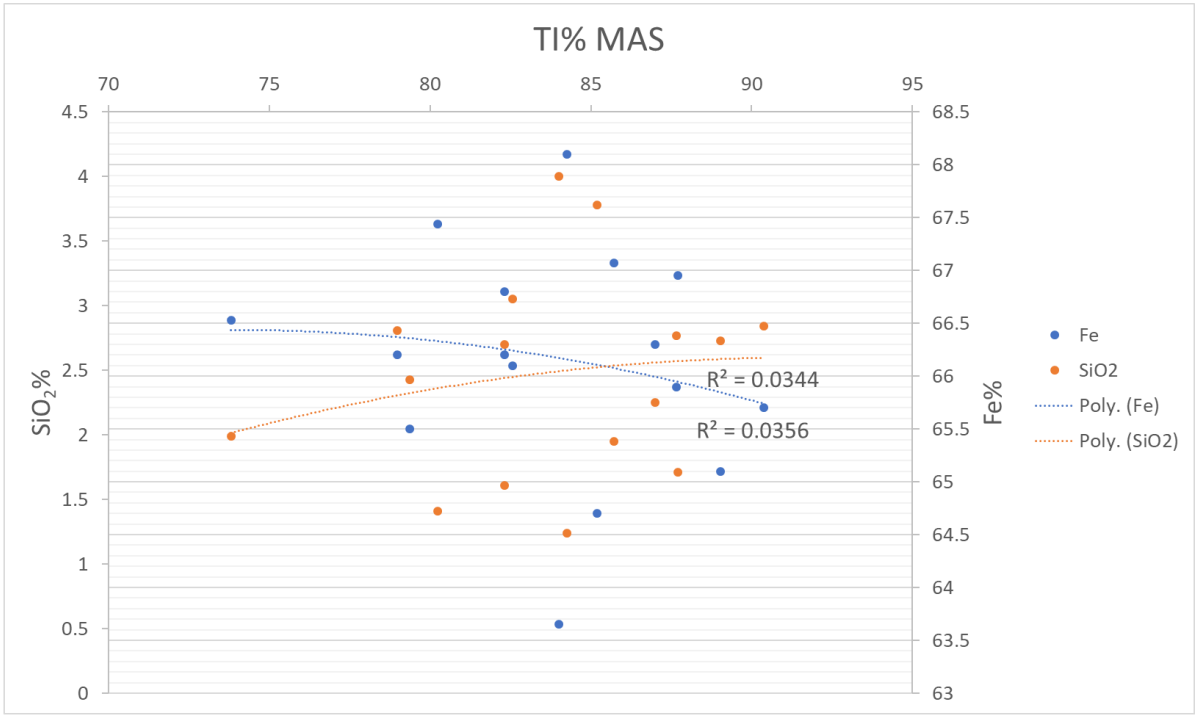

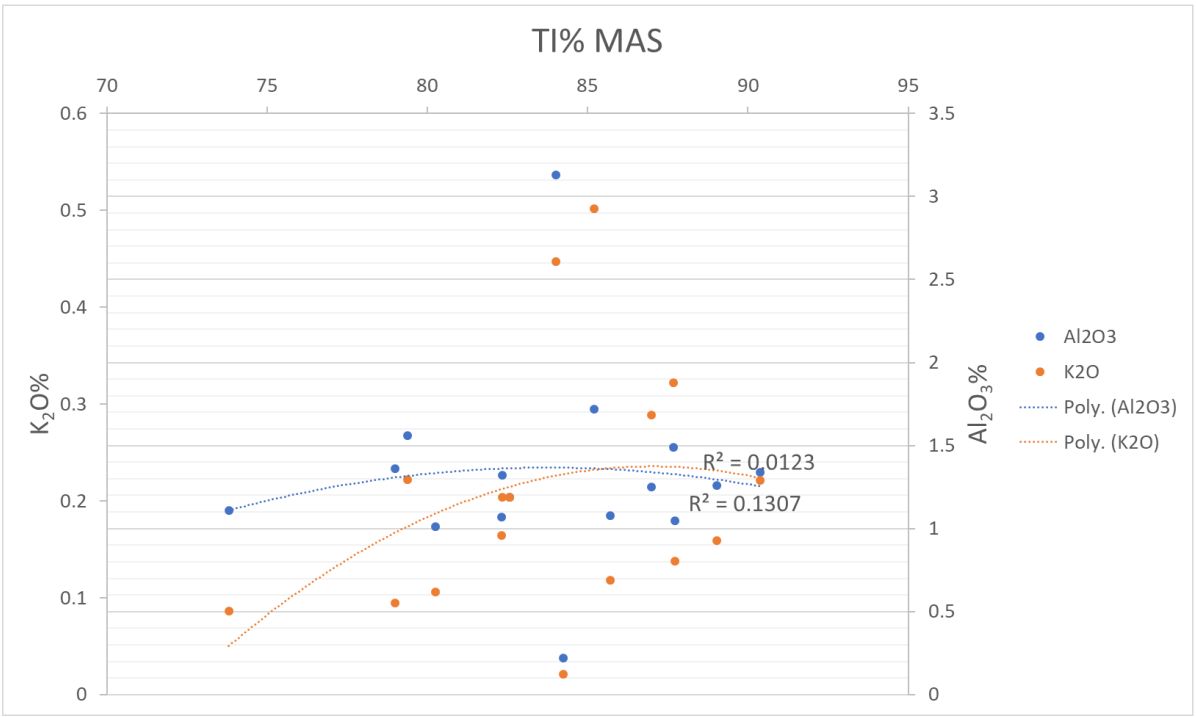

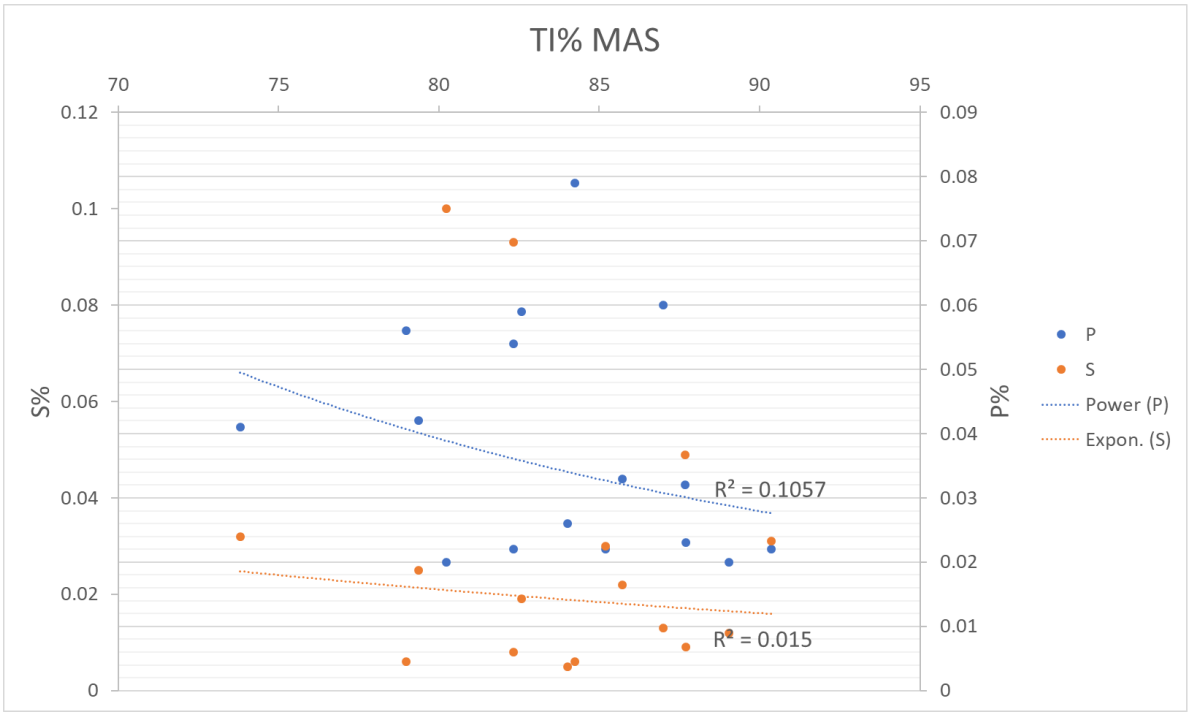
TI% MAS
70
75
80
85
90
95
0.12
0.1
0.08
0.06
0.04
0.02
0
S%
0.09
0.08
0.07
0.06
0.05
0.04
0.03
0.02
0.01
0
P%
R² = 0.1057
R² = 0.015
P
S
Power (P)
Expon. (S)

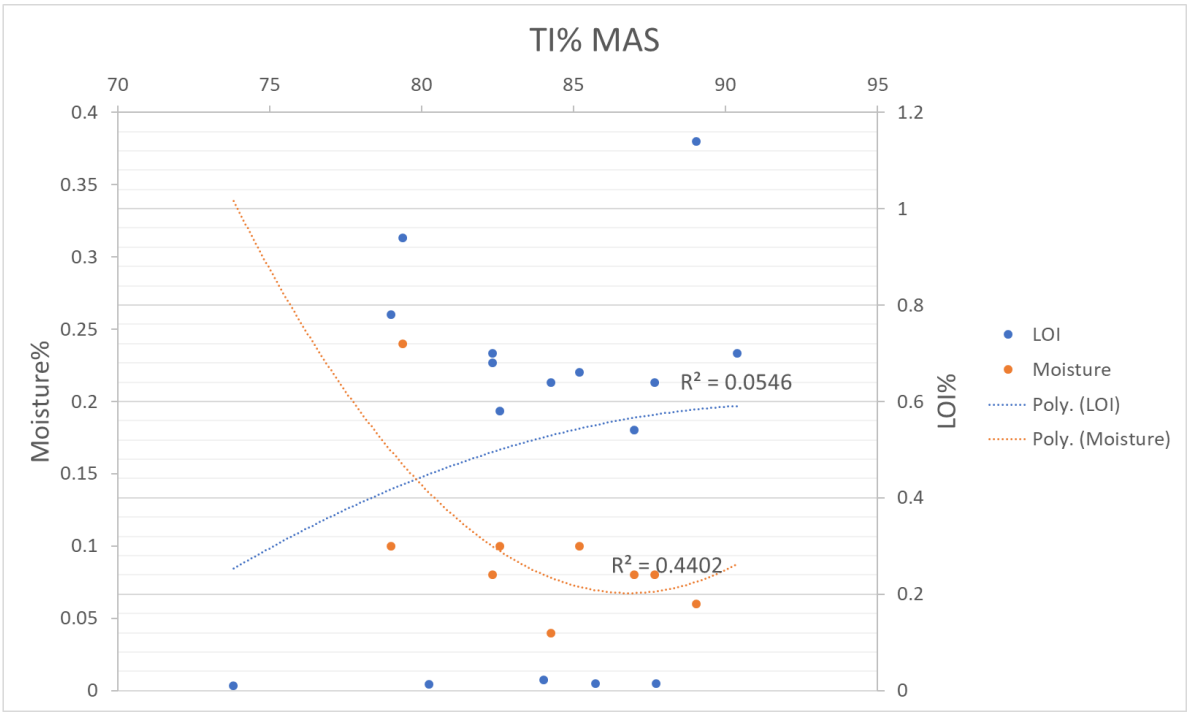
TI% MAS
70
75
80
85
90
95
0.4
0.35
0.3
0.25
0.2
0.15
0.1
0.05
0
Moisture%
1.2
1
0.8
0.6
0.4
0.2
0
LOI%
R² = 0.0546
R² = 0.4402
LOI
Moisture
Poly. (LOI)
Poly. (Moisture)

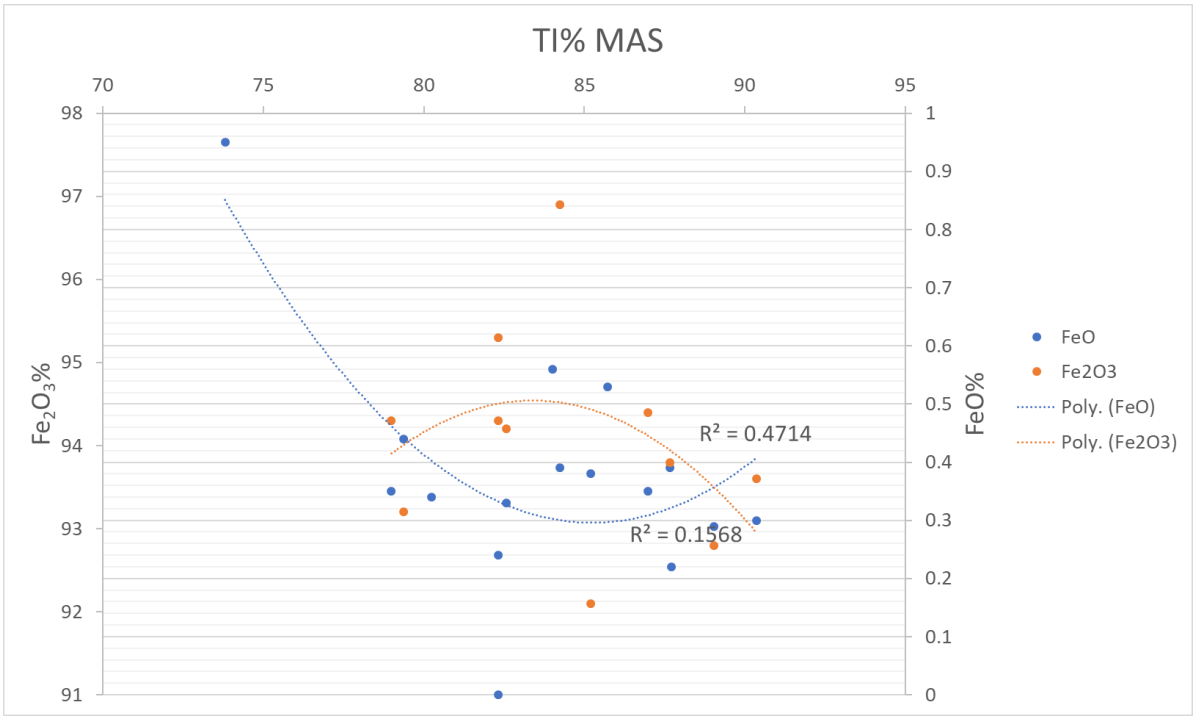
TI% MAS
70
75
80
85
90
95
98
97
96
95
94
93
92
91
1
0.9
0.8
0.7
0.6
0.5
0.4
0.3
0.2
0.1
0
Fe2O3%
FeO%
R² = 0.4714
R² = 0.1568
FeO
Fe2O3
Poly. (FeO)
Poly. (Fe2O3)

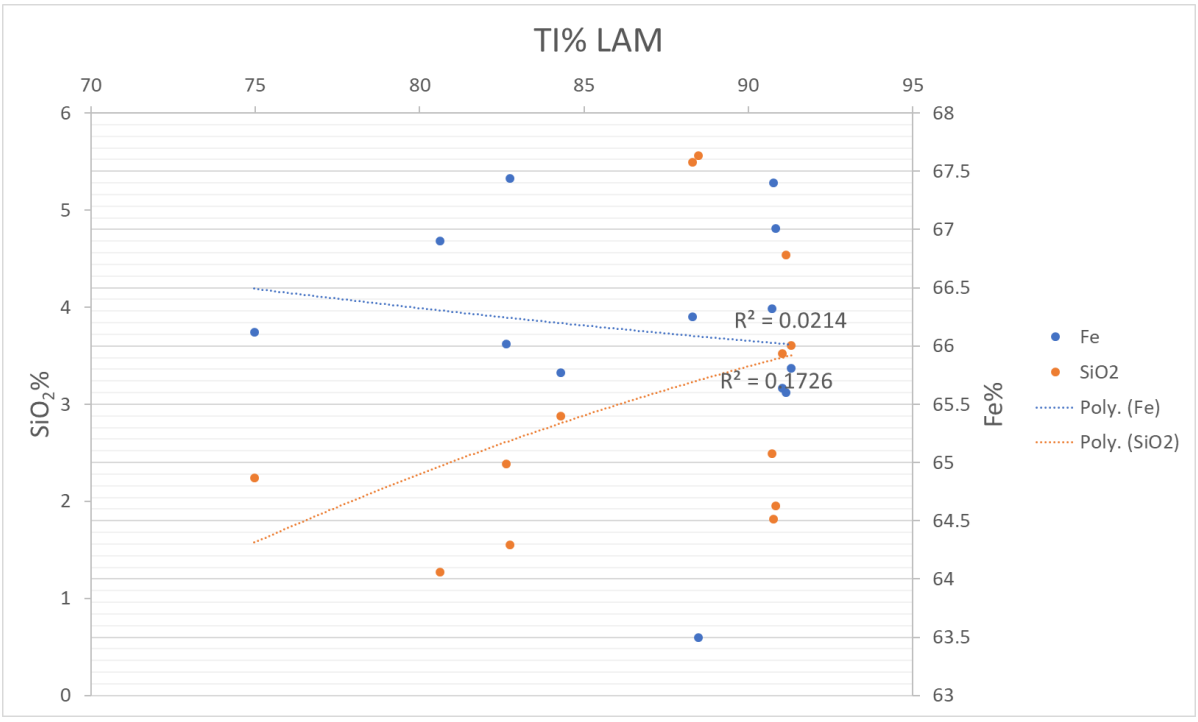
TI% LAM
70
75
80
85
90
95
6
5
4
3
2
1
0
68
67.5
67
66.5
66
65.5
65
64.5
64
63.5
63
SiO2%
Fe%
R² = 0.0214
R² = 0.1726
Fe
SiO2
Poly. (Fe)
Poly. (SiO2)

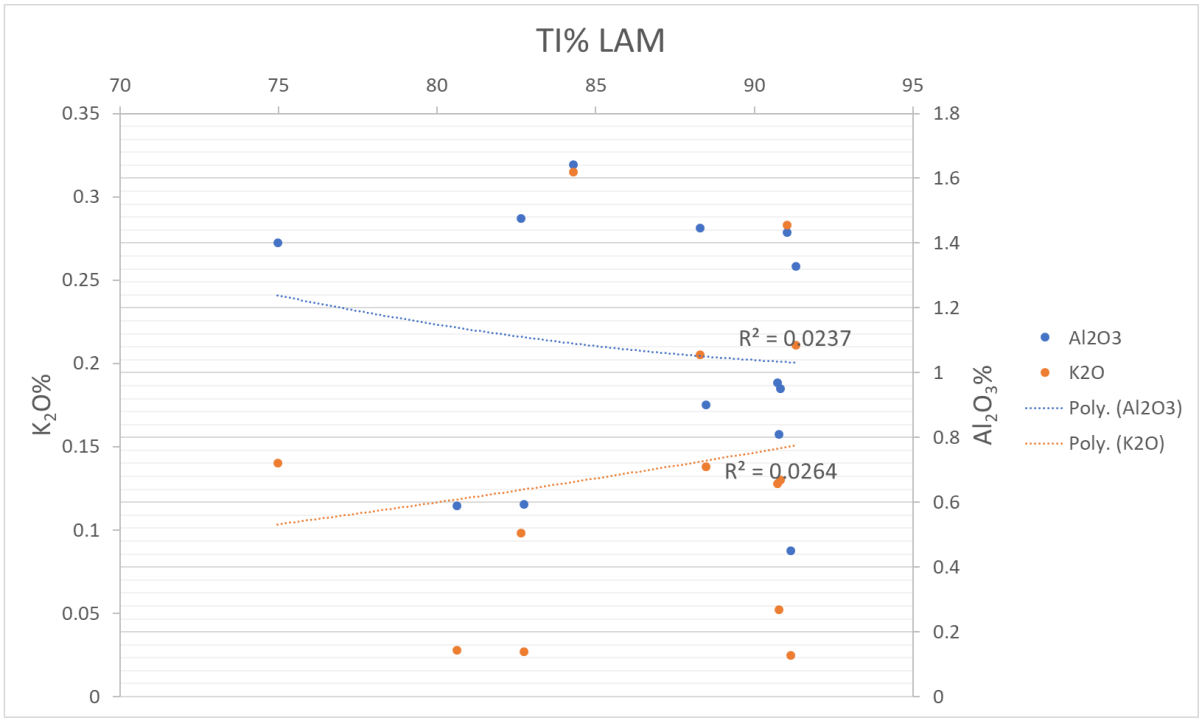
TI% LAM
70
75
80
85
90
95
0.35
0.3
0.25
0.2
0.15
0.1
0.05
0
1.8
1.6
1.4
1.2
1
0.8
0.6
0.4
0.2
0
K2O%
Al2O3%
R² = 0.0237
R² = 0.0264
Al2O3
K2O
Poly. (Al2O3)
Poly. (K2O)

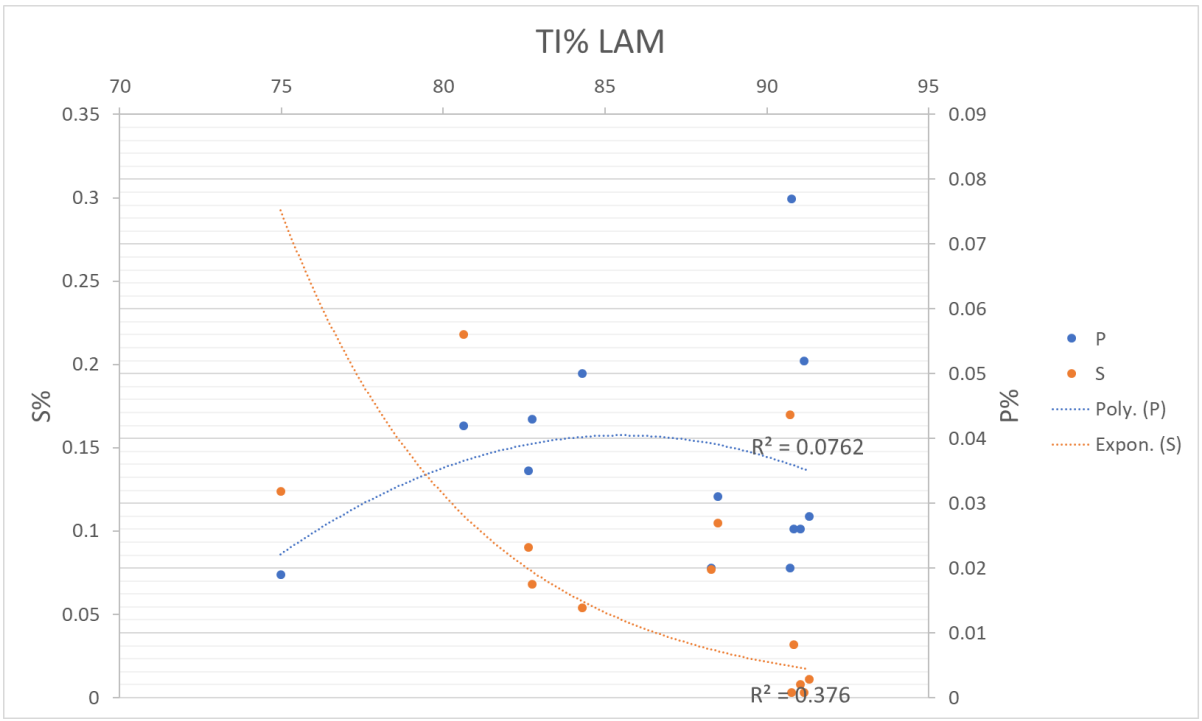
TI% LAM
70
75
80
85
90
95
0.35
0.3
0.25
0.2
0.15
0.1
0.05
0
0.09
0.08
0.07
0.06
0.05
0.04
0.03
0.02
0.01
0
S%
P%
R² = 0.0762
R² = 0.376
P
S
Poly. (P)
Expon. (S)

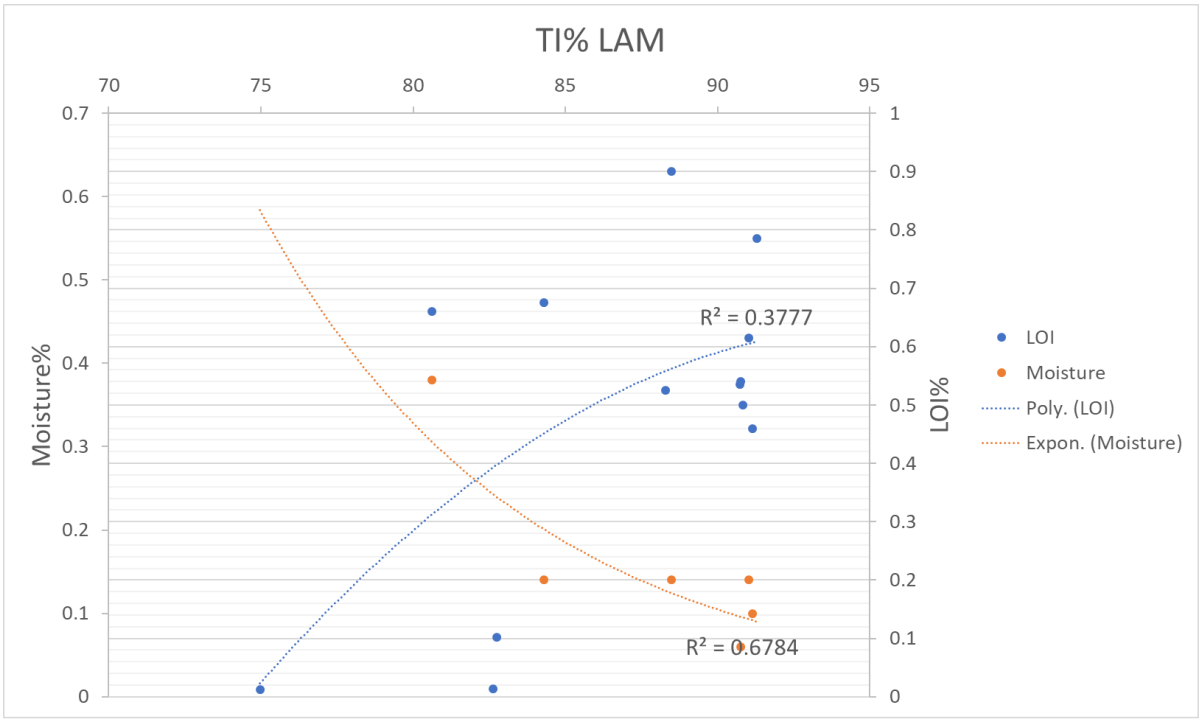
TI% LAM
70
75
80
85
90
95
0.7
0.6
0.5
0.4
0.3
0.2
0.1
0
1
0.9
0.8
0.7
0.6
0.5
0.4
0.3
0.2
0.1
0
Moisture%
LOI%
R² = 0.3777
R² = 0.6784
LOI
Moisture
Poly. (LOI)
Expon. (Moisture)

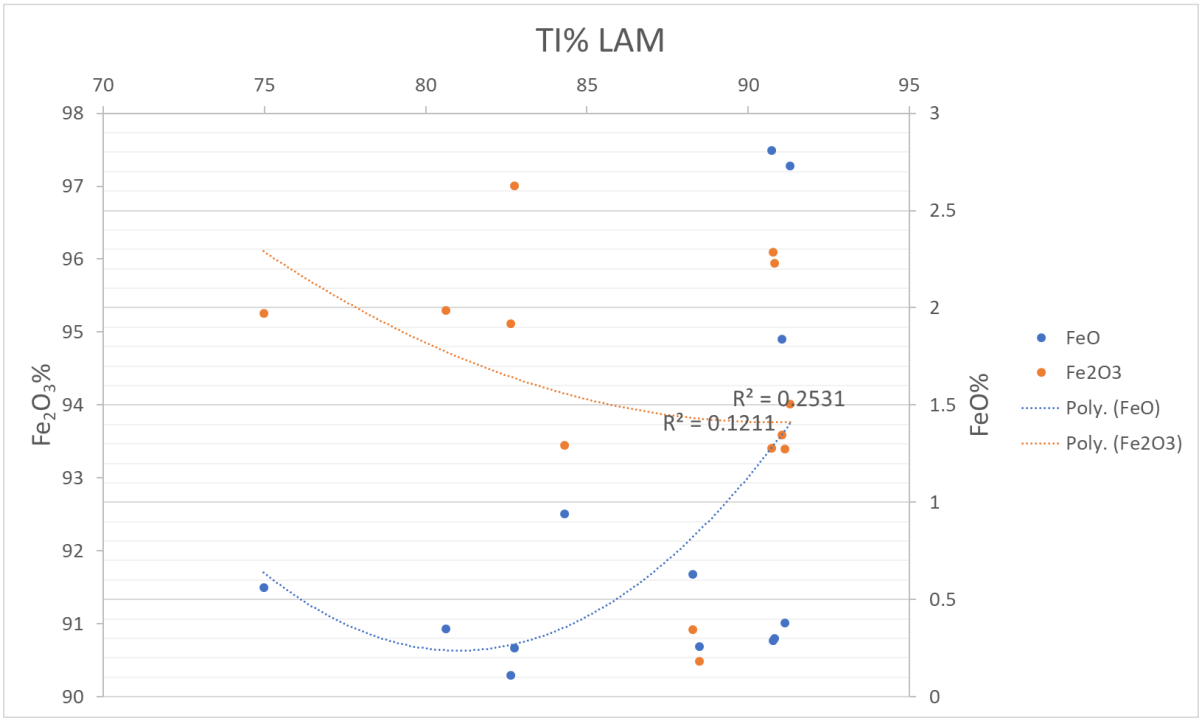
TI% LAM
70
75
80
85
90
95
98
97
96
95
94
93
92
91
90
3
2.5
2
1.5
1
0.5
0
Fe2O3%
FeO%
R² = 0.2531
R² = 0.1211
FeO
Fe2O3
Poly. (FeO)
Poly. (Fe2O3)

Reducibility Index

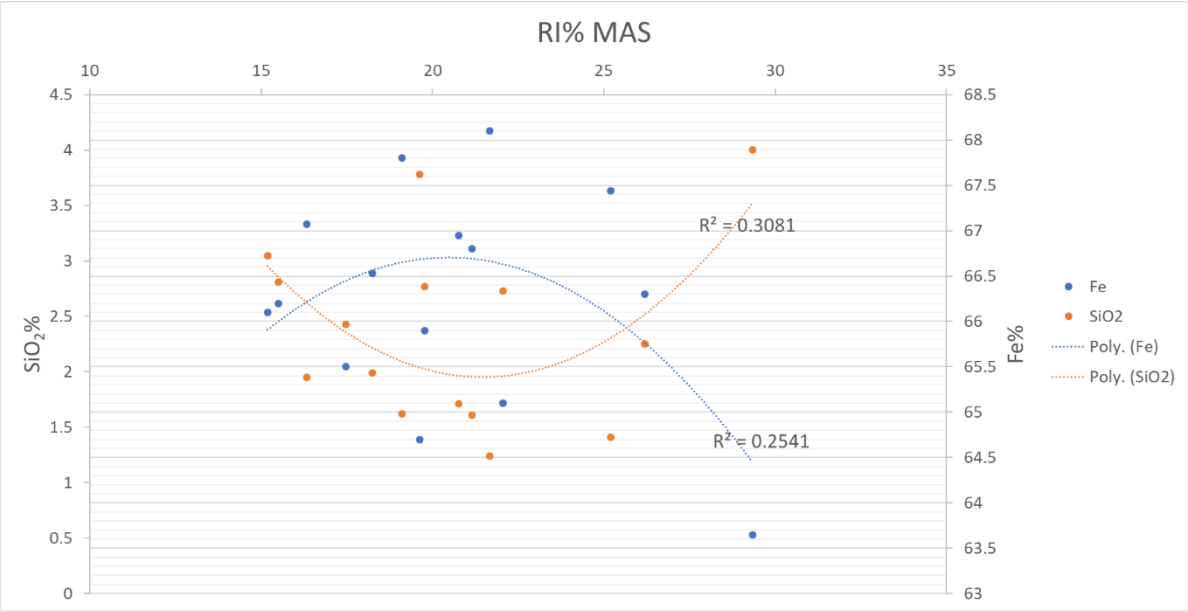

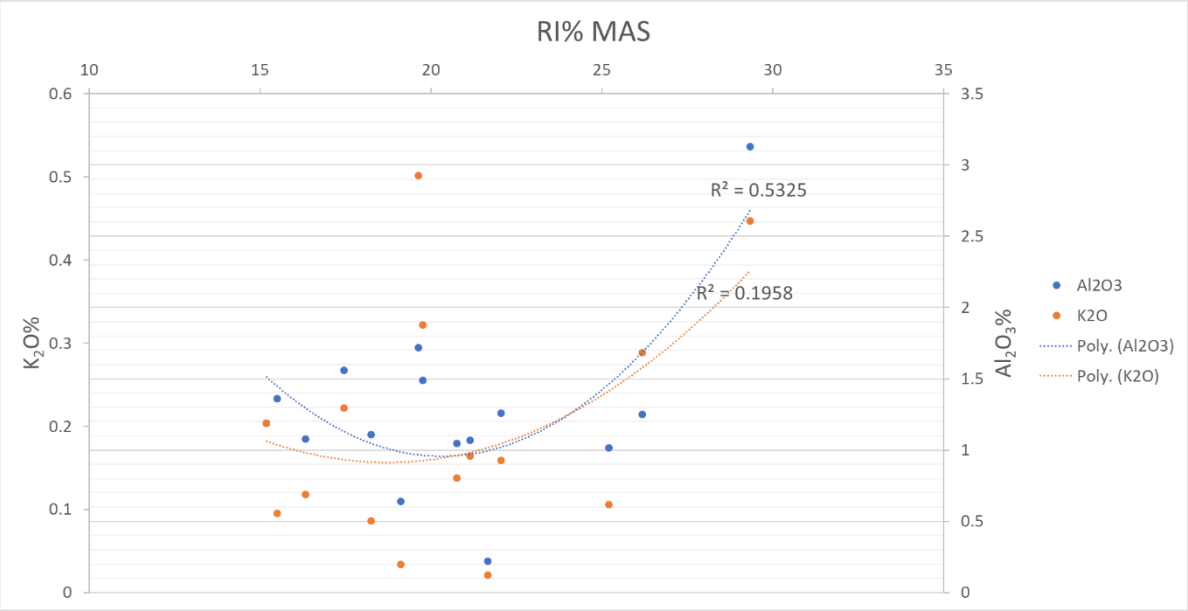

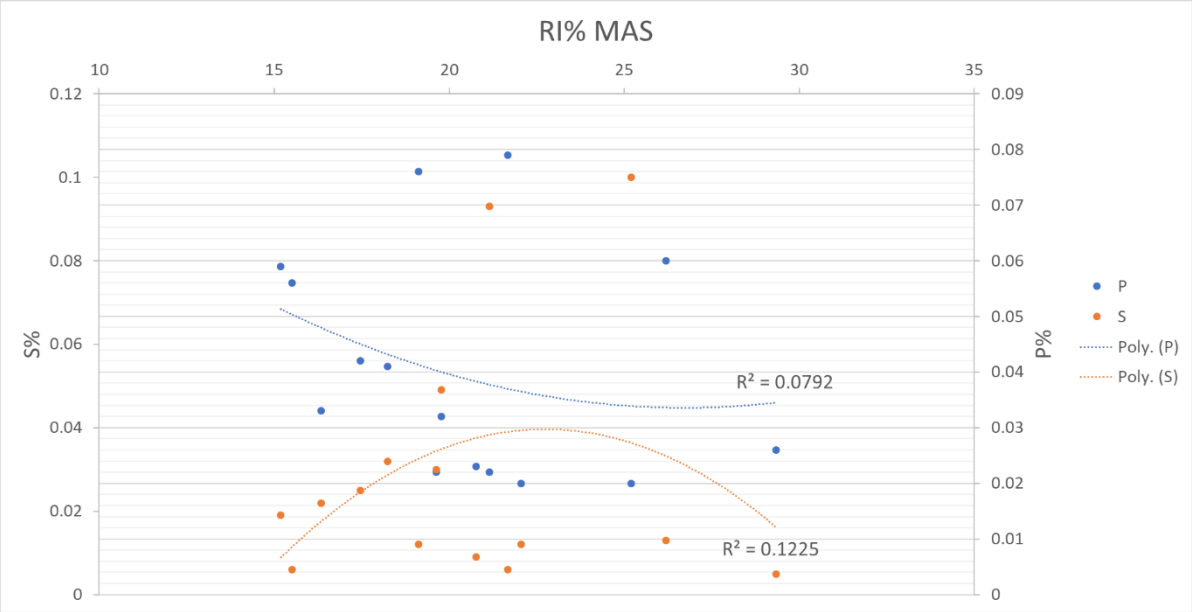
RI% MAS
10
15
20
25
30
35
0.12
0.1
0.08
0.06
0.04
0.02
0
S%
0.09
0.08
0.07
0.06
0.05
0.04
0.03
0.02
0.01
0
P%
R² = 0.0792
R² = 0.1225
P
S
Poly. (P)
Poly. (S)

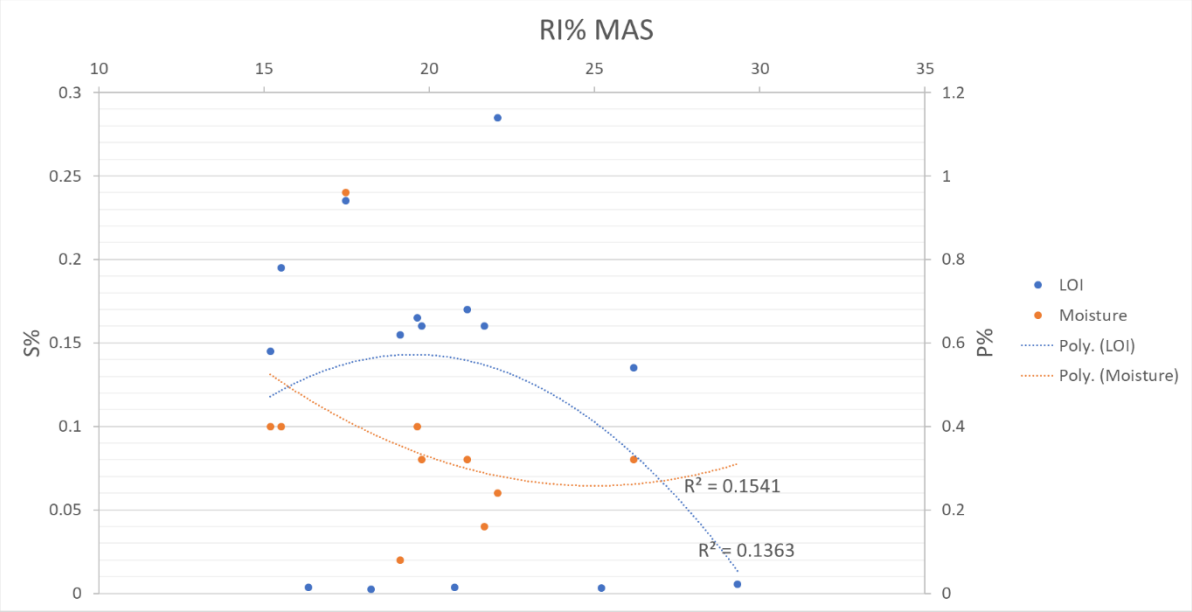
RI% MAS
10
15
20
25
30
35
0.3
0.25
0.2
0.15
0.1
0.05
0
S%
1.2
1
0.8
0.6
0.4
0.2
0
P%
R² = 0.1541
R² = 0.1363
LOI
Moisture
Poly. (LOI)
Poly. (Moisture)

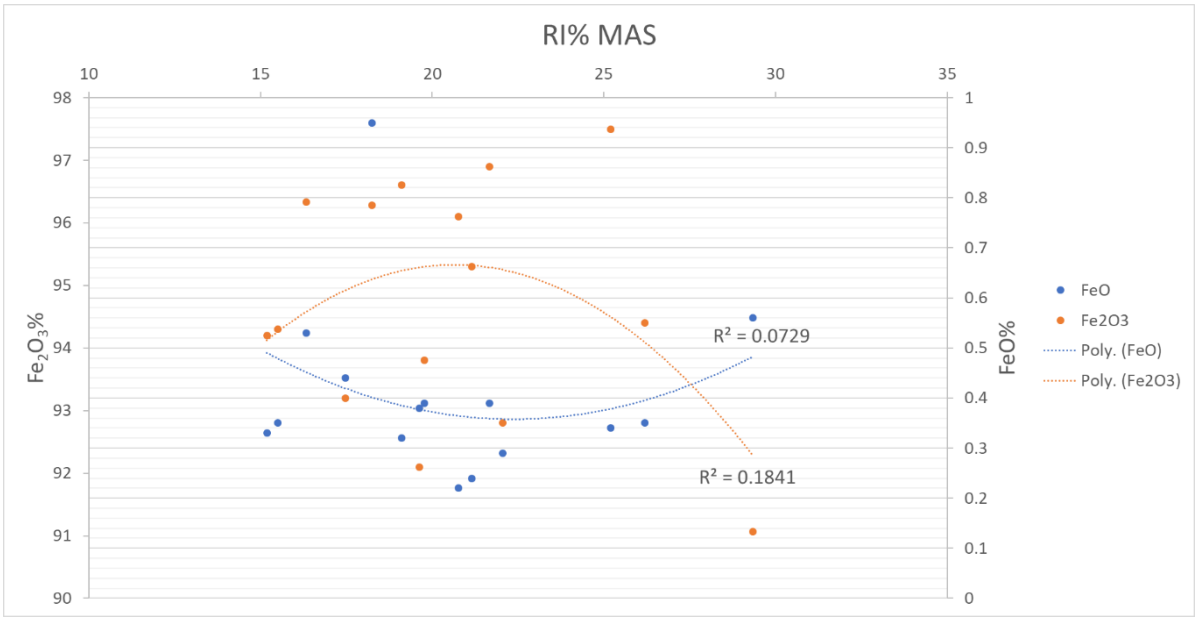
RI% MAS
10
15
20
25
30
35
98
97
96
95
94
93
92
91
90
1
0.9
0.8
0.7
0.6
0.5
0.4
0.3
0.2
0.1
0
Fe2O3%
FeO%
R² = 0.0729
R² = 0.1841
FeO
Fe2O3
Poly. (FeO)
Poly. (Fe2O3)

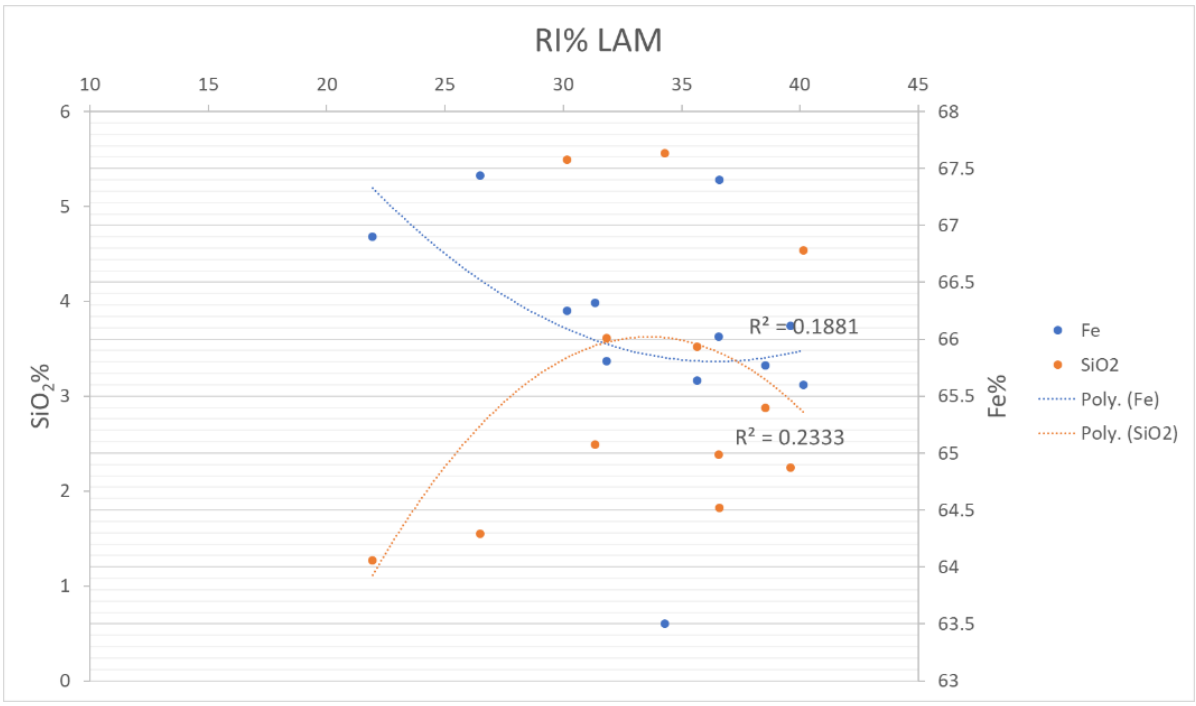
RI% LAM
10
15
20
25
30
35
40
45
6
5
4
3
2
1
0
68
67.5
67
66.5
66
65.5
65
64.5
64
63.5
63
SiO2%
Fe%
R² = 0.1881
R² = 0.2333
Fe
SiO2
Poly. (Fe)
Poly. (SiO2)

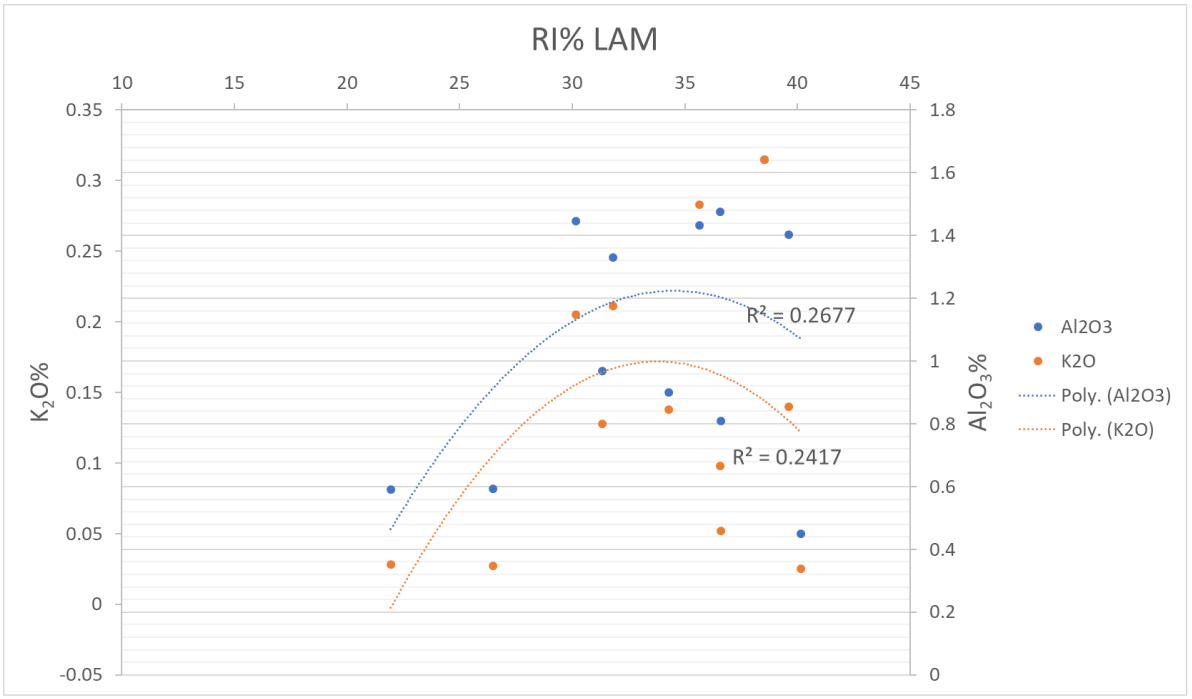
RI% LAM
10 15 20 25 30 35 40 45
0.35 0.3 0.25 0.2 0.15 0.1 0.05 0 -0.05
1.8 1.6 1.4 1.2 1 0.8 0.6 0.4 0.2 0
K2O%
Al2O3%
R² = 0.2677
R² = 0.2417
Al2O3
K2O
Poly. (Al2O3)
Poly. (K2O)

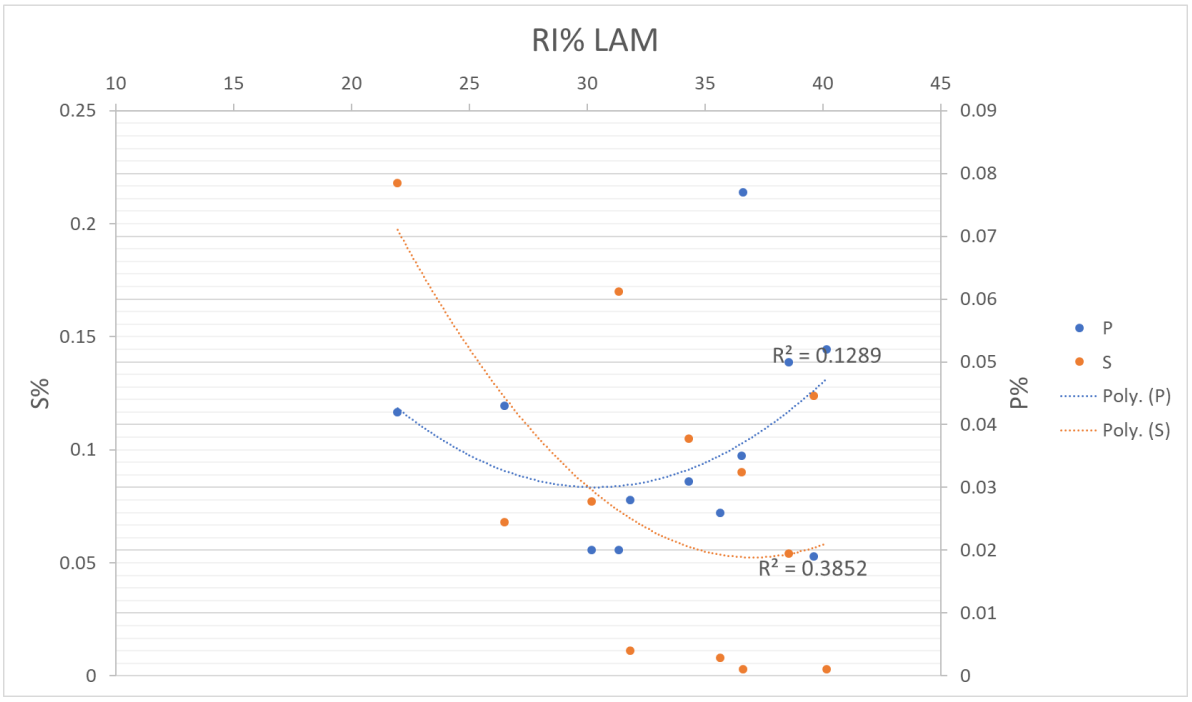
RI% LAM
10 15 20 25 30 35 40 45
0.25 0.2 0.15 0.1 0.05 0
0.09 0.08 0.07 0.06 0.05 0.04 0.03 0.02 0.01 0
S%
P%
R² = 0.1289
R² = 0.3852
P
S
Poly. (P)
Poly. (S)

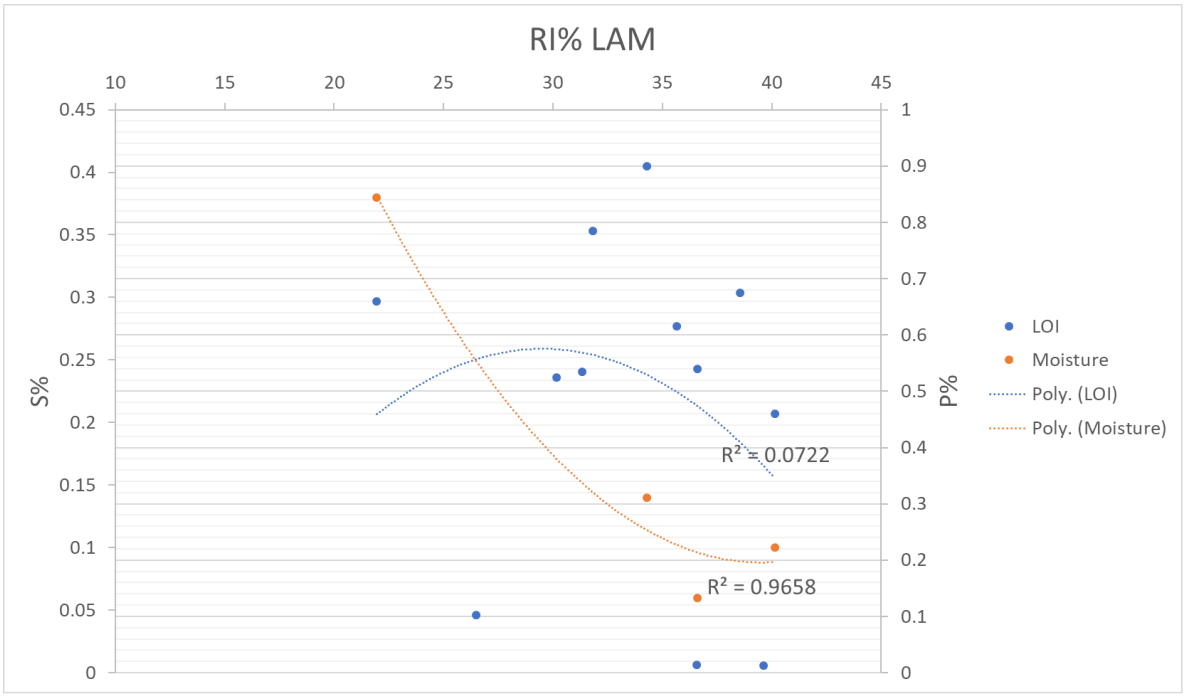
RI% LAM
10
15
20
25
30
35
40
45
0.45
0.4
0.35
0.3
0.25
0.2
0.15
0.1
0.05
0
S%
1
0.9
0.8
0.7
0.6
0.5
0.4
0.3
0.2
0.1
0
P%
R² = 0.0722
R² = 0.9658
LOI
Moisture
Poly. (LOI)
Poly. (Moisture)

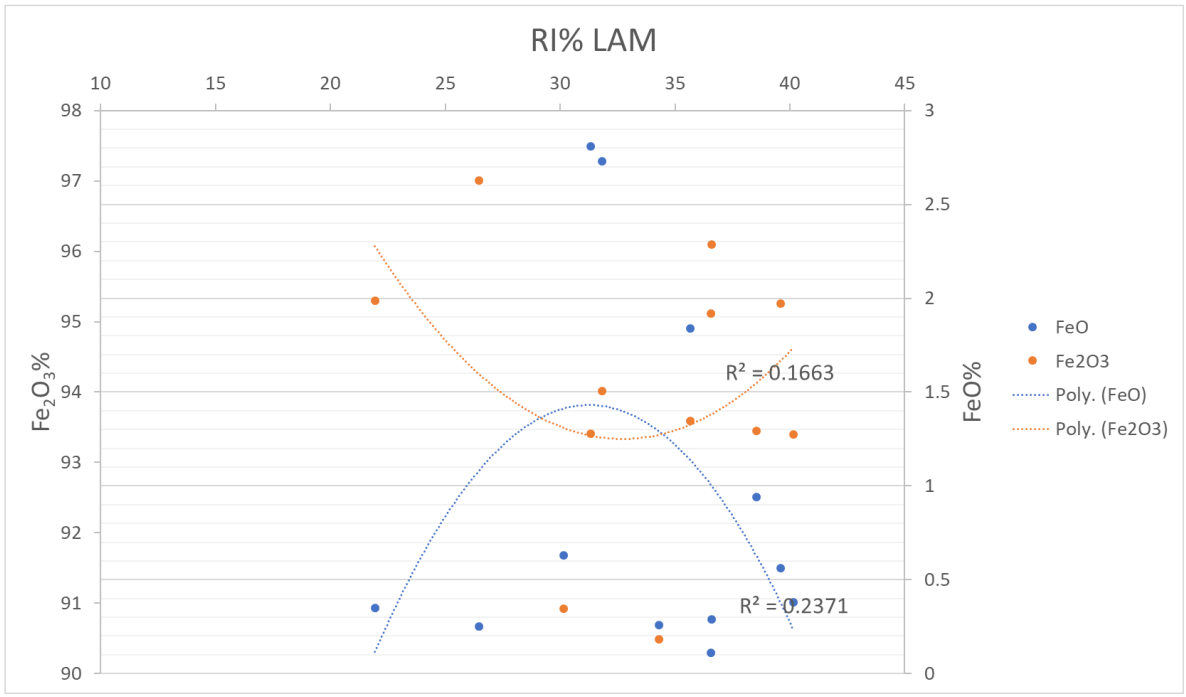
RI% LAM
10
15
20
25
30
35
40
45
98
97
96
95
94
93
92
91
90
Fe2O3%
3
2.5
2
1.5
1
0.5
0
FeO%
R² = 0.1663
R² = 0.2371
FeO
Fe2O3
Poly. (FeO)
Poly. (Fe2O3)

Reduction-Disintegration Index

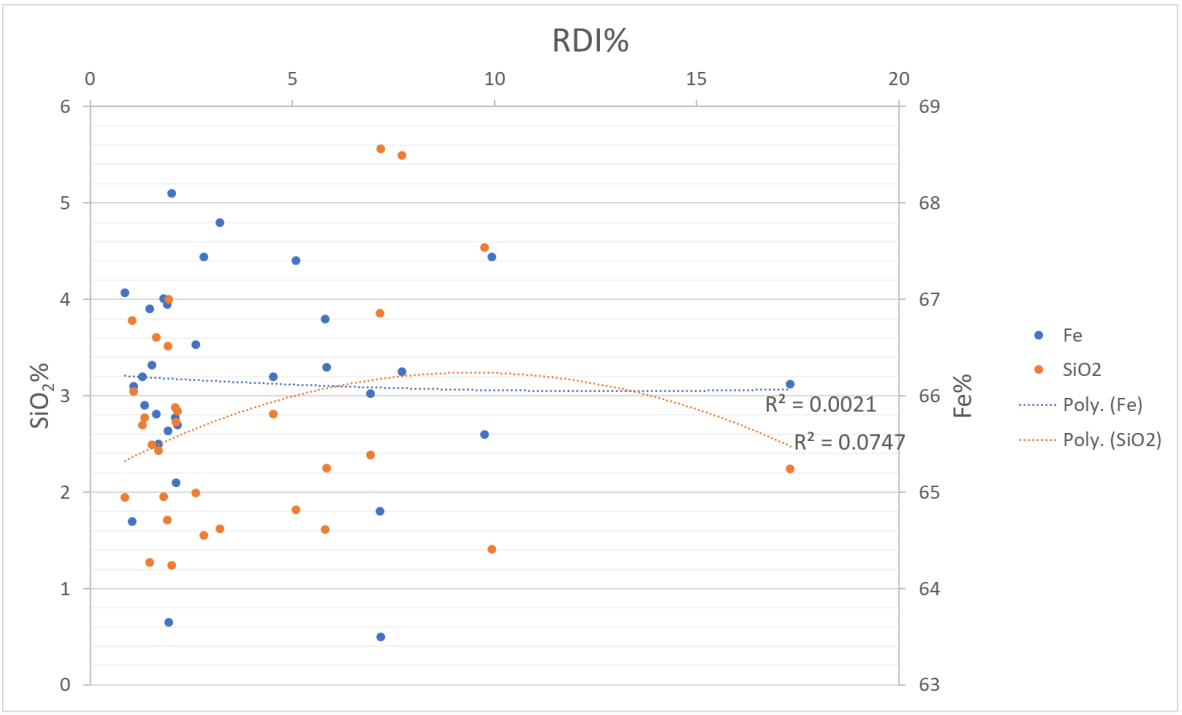

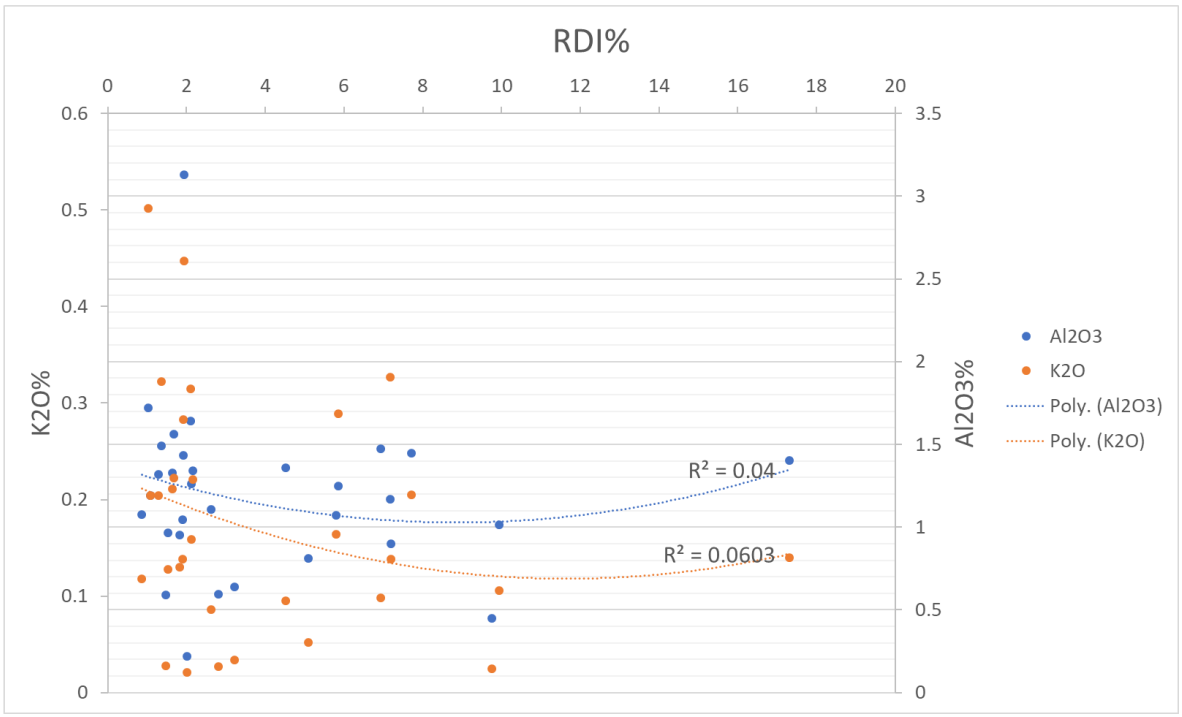

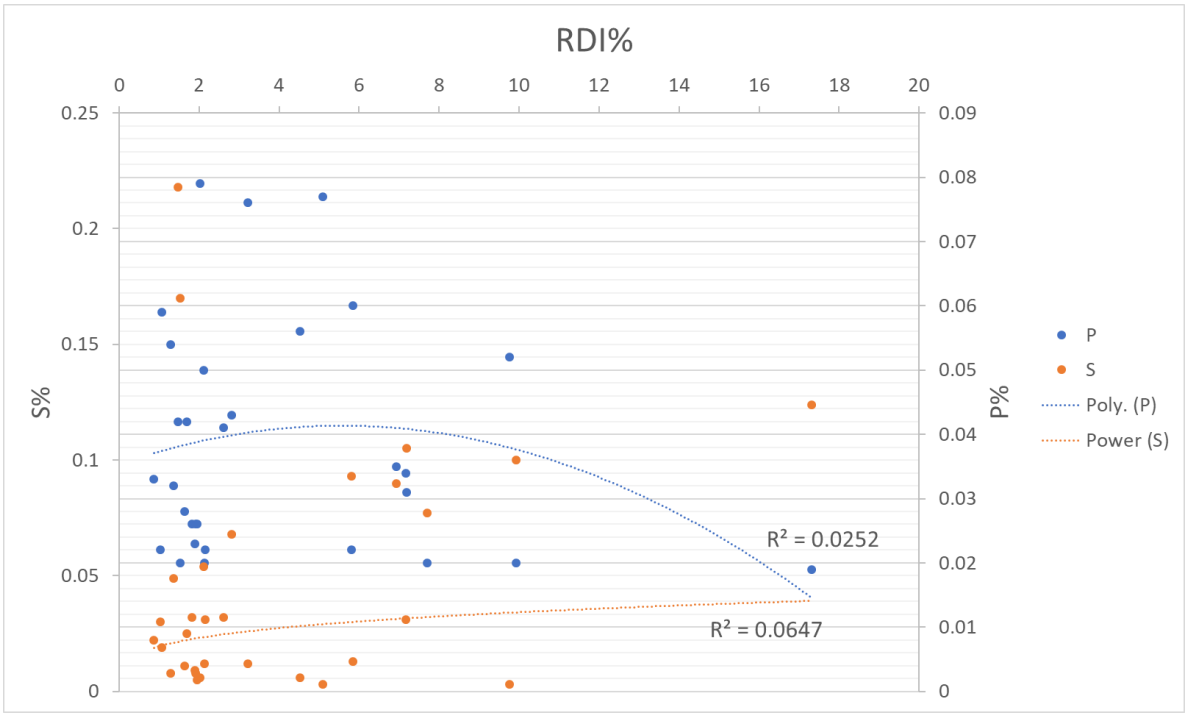
RDI%
0
2
4
6
8
10
12
14
16
18
20
0.25
0.2
0.15
0.1
0.05
0
S%
0.09
0.08
0.07
0.06
0.05
0.04
0.03
0.02
0.01
0
P%
R² = 0.0252
R² = 0.0647
P
S
Poly. (P)
Power (S)

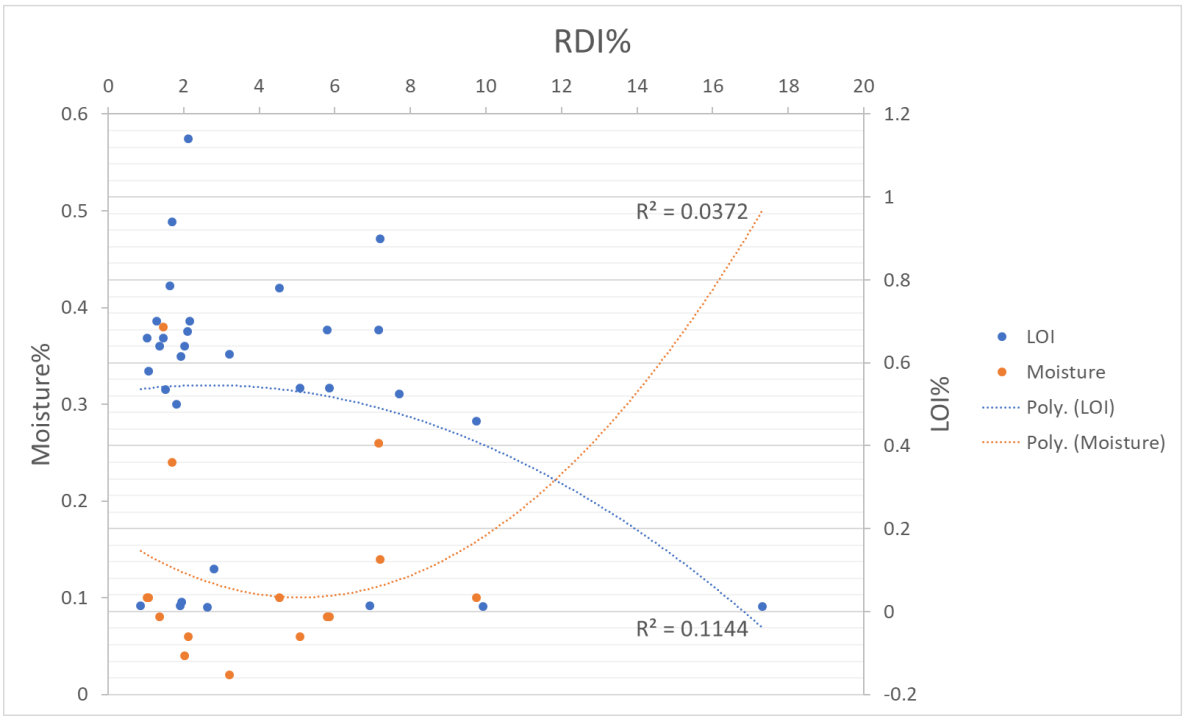
RDI%
0
2
4
6
8
10
12
14
16
18
20
0.6
0.5
0.4
0.3
0.2
0.1
0
Moisture%
1.2
1
0.8
0.6
0.4
0.2
0
-0.2
LOI%
R² = 0.0372
R² = 0.1144
LOI
Moisture
Poly. (LOI)
Poly. (Moisture)

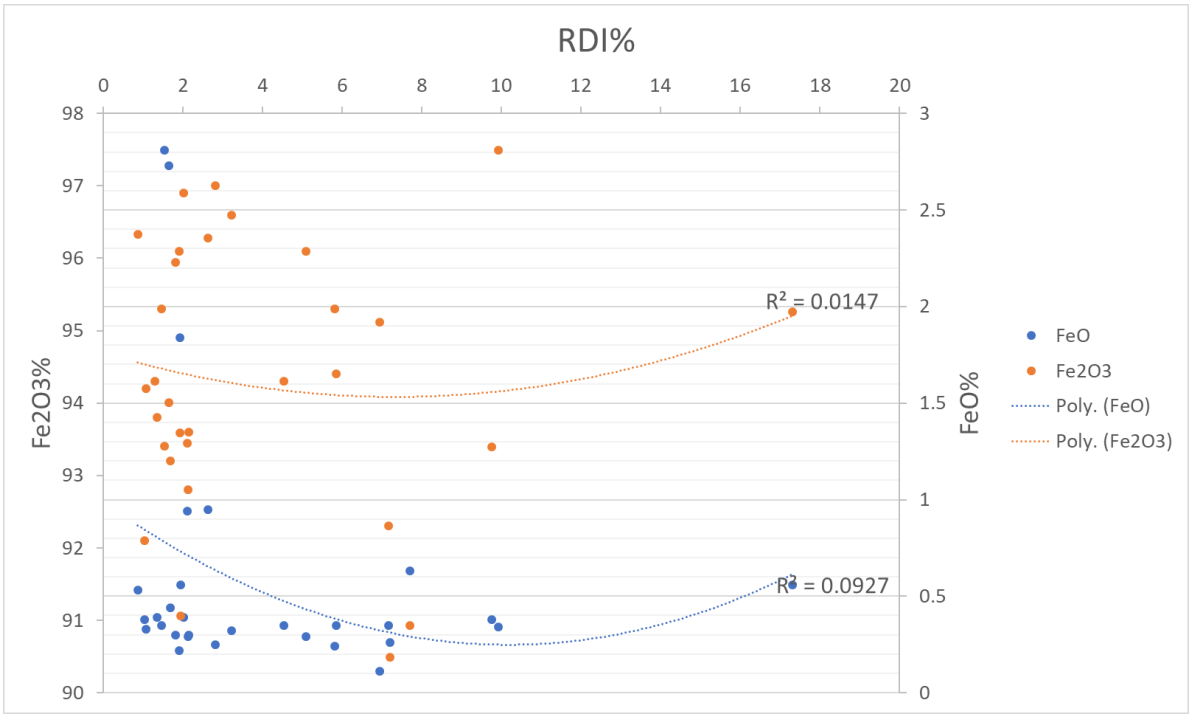
RDI%
0
2
4
6
8
10
12
14
16
18
20
98
97
96
95
94
93
92
91
90
Fe2O3%
3
2.5
2
1.5
1
0.5
0
FeO%
R² = 0.0147
R² = 0.0927
FeO
Fe2O3
Poly. (FeO)
Poly. (Fe2O3)

Decrepitation Index

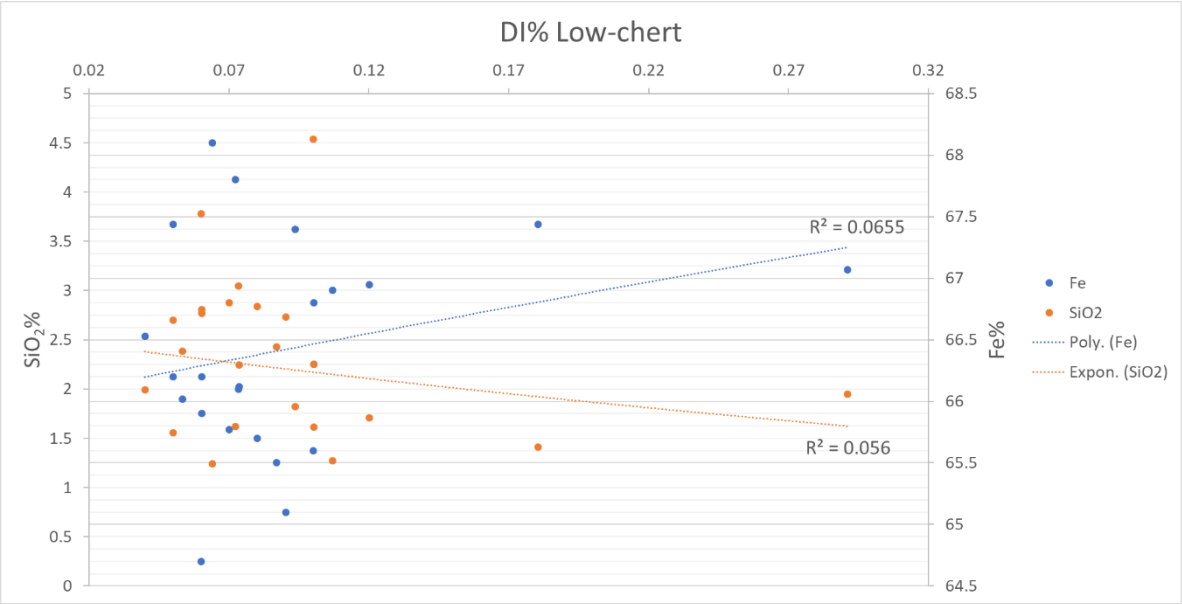

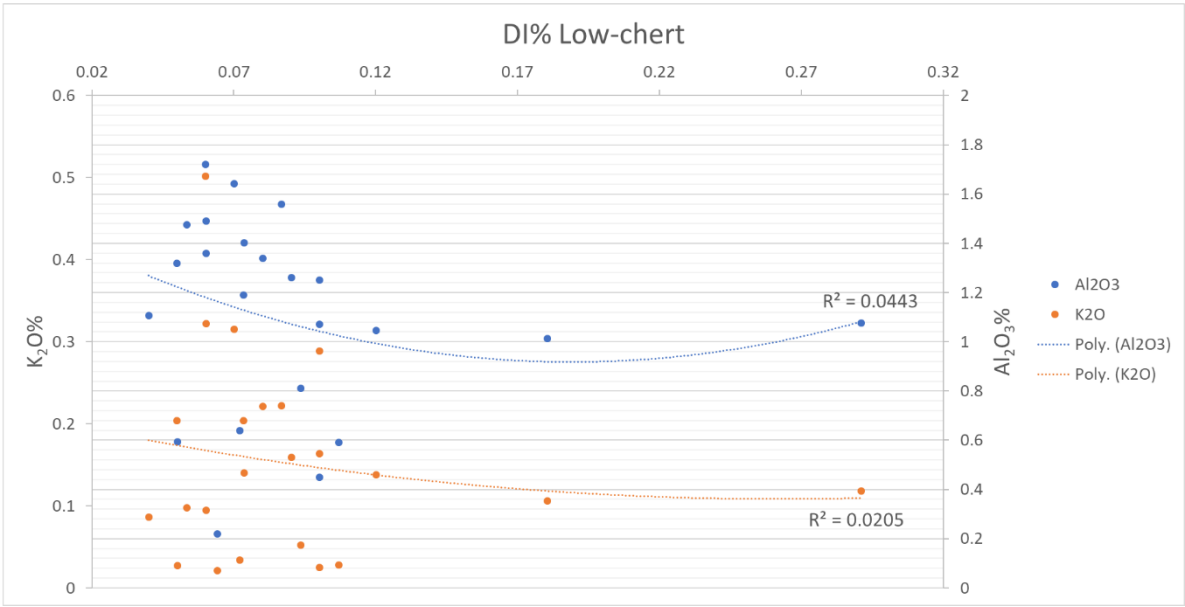

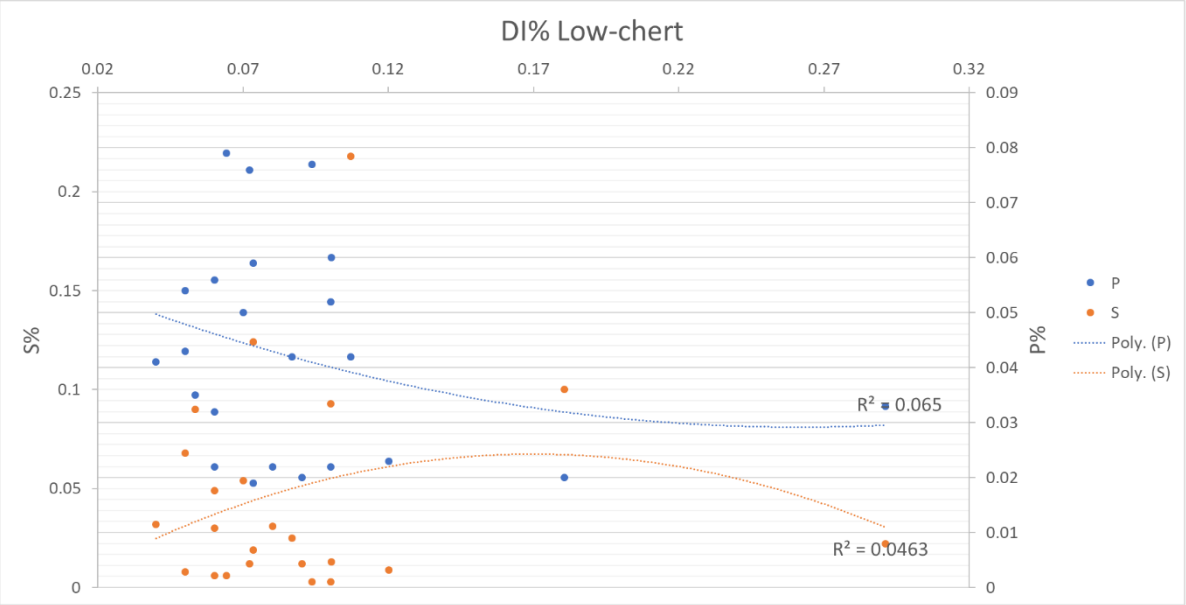
DI% Low-chert
0.02
0.07
0.12
0.17
0.22
0.27
0.32
0.25
0.2
0.15
0.1
0.05
0
S%
0.09
0.08
0.07
0.06
0.05
0.04
0.03
0.02
0.01
0
P%
R² = 0.065
R² = 0.0463
P
S
Poly. (P)
Poly. (S)

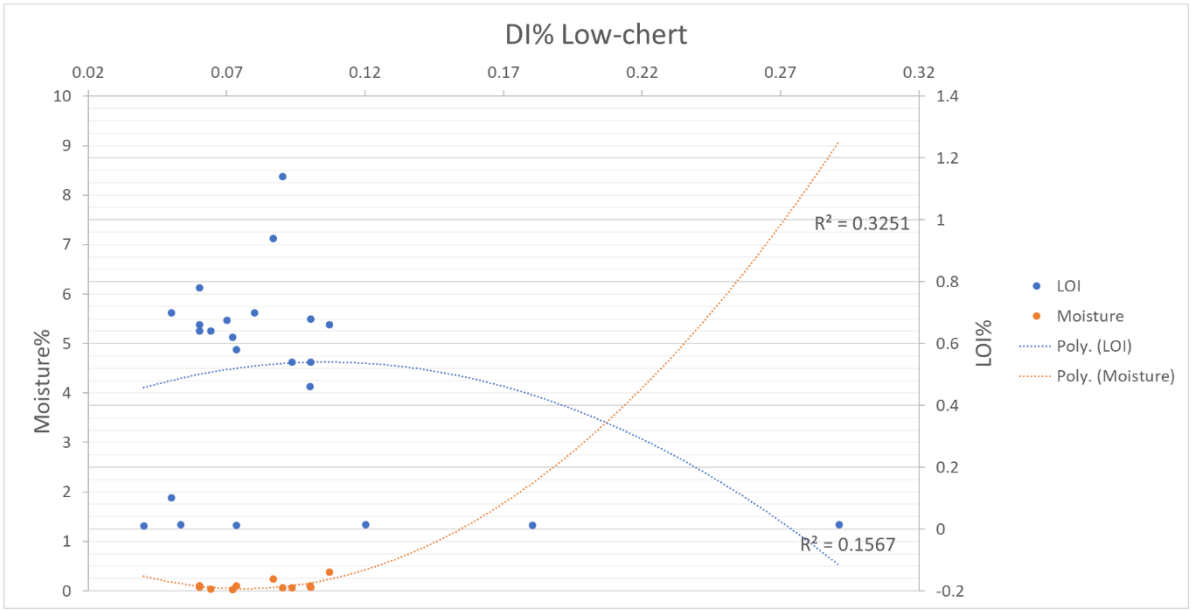
DI% Low-chert
0.02
0.07
0.12
0.17
0.22
0.27
0.32
10
9
8
7
6
5
4
3
2
1
0
Moisture%
1.4
1.2
1
0.8
0.6
0.4
0.2
0
-0.2
LOI%
R² = 0.3251
R² = 0.1567
LOI
Moisture
Poly. (LOI)
Poly. (Moisture)

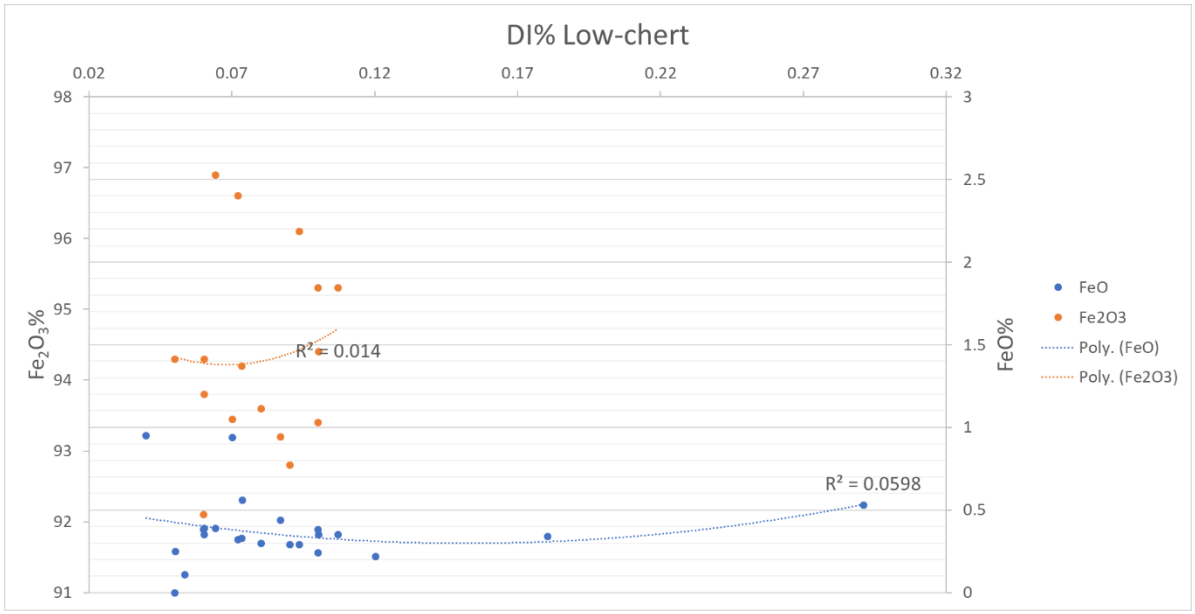
DI% Low-chert
0.02
0.07
0.12
0.17
0.22
0.27
0.32
98
97
96
95
94
93
92
91
3
2.5
2
1.5
1
0.5
0
Fe2O3%
FeO%
R² = 0.014
R² = 0.0598
FeO
Fe2O3
Poly. (FeO)
Poly. (Fe2O3)

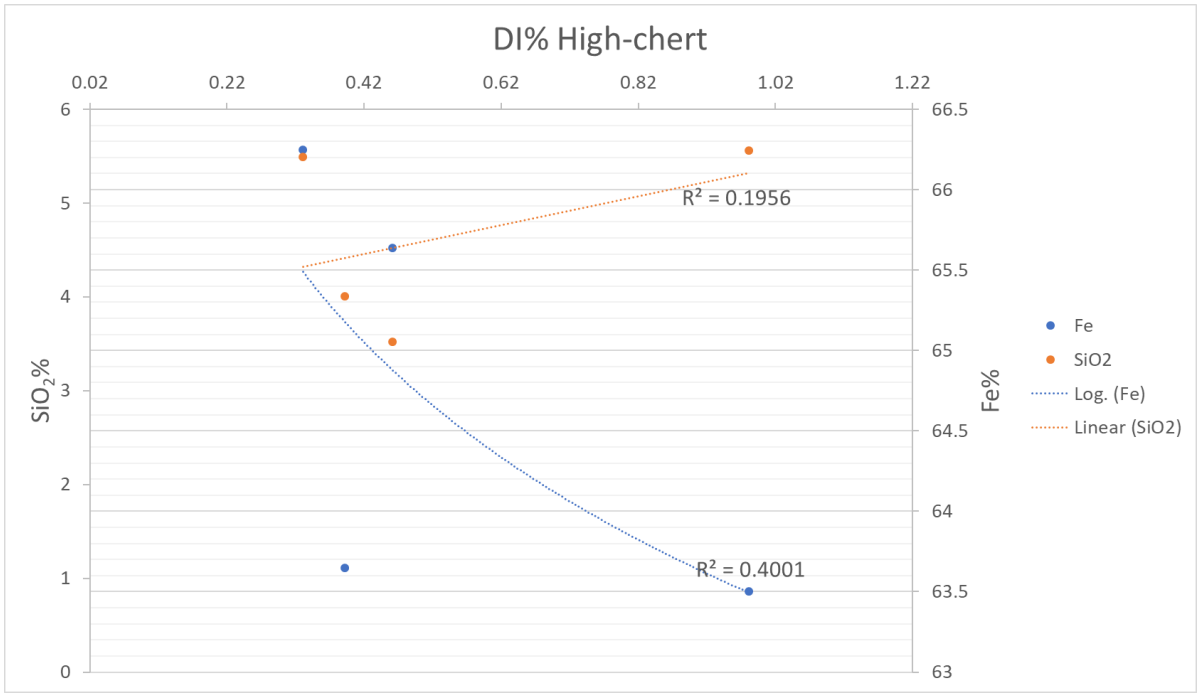
DI% High-chert
0.02
0.22
0.42
0.62
0.82
1.02
1.22
6
5
4
3
2
1
0
66.5
66
65.5
65
64.5
64
63.5
63
SiO2%
Fe%
R² = 0.1956
R² = 0.4001
Fe
SiO2
Log. (Fe)
Linear (SiO2)

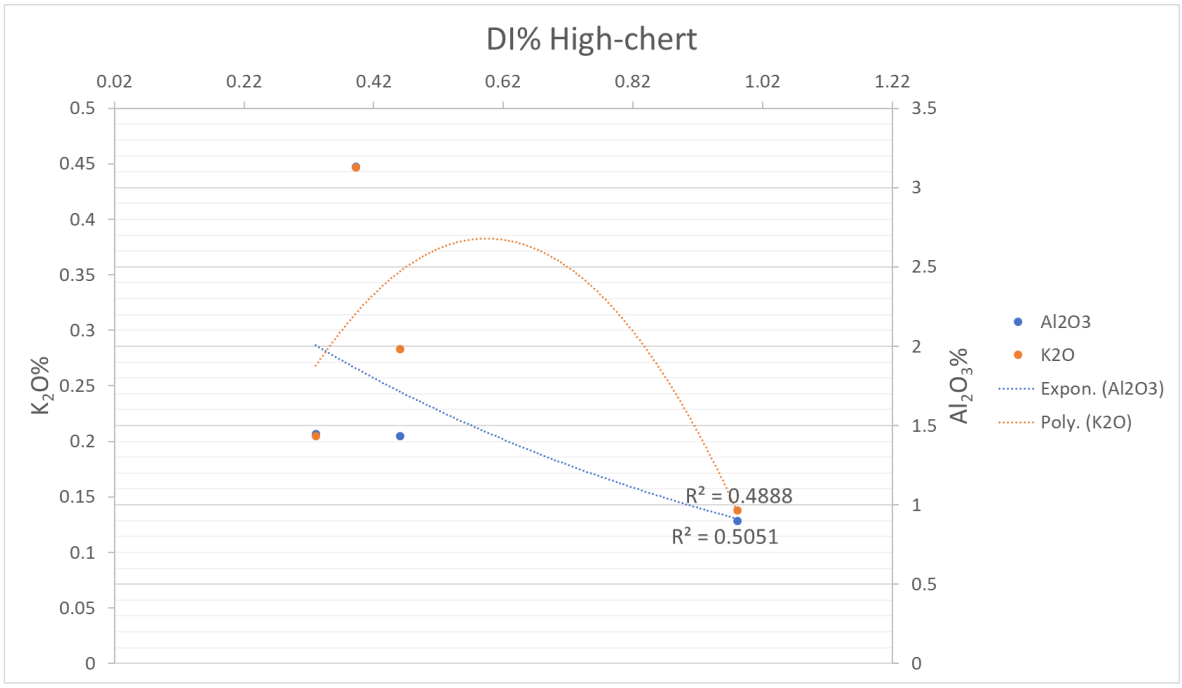
DI% High-chert
0.02
0.22
0.42
0.62
0.82
1.02
1.22
0.5
0.45
0.4
0.35
0.3
0.25
0.2
0.15
0.1
0.05
0
3.5
3
2.5
2
1.5
1
0.5
0
K2O%
Al2O3%
R² = 0.4888
R² = 0.5051
Al2O3
K2O
Expon. (Al2O3)
Poly. (K2O)

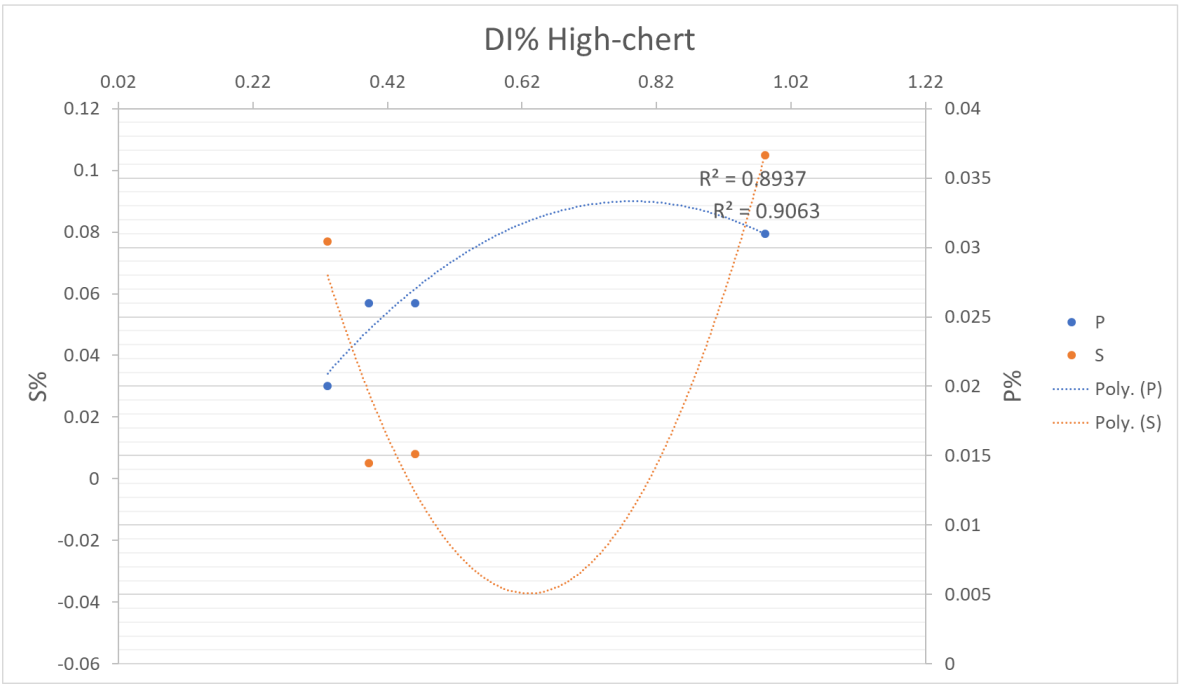
DI% High-chert
0.02
0.22
0.42
0.62
0.82
1.02
1.22
0.12
0.1
0.08
0.06
0.04
0.02
0
-0.02
-0.04
-0.06
0.04
0.035
0.03
0.025
0.02
0.015
0.01
0.005
0
S%
P%
R² = 0.8937
R² = 0.9063
P
S
Poly. (P)
Poly. (S)

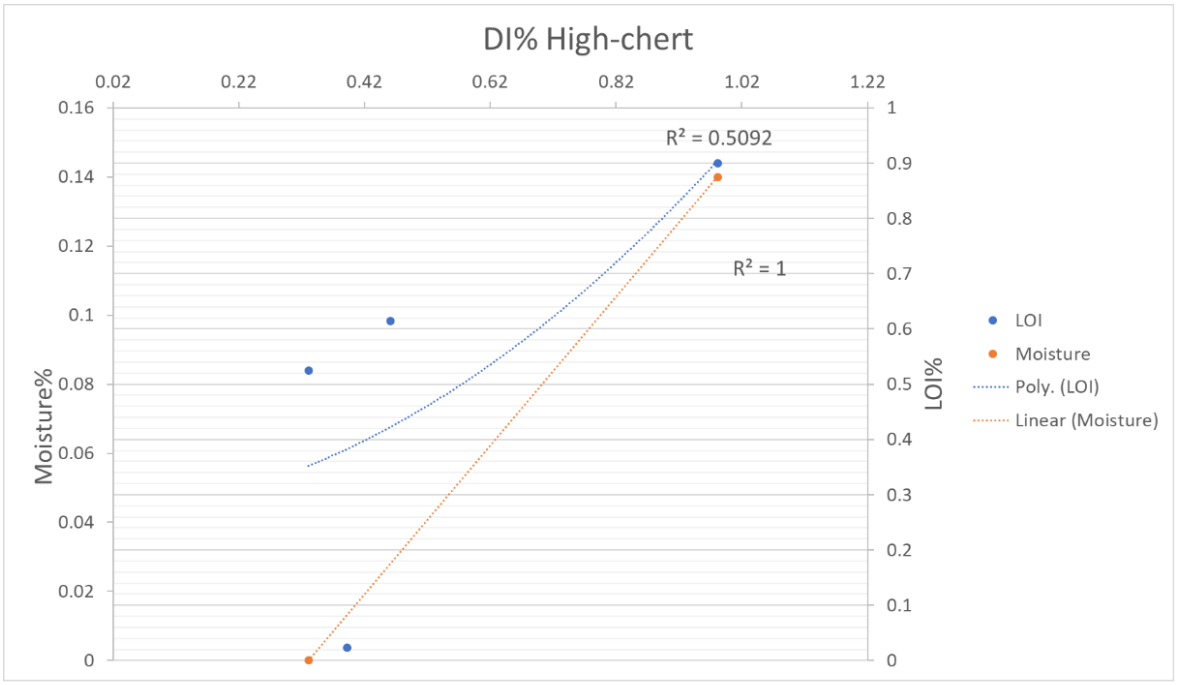
DI% High-chert
0.02
0.22
0.42
0.62
0.82
1.02
1.22
0.16
0.14
0.12
0.1
0.08
0.06
0.04
0.02
0
1
0.9
0.8
0.7
0.6
0.5
0.4
0.3
0.2
0.1
0
R² = 0.5092
R² = 1
Moisture%
LOI%
LOI
Moisture
Poly. (LOI)
Linear (Moisture)

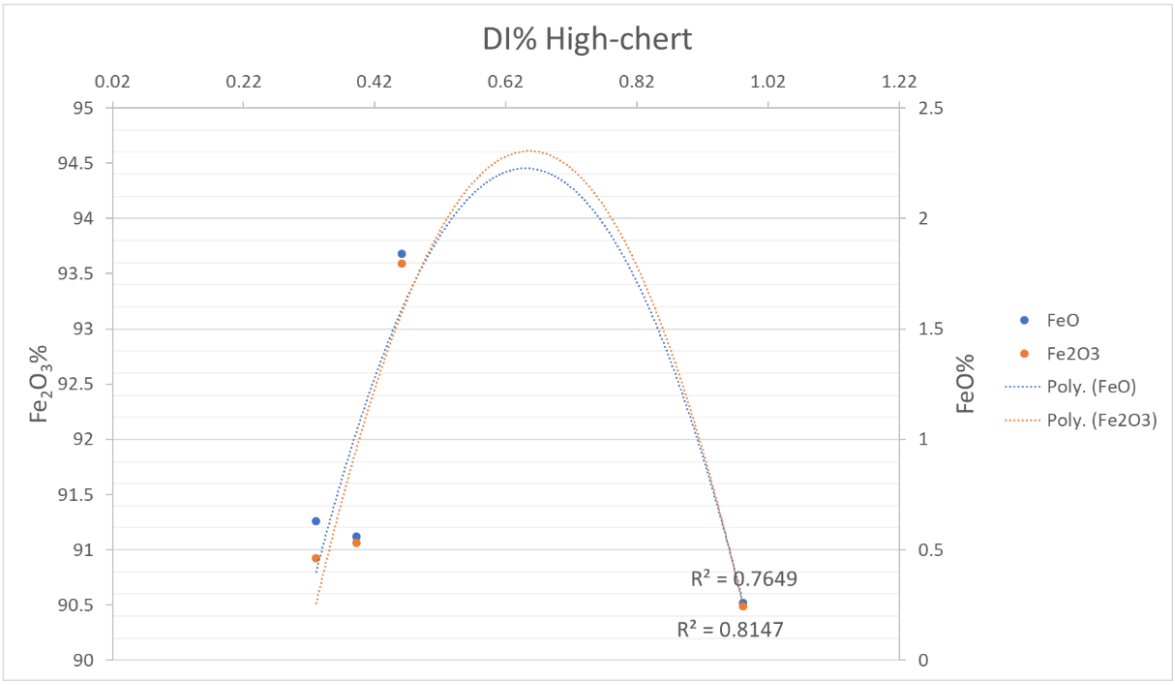
DI% High-chert
0.02
0.22
0.42
0.62
0.82
1.02
1.22
95
94.5
94
93.5
93
92.5
92
91.5
91
90.5
90
2.5
2
1.5
1
0.5
0
R² = 0.7649
R² = 0.8147
Fe2O3%
FeO%
FeO
Fe2O3
Poly. (FeO)
Poly. (Fe2O3)